# Safety and Safeguards for Molten Salt Reactors in Integrated Energy Systems

A Dissertation Presented for the

Doctor of Philosophy

Degree

The University of Tennessee, Knoxville

Nicholas J. Dunkle

May 2025

# Acknowledgements

I wish to thank Dr. Sandra Bogetic and Dr. Nicholas Brown for their reliable advice and assistance in my efforts towards my PhD. I also wish to thank Dr. Ondrej Chvala for his help in starting my graduate school journey. Lastly, I wish to thank Lance Drouet for fixing my laptop when the keyboard stopped functioning.

This work was funded under U. S. Department of Energy Nuclear Energy University Programs federal grant DE-NE0009214.

# Abstract

The research conducted in this work investigates the dynamic behavior of a fast spectrum molten salt reactor (MSR) when used in an integrated energy system (IES) with both a regenerative Rankine heat cycle balance of plant for electricity production and a hydrogen production plant using the hybrid sulfur thermochemical cycle. The research was accomplished by constructing dynamic models of the systems in OpenModelica, debugging, and making a combined IES model. From there, a suite of simulations were performed on the models meant to determine the systems' response to three types of accidents: reactivity initiated accidents (RIA), loss of flow accidents (LOFA), and loss of heat sink accidents (LOHSA). Also included in this research is analysis of multiple types of safeguards techniques for MSRs with a specific focus on a novel technique whereby passive monitoring of the MSR's offgas provides unique plutonium signatures in a timely manner. The other MSR safeguards techniques discussed are frequency analysis, archival monitoring, and accountancy transition. The overarching goal of the research is to make a comprehensive safety and safeguards investigation of the use of an MSR in an IES as a means of promoting awareness of the benefits of the technology and improving its potential deployability.

# Table of Contents

# List of Tables

# List of Figures

# Chapter 1

# Introduction

## 1.1 Motivations and Goals

With nearly a fourth of the century passed, it is widely understood that climate change will be one of, if not the most, major issues facing Humanity. Properly confronting the energy crisis due to climate change requires decarbonization and a shift to other forms of energy production to maintain current consumption levels. However, overall energy demand around the world is only expected to rise along with the global population and the recent apparent boom in artificial intelligence development. Last year, the global population surpassed eight billion, and the UN predicts that the population will reach 9.7 billion in 2050 and peak at approximately 10.4 billion in the mid-2080s. [3] The majority of the current and predicted population growth is within developing countries that currently have energy consumption per capita averages at a fraction of that in developed countries. [4] As such, global energy production must not only shift to cleaner non-carbon emitting sources, but also increase in scale by multiple times over. That realization is the true scope of the energy crisis in modern times. Nuclear energy can be used to meet the energy challenges of our time through the use of innovative utilization techniques and novel energy production methods. These novel energy production methods are advanced reactors which have a variety

of different designs, capabilities, benefits, and potential uses. The type of advanced reactor focused on in this work is Molten Salt Reactors (MSRs), which use molten salts for their primary cooling and heat transfer. Specifically focused on in this work are MSRs with their fuel in a liquid form mixed in a halide melt, known as fuel salt. This fuel salt flows throughout the primary loop of the reactor and is the primary difference when compared to conventional light water reactors (LWRs). The primary benefit of using fuel salt is that the temperature of the reactor can be higher while operating at a lower pressure due to its superior thermal properties compared to solid fuel cooled by water. In simple terms, lower operating pressures and higher temperature tolerances allow for improved safety, while higher nominal temperatures allow for improved efficiency and innovative utilization techniques. These techniques are broadly any use for nuclear power in the energy market beyond electricity generation. Currently, nuclear power is used almost entirely for electricity generation, as seen by using the United States as an example in Figure 1.1.

While further electrification of the economy would likely allow for more utilization of clean energy sources, there are major economic sectors that could not reasonably or effectively switch to only electricity consumption. These sectors are namely industrial and transportation. Considering the inability to fully electrify the economy and the development time necessary to approach the maximum effective electrification capacity, limiting nuclear power to only electricity generation greatly limits its potential to aid in the aforementioned energy crisis. The heat produced by a nuclear reactor could be used to drive a variety of energy intensive industrial processes such as desalination, hydrogen production, nitrogen-based fertilizer production, and metallurgy. The coupling of an electricity producing power plant to a heat intensive process is known as an integrated energy system (IES). [5] One such example which proves the feasibility of nuclear power in an IES is the BN-350 in Aktau, Kazakhstan which was a sodium-cooled fast reactor that operated from 1973 to 1994 and produced both electricity and desalinated fresh water. [6] In some other cases, a non-nuclear power plant has been dually used in an IES for desalination. [7] The industrial process

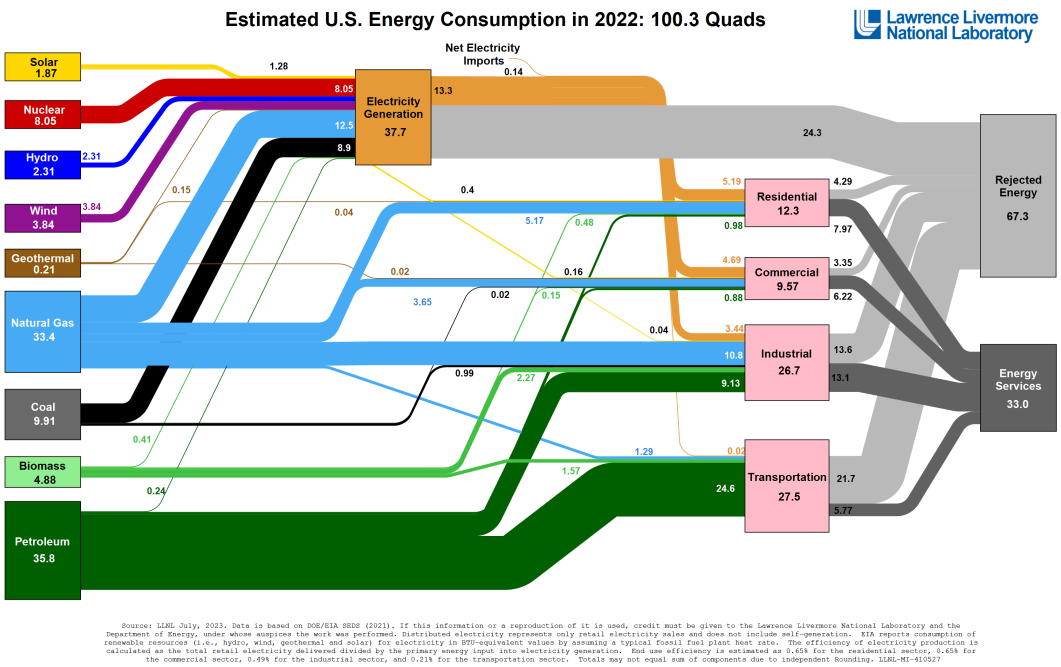


Source: LLNL July, 2023. Data is based on DOE/EIA SEDS (2021). If this information or a reproduction of it is used, credit must be given to the Lawrence Livermore National Laboratory and the Department of Energy, under whose auspices the work was performed. Distributed electricity represents only retail electricity sales and does not include self-generation. EIA reports consumption of renewable resources (i.e., hydro, wind, geothermal and solar) for electricity in BTU-equivalent values by assuming a typical fossil fuel plant heat rate. The efficiency of electricity production is calculated as the total retail electricity delivered divided by the primary energy input into electricity generation. End use efficiency is estimated as 0.65% for the residential sector, 0.65% for the commercial sector, 0.49% for the industrial sector, and 0.21% for the transportation sector. Totals may not equal sum of components due to independent Rounding. LLNL-MI-410527

Figure 1.1: United States energy consumption in 2022 by generation source and economic sector. The units are quadrillion BTUs. Rejected energy (shown in light gray) represents the waste energy from all inefficiencies. [1]

focused on in this project is hydrogen production via the Hybrid Sulfur (HyS) cycle. The HyS cycle is a thermochemical and electrical hybrid process to split water into hydrogen and oxygen by electrolyzing water mixed with sulfur dioxide to produce hydrogen and sulfuric acid, which is then decomposed at high temperature to produce oxygen and sulfur dioxide to continue the cycle. [8] In the HyS cycle, the sulfur is fully recycled which means that the net inflows to the system are water, electricity, and heat, with the net outflows being only hydrogen and oxygen. The major advantage of the HyS cycle is that greater energy efficiency can be obtained compared to conventional electrolysis of water. [9, 10] The limited operational experience of MSRs combined with that of the HyS cycle allows for increased value and importance for the modeling of these systems.

## 1.2 Summary of Scope

In this research project, a dynamic model was created for each of three the systems of the IES. These models were tested and debugged on their own, then combined into a single dynamic model to allow each of the interconnected systems to affect each other during a transient. The three systems in the IES model will be: 1) an MSR inspired by Terrapower's molten-chloride fast reactor (MCFR) design, 2) a HyS cycle hydrogen production plant, and 3) an electricity producing balance of plant (BOP) using a once-through steam generator and a regenerative Rankine heat cycle. The dynamic modeling methodology used was developed in previous work on a generic thermal spectrum MSR. [11] With the dynamic models, safety and safeguards related scenarios will be simulated. These scenarios are: reactivity initiated accidents (RIA), loss of flow accidents (LOFA), and loss of heat sink accidents (LOHSA) in regards to to the BOP and HyS systems as the heat sinks of the IES. The safeguards component of the work was originally focused on the aforementioned thermal spectrum MSR with the investigation of a novel technique for passively detecting plutonium signatures

using the offgas from the reactor. [12] The overall goal of this research is to improve the deployability of both MSRs and a nuclear IES.

## 1.3 Key Questions

The five key questions answered by this research are as follows:

- What are the barriers to the deployment of an IES with an MSR?

The barriers to deployment of an IES powered by an MSR can generally be grouped into four types: social, economic, technological, and regulatory. Social perceptions are expected to differ regionally, across age group, and may vary between specific technologies. Economic barriers will vary with specific technologies, but are at a higher price point and price uncertainty for nuclear power more broadly. The regulatory challenges for a nuclear IES in the United States primarily involve 10 CFR 50.34 and the inclusion of the industrial processes in the exclusion boundary radius. This project focuses particularly on technological issues generally relating to the safe, reliable, and accountable operation of an MSR in an IES. The topic is not focused on specifically within any chapter, but broadly throughout each chapter.

- What are the major safety concerns for an MSR in relation to heat transfer and what additional concerns are there for an MSR in an IES?

The major safety concerns for an MSR powered IES are primarily explored in Chapter 2, in which, a design-basis reactivity initiated accident, loss of flow accident, and loss of heat sink accidents are identified and evaluated. A loss of flow accident is assessed in further detail for a generic thermal spectrum MSR in Chapter 4. In that chapter, the results of a pump trip in the different coolant loops of the reactor are shown and discussed.

- What is the range of responses an IES may exhibit due to different heat sink failure modes between the systems of an IES?

The loss of each of the two heat sinks of the IES design are evaluated in Section 2.5.3 of Chapter 2. Specifically, the results of a loss of flow leading into the once-through steam generator of the regenerative Rankine cycle on the electrical production side of the IES, and the results of a loss of flow leading into the Bayonet decomposer of the hybrid sulfur cycle on the hydrogen production side of the IES.

- How do the frequency response characteristics of an IES differ compared to an MSR on its own and what effects does the size of the thermal manifold have on that difference?

This question is primarily answered through the entirety of Chapter 3, in which, the frequency response of the thermal power, electrical power, and hydrogen production rate are tested across six magnitudes of frequency with a standard transient. The dependency due to the mass of the thermal manifold is evaluated with the simulation set repeated for half the thermal manifold mass and once again with twice the thermal manifold mass.

- What techniques can be used to do safeguards for MSRs and how could they be implemented into the design and regular operation?

Safeguards techniques for MSRs are identified in Chapter 5. Specifically, a novel technique for passive non-destructive monitoring of the operating MSR is proposed and evaluated. The method of the technique is to observe the beta particles emitted in the MSR offgas to identify the relative concentration of different noble gas isotopes. These isotopes are then demonstrated to be used to determine the concentration of different fissile isotopes actively participating in fission within the core.

# Chapter 2

# Dynamic Modeling of a Fast Spectrum Molten Salt Reactor Integrated Energy System

*This chapter has been submitted as an individual journal article. It is currently under review by Nuclear Science and Engineering for an article collection on Nuclear Energy Research and Development at the University of Tennessee. I am the primary author. The other authors are Dr. Sandra Bogetic and Dr. Nicholas Brown. I primarily wrote the entire paper. Dr. Bogetic and Dr. Brown both helped review and improve the content of the paper. The only edit between the version presented here and that submitted to the journal is the removal of the abstract.*

## 2.1 Introduction

Nuclear energy can play a pivotal role in the green energy transition by providing safe, efficient, clean, and reliable power for a variety of heat intensive industrial uses. Dynamic modeling has unique potential to scope the operation and safety characteristics of systems with little to no operating experience. Presented in this paper is a dynamic model of an integrated energy system (IES) which uses an advanced nuclear reactor to produce both electricity and hydrogen. The purpose of this IES dynamic model is to provide information about the safety and efficiency of using nuclear power in an IES for uses beyond electricity production. This IES features both the low operating pressure of the molten salt reactor (MSR) and the negative reactivity feedback due to temperature. The latter feature is important in the accident scenarios simulated and presented in this work.

Broadly speaking, energy use in the economy can be divided into two categories: electricity generation and non-electric uses. Electricity generation tends to be produce less emissions per unit energy than non-electric applications, and as such, increasing the share of electricity in the total final energy consumption from 20% in 2022 to over 27% in 2030 is a goal in the Net Zero Emissions by 2050 (NZE) Scenario. [13, 14] The fact that low carbon energy is predominantly used for electricity generation necessarily means that non-electric uses remain dominated by fossil fuels. For example, in France during 2017, the amount of electricity generation from nuclear power was 79.6% of the total. [15] If combined with the electrical generation from solar, wind, hydro, and geothermal, the electricity generation from low carbon energy in France was 85.5% of the total for the year. However, the share of electricity in the total final energy consumption was 49.1% of the amount used in the economy for that year. The share of low carbon energy in non-electric energy uses was only 0.088%. Therefore, towards the goal of decarbonization, it is beneficial to both further the electrification of the economy and the broaden use of green energy outside of electricity generation.

The IES in this project is comprised of three systems: a generic fast spectrum MSR for heat generation, a regenerative Rankine cycle for electricity generation, and hydrogen production via the hybrid sulfur thermochemical cycle. The MSR design in this project is inspired by the commercial variant of Terrapower's Molten Chloride Fast Reactor (MCFR). [16, 17, 18] Some publicly available parameters for the MCFR-C design are used in this model to provide more realistic results, but the design and performance of our model is in no way meant to be representative of the MCFR. Further discussion on the design methodology of the fast spectrum MSR in this IES model and what parameters are from the MCFR is included in Section 2.3.1. The hydrogen production system utilizes a bayonet catalytic reactor for the decomposition stage of the hybrid sulfur cycle and a proton exchange membrane (PEM) for the electrolysis stage. [19, 20] Further discussion on the hydrogen production system is included in Section 2.3.2. The Rankine cycle in the model utilizes a once-through steam generator (OTSG) inspired by BWXT's design. [21] Further discussion on the electricity generation system is included in Section 2.3.3. The IES model used in this work is both lightweight and flexible. Simulations run quickly on workstations with approximately 500 seconds simulated per second actual when simulating a 10,000 second benchmark. The model tracks mass and heat flow throughout the system along with: neutron population, decay heat, and fission product poisons in the reactor; electricity production via the turbines in the balance of plant; and reaction rates in hydrogen production plant. The transients investigated in this work are: a rapid reactivity insertion, a loss of flow in the primary loop, a failure in the electricity generation system, and a failure in the hydrogen generation system.

## 2.2 Background

The research conducted in this paper is part of a Department of Energy Nuclear Energy University Program (NEUP) project on the topic of an MSR powered IES. Specifically, the title of the NEUP project is "Design and intelligent optimization of

the thermal storage and energy distribution for the TerraPower Molten Chloride Fast Reactor in an Integrated Energy System (IES)". [22, 23] The project is led by the University of Tennessee in collaboration with the University of Illinois at Urbana-Champaign (UIUC), Oak Ridge National Laboratory, and Terrapower. Further details on the goals of the NEUP project can be found in the project abstract. [24] The project began with an overall assessment of powering an IES with the MCFR and what chemical processes could potentially be driven by it. [25] Alongside that initial assessment is historical analysis on the use of nuclear reactors for industrial uses outside of electricity generation. Namely, the Aktau nuclear power plant in modern day Kazakhstan, which had over twenty years of operation powering both a desalination plant along the Caspian sea and producing electricity. [26]

The purpose of this paper in the context of the wider NEUP project is to demonstrate the IES dynamic model that has been developed in OpenModelica. Previously developed in this project is a neutronics model of a fast spectrum Chloride MSR similarly based upon the MCFR. [27, 28] The reactor system in the IES dynamic model presented here utilizes neutronics parameters (i.e. point kinetics, feedback coefficients, etc) from the fast Chloride MSR neutronics model. [29] Similarly, the HyS cycle hydrogen production system in the IES dynamic model is based on the HyS static model developed previously within this NEUP project. [30] In parallel with the IES dynamic model presented in this paper is a separate IES model that focuses on district heating and desalination. [31] In continuation of the project, there are plans to investigate the capability of an MCFR-like reactor to load follow according to real year long power usage data from the UIUC cluster high-performance computer system. Whereas this paper approaches accident analysis broadly in demonstration of the model's capabilities, progress has been made elsewhere in the project for postulating and investigating more specific transient events. [32]

The purpose of this paper in the context of the wider NEUP project is to demonstrate the IES dynamic model that has been developed in OpenModelica. Previously developed in this project is a neutronics model of a fast spectrum Chloride

MSR similarly based upon the MCFR. [27, 28] The reactor system in the IES dynamic model presented here utilizes neutronics parameters (i.e. point kinetics, feedback coefficients, etc) from the fast Chloride MSR neutronics model. [29] Similarly, the HyS cycle hydrogen production system in the IES dynamic model is based on the HyS static model developed previously within this NEUP project. [30] In parallel with the IES dynamic model presented in this paper is a separate IES model that focuses on district heating and desalination. [31] In continuation of the project, there are plans to investigate the capability of an MCFR-like reactor to load follow according to real year long power usage data from the UIUC cluster high-performance computer system. Whereas this paper approaches accident analysis broadly in demonstration of the model's capabilities, progress has been made elsewhere in the project for postulating and investigating more specific transient events. [32]

The dynamic modeling methodology utilized in this work was initially developed as part of a previous NEUP project on the development of material control and accountancy tools for liquid-fueled MSRs. [33, 34] The research in that project produced a generic thermal spectrum MSR, named NERTHUS, complete with a neutronic model and a dynamic model. [11] As part of the primary goal of that NEUP project, the model was used to determine Plutonium signatures in the primary loop offgas for novel safeguards techniques. [35] The model has also been used to the effects of loss of flow scenarios in the different loops. [36]. This research is in part further built upon in this paper through the inclusion of a loss of flow scenario in the primary loop of the MCFR-like reactor system. Both the NERTHUS reactor and the MCFR-like design in this work are liquid-fueled MSR systems. The primary difference between the two is that NERTHUS is thermal spectrum and the MCFR-like design is fast spectrum. The focus of this paper is on scoping analysis of the safety of using nuclear power for non-electric energy uses. However, the capability to load follow is an important capability for nuclear power to have in the field of electricity generation. [37] As such, the NERTHUS dynamic model has previously been used in a paper to investigate the potential for a liquid-fueled MSR to load follow. [38] The

focus of this work is scoping analysis of a fast spectrum MSR powering an IES. Of which, similar research is available on using a thermal spectrum high-temperature gas-cooled reactor. [39, 40]

There are many reasons why hydrogen is a promising energy carrier. The main three reasons are its energy content, environmental benefits, and flexibility. The energy content of hydrogen is 120 MJ per kilogram, compared to 46 MJ per kilogram of gasoline. [41] While the energy content of hydrogen is superior to gasoline, the volumetric energy density of liquid hydrogen is only 8 MJ per liter compared to 32 MJ per liter of gasoline. Despite that difference, it is useful to put it context with batteries. Lithium-ion batteries, commonly used in electric vehicles, have a mass energy density of about 0.72 MJ per kilogram or approximately 0.37 MJ per liter. [42] The environmental benefits of hydrogen are clear. Hydrogen is one of the few fuels that does not emit carbon from its combustion. However, the major environmental concern with hydrogen currently is that nearly all hydrogen commercially produced in the United States is made via steam-methane reforming, which produces carbon emissions. [43] Conversely, hydrogen production via nuclear power does not produce carbon. [44] The uses of hydrogen are varied and go beyond combustion and use in fuel-cells. [45] Hydrogen can also be used in industrial processes, such as the production of ammonia for fertilizer production. [46, 47]

## 2.3 Modeling Methodology

### 2.3.1 MCFR-like Dynamic Model

The reactor used in the IES model is a fast spectrum molten-salt reactor inspired by the commercial variant Terrapower's Molten Chloride Fast Reactor (MCFR-C). [18] The MCFR-C is still in development and the design parameters available from it are limited and have potential to change. [48, 49] As such, the generic fast spectrum molten-salt reactor model produced in this work should be considered similar to, but

not representative of, Terrapower's MCFR-C design. The neutronics parameters for our MCFR-like dynamic model come from a separate model based on the MCFR-C. [29] The shape, size, and relevant masses of the reactor design in this work is similarly based on the MCFR-C along with the eight primary heat exchangers. However, from there some engineering judgement must be used due to the lack of publicly available information for further heat exchangers and balance of plant that Terrapower is considering for the MCFR-C. For our reactor model, we have a single secondary heat exchanger that acts as a thermal manifold by connecting the heat flow from the reactor to the electricity production in the balance of plant and the hydrogen production unit, as shown in Figure 3.1.

In this section, the design methodology of the fast spectrum molten-salt reactor is explained in three pieces. Firstly, the point kinetics equations and the modifications to them necessary to represent circulating liquid fuel are described in Section 2.3.1. Next, the method of tracking fission product poisons, their effect on reactivity, and the reactivity feedbacks from temperature in the core are in Section 2.3.1. Finally, the mass and energy conservation equations for the heat transfer through the core and heat exchangers is included in Section 2.3.1.

### Modified Point Kinetics

Point kinetics are used to track the neutron population in the reactor model, but it is necessary to modify it to include the effect of circulating fuel. Delayed neutron precursors (DNP) flow with the liquid fuel salt out of the core, transit the primary loop, and then re-enter the core. Not all of the DNP would be expected to survive the transit. As such, two new terms are added to the DNP balance equation. These terms are the core residency time, $\tau_c$, and the loop transit time, $\tau_l$. With exception to the additional terms meant to include the effects of fuel circulation, the point kinetics equations used in the model are standard. [50]

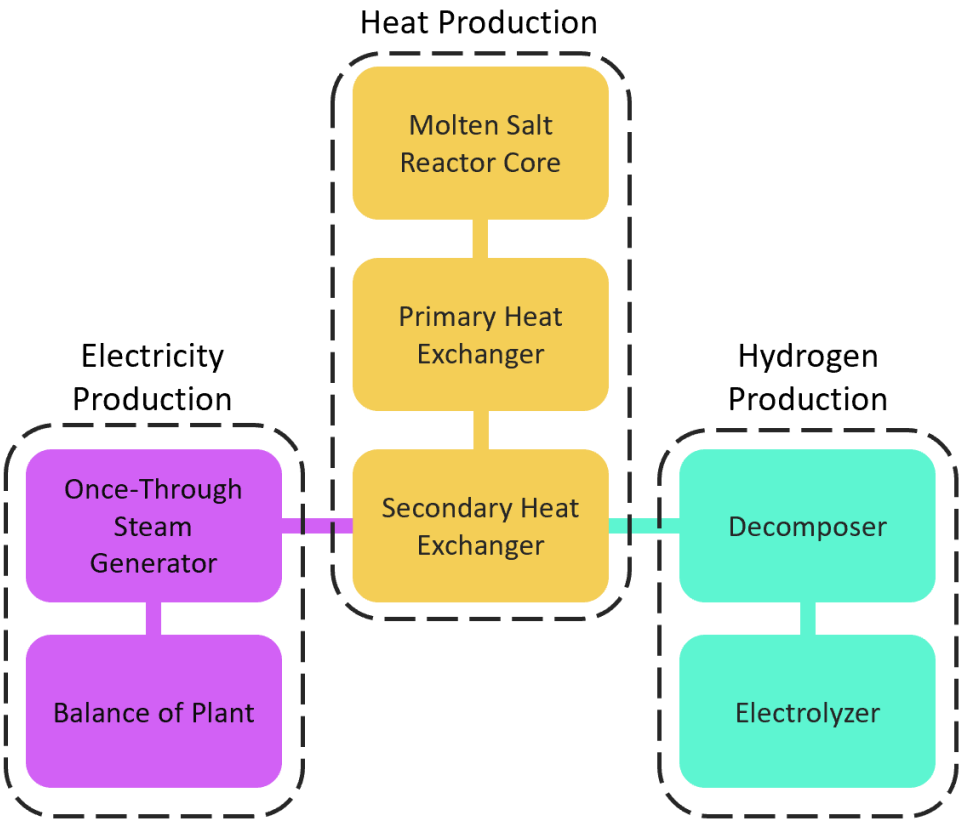


Figure 2.1: Arrangement of the three systems in the IES model, their connection through the secondary heat exchanger, and the organizational grouping of their components.

The detailed effects of circulating fluid fuel have been detailed in the literature. [51, 52, 53] The normalized neutron population is given by Equation 2.1, and the delayed neutron precursor concentration is given by Equation 2.2.

$$\frac{\partial n(t)}{\partial t} = \frac{\rho(t) - \beta}{\Lambda} n(t) + \sum_{i=1}^{6} \lambda_i C_i \tag{2.1}$$

$$\frac{\partial C_i(t)}{\partial t} = \frac{\beta_i}{\Lambda} n(t) - \lambda_i C_i(t) - \frac{C_i(t)}{\tau_c} + \frac{C_i(t - \tau_l) e^{-\lambda_i \tau_l}}{\tau_c} \tag{2.2}$$

In these equations, $n(t)$ is the neutron population at that point in time, $\rho(t)$ is the total reactivity relative to nominal conditions, $\beta$ is total delayed neutron fraction (i.e., $\sum_{i=1}^{6} \beta_i$), $\Lambda$ is the neutron generation time, $\lambda_i$ is the decay constant for the $i^{th}$ DNP group, $C_i(t)$ is the concentration for the $i^{th}$ DNP group, and $\tau$ is the fuel residence times within the core ($\tau_c$) and loop ($\tau_l$), respectively. All together, the four components affecting the delayed neutron precursor concentration are: [11]

1. The DNP production rate (proportional to the neutron population, delayed neutron fraction, and the neutron generation time)
2. Loss of precursor species due to decay
3. Advection of DNPs from the core
4. Re-introduction of the remaining DNPs retained following transit throughout the rest of the primary loop and are reentering the core (i.e., accounting for any lost to decay or chemical separation over the transit time)

Using the normalized neutron population, the instantaneous fission power can be determined with Equation 2.3. [50] In the equation, $w_f$ is the average energy released per fission event and $\nu$ is the average number of neutrons produced per fission event. To then determine the total reactor power, it is necessary to add the instantaneous fission power to the decay power at that time, shown in Equation 2.4.

$$n(t) \rightarrow P(t)_{fission} = w_f \nu \Sigma_f n(t) \tag{2.3}$$

$$P(t)_{total} = P(t)_{fission} + P(t)_{decay} \tag{2.4}$$

Heat production from fission product decay is tracked in a similar method to delayed neutron precursors. The fission products are separated into multiple decay heat precursor groups. Each group has an individual decay heat yield term and decay constant term. The summation of the production and removal of each group gives the change in decay heat production over time, as shown in Equation 2.5.

$$\frac{dP_d}{dt} = \sum_{i=1}^{N} [n(t)\ \delta_i - \lambda_i P_{d,i}(t)] \tag{2.5}$$

In the equation, $P_d$ is the total decay heat production as a fraction of the nominal reactor power, $N$ is the number of the decay heat precursor groups, $n(t)$ is the normalized neutron population, $\delta_i$ $[s^{-1}]$ is normalized relative decay heat yield of the $i^{th}$ decay group, and $\lambda_i$ $[s^{-1}]$ is decay constant of the $i^{th}$ decay group. The use of normalized neutron population is to allow direct coupling to the modified point kinetics.

### Reactivity Effects

The reactivity effect due to the circulation of the fuel salt out of the core, through the primary loop, and reentering the core is consistent at nominal conditions. There are two ways to conceptualize this reactivity effect; as negative reactivity due to the circulation rate or as the amount of positive reactivity necessary to compensate for circulation. In either regard, the total magnitude of the circulation effect is given by Equation 2.6.

$$\rho_0 = \beta - \sum_{i=1}^{6} \frac{\beta_i}{1 + \frac{1}{\lambda_i \tau_c}[1 - e^{-\lambda_i \tau_l}]} \tag{2.6}$$

In the equation, $\rho_0$ is the reactivity effect from circulation, $\beta$ is total delayed neutron fraction, $\beta_i$ is the delayed neutron fraction for the $i^{th}$ DNP group, $\lambda_i$ is the decay constant for the $i^{th}$ DNP group, and $\tau$ is the fuel residence times within the core ($\tau_c$) and loop ($\tau_l$), respectively. All together, the total reactivity in the reactor is the sum of the effect from external reactivity, $\rho_{ex}$; temperature related feedbacks, $\rho_{fb}$; circulation, $\rho_0$; and fission product poisons, $\rho_{FP}$, as shown in Equation 2.7.

$$\rho(t) = \rho_{ex} + \rho_{fb} + \rho_0 + \rho_{FP} \tag{2.7}$$

The temperature related feedbacks are the sum of the effect from the temperature of the fuel and the reflector, described in Equation 2.8.

$$\rho_{fb}(t) = \alpha_r(T_r(t) - T_{0,r}) + \alpha_f(T_f(t) - T_{0,f}) \tag{2.8}$$

In the equation, $\alpha_r$ is the reactivity feedback coefficient from temperature for the reflector, $\alpha_f$ is the reactivity feedback coefficient from temperature for the fuel, $T_r(t)$ is temperature of the reflector, $T_{0,r}$ is the nominal temperature of the reflector, $T_r(t)$ is temperature of the fuel, and $T_{0,r}$ is the nominal temperature of the fuel. The total temperature feedback coefficient is -4.4376$\times 10^{-5}$ for the fuel and 0.1164$\times 10^{-5}$ for the reflector. [29] The slightly positive reflector temperature coefficient is due to the reduction in density that lead experiences with increasing temperature. The density reduction has a spectral effect and leakage effect. Lower reflector density reduces moderation, which increases the increases the reproductive factor, $\eta$, for a fast reactor and thus is a positive reactivity effect. For leakage, lower reflector density increases leakage and thus is a negative reactivity effect. This understanding of the slightly positive reflector temperature coefficient is similar to that for SFR sodium voiding. [54]

The reactivity effect from a particular fission product poison is determined as a function of the concentration of that isotope relative to its concentration at nominal steady state conditions, shown for xenon in Equation 2.9 In the equation, $N_{Xe}(t)$ is

the current concentration, $N_{Xe}(t=0)$ is the steady state concentration, $\rho_{Xe}(t)$ is the reactivity effect due to xenon, and $\rho_{Xe,0}$ is a constant that determines the reactivity effect per change in concentration. The constant is determined as the absorptive cross section of the poison divided by that of the fuel, shown in Equation 2.10.

$$\rho_{Xe}(t) = \rho_{Xe,0}\left(\frac{N_{Xe}(t)}{N_{Xe(t=0)}} - 1\right) \tag{2.9}$$

$$\rho_{Xe,0} = -\frac{\Sigma_{Xe(0)}}{\Sigma_{a,Fuel}} \tag{2.10}$$

Two poisons are tracked within the model along with their primary parents. The two poisons are $^{135}Xe$ and $^{149}Sm$. The parents tracked for $^{135}Xe$ are $^{135}I$ and $^{135}Te$. The parent tracked for $^{149}Sm$ is $^{149}Pm$. The concentration of a particular isotope is the summation of direct production via fission, indirect production via decay from parents, removal via decay, and removal due to neutron absorption. The accounting of these isotopes is simplified due to all of the parents decaying solely via beta decay into the next isotope we are tracking.

The concentration of the parents are described by Equation 2.11, wherein, $N_i(t)$ is the concentration of the isotope, $\gamma_i$ is the fission yield for that isotope, $\Sigma_f(t)$ is the macroscopic fission cross section of the fuel, $\phi_0$ is the nominal flux density in the core, $n(t)$ is the normalized neutron population, and $\lambda_i$ is the decay constant for that isotope. Due to the half-life of $^{135}Te$ being magnitudes smaller than its daughter, $^{135}I$, it can be simplified by adding its fission yield to that of its daughter. Therefore, Equation 2.11 applies for $^{135}I$ and $^{149}Pm$.

$$\frac{\partial N_i(t)}{\partial t} = \gamma_i \Sigma_f(t) \phi_0 n(t) - \lambda_i N_i(t) \tag{2.11}$$

Similarly, the concentrations of $^{135}Xe$ and $^{149}Sm$ can be determined by Equations 2.12 and 2.13, respectively. There are multiple changes from the general equation for the parents. The first is the production from the decay of their parent added to

the direct production yield from fission. Next, as poisons, both have a removal term due to neutron absorption. For $^{149}Sm$, there is no decay term due to it being a stable isotope. For $^{135}Xe$, there is an additional removal term from removal via the offgas management system. As a noble gas, xenon is expected to be insoluble and form bubbles within the eutectic fuel salt mixture, rise out of it, and exit as offgas. The rate of removal this process provides is design specific and can be actively increased via sparging or other similar processes. [55, 56]

$$\frac{\partial N_{Xe}(t)}{\partial t} = \gamma_{Xe}\Sigma_f(t)\phi_0 n(t) + \lambda_I N_I(t) - \lambda_{Xe}N_{Xe}(t) - \sigma_a^{Xe}\phi_0 n(t)N_{Xe}(t) - \lambda_{gas}N_{Xe}(t) \tag{2.12}$$

$$\frac{\partial N_{Sm}}{\partial t} = \gamma_{Sm}\Sigma_f(t)\phi_0 n(t) + \lambda_{Pm}N_{Pm}(t) - \sigma_a^{Sm}\phi_0 n(t)N_{Sm}(t) \tag{2.13}$$

The nominal steady state concentrations of the two poisons is found simply by solving their accountancy equations for when the change in concentration is zero and the normalized neutron population is one. The concentrations of each of the isotopes of interest are then tracked at each simulation time step for the purpose of their reactivity effect. However, due to the hardened spectra of fast neutrons in the reactor, the absorption cross section of the poisons is magnitudes smaller and the reactivity effect would thus be minute. [57, 58]

### Heat Transfer

Tracking the heat transfer through the components is accomplished through mass and energy conservation equations. Components are characterized as a collection of solid and fluid control volumes (CV). The concept is based on Mann's Model of heat transfer, which was developed in the 1960s by ORNL for the Molten-Salt Reactor Experiment. [59, 60, 61, 62] In Mann's Model of heat transfer, fluid CVs are assumed to be well-mixed tanks which have homogeneous qualities throughout and

the temperature of the tank is the outlet temperature. Solid CVs are assumed to be thermally thin and have no temperature gradients within them. The arrangement of CVs in the core and primary heat exchanger (PHX) for our MCFR dynamic model are shown in Figure 2.2. In general, two fluid CVs are paired with a solid CV to collectively form one region. In the MCFR dynamic model, the core is a single heat transfer region and the primary heat exchanger is four regions with two on the primary side and two on the secondary side.

For a generic fluid CV, the temperature of that CV is found from the energy balance in and out of that CV, shown in Equation 2.14. In the equation, $m_f$ is the mass of fluid in that CV, $Cp_f$ is the specific heat of the fluid, $T_f$ is the temperature of the CV, $T_{in}$ is the temperature of the fluid flowing into that CV, $T_s$ is the temperature of the accompanying solid CV, $hA$ is the heat transfer coefficient times heat transfer area between the solid and fluid CV, and $T_{f,avg}$ is the average fluid temperature in that region. Assuming the fluid CVs are equivalent in size, the average fluid temperature is the temperature of the first fluid CV in that region. Using the primary heat exchanger in Figure 2.2 as an example, the average primary fluid temperature for the solid tube CV #1 is the temperature of PHX Fuel CV #1. For the secondary side, the average fluid temperature is the temperature of PHX Cool CV #1.

$$m_f Cp_f \frac{dT_f}{dt} = \dot{m}_f Cp_f (T_{in} - T_f) + hA(T_s - T_{f,avg}) \tag{2.14}$$

For the fluid CVs in the primary loop, the presence of fission products in the fuel salt adds decay heat into the energy balance. The change in the temperature of the fluid CV due to decay heat is given by Equation 2.15. In the equation, $P_d$ is the decay heat fraction normalized to the nominal reactor power $P_{core}$, $m_{total}$ is the total fuel salt mass, and $Cp_f$ is the specific heat of the fuel salt. The total fuel salt mass is used due to the decay heat being distributed throughout and not localized in that CV. The fuel salt mass for that CV is on both sides of the equation and thus cancels

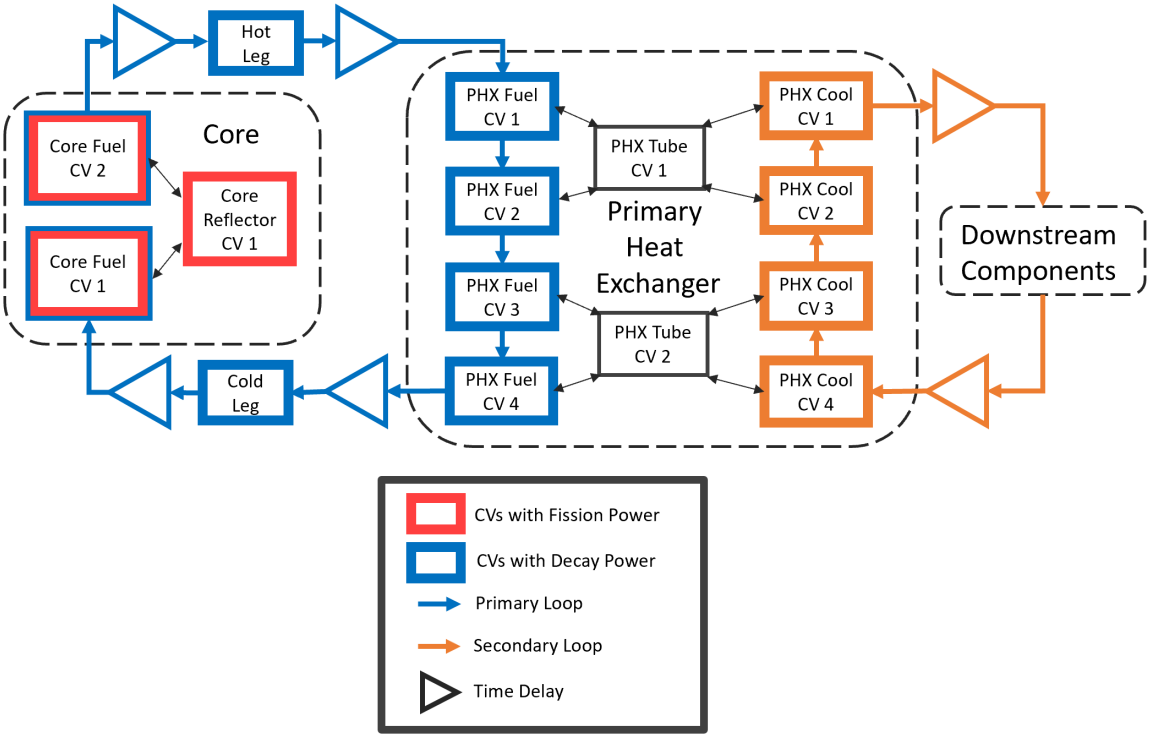


Figure 2.2: Arrangement of solid and fluid control volumes in the reactor core and primary heat exchanger as components within the IES model. Fission power is only within the core, whereas decay power is throughout the primary loop.

out. All together, the temperature of the fluid CVs on the primary side of the PHX is given by Equation 2.16.

$$\left(\frac{dT_f}{dt}\right)_{decay} = \frac{P_d \cdot P_{core}}{m_{total} \cdot Cp_f} \tag{2.15}$$

$$m_f Cp_f \frac{dT_f}{dt} = \dot{m}_f Cp_f (T_{inlet} - T_f) + hA(T_s - T_{f,avg}) + \frac{P_d \cdot P_{core}}{m_{total} \cdot C_f} \tag{2.16}$$

The temperature of the solid CVs, representing the tubing or walls between the primary fluid and secondary fluid, is determined by Equation 2.17, wherein, $m_s$ is the mass of the solid CV, $Cp_s$ is the specific heat of the solid, $T_s$ is the temperature of the solid, $hA_1$ is the heat transfer coefficient times heat transfer area between the solid and the primary fluid CV, $hA_2$ is the heat transfer coefficient times heat transfer area between the solid and the secondary fluid CV, $T_{f1,avg}$ is the average fluid temperature on the primary side, and $T_{f1,avg}$.

$$m_s Cp_s \frac{dT_s}{dt} = hA_1(T_{f1,avg} - T_s) - hA_2(T_s - T_{f2,avg}) \tag{2.17}$$

### Salt Parameters

The IES uses three types of salts, which are compared in Table 2.1. In the primary loop, the salt is a binary eutectic of sodium chloride (66.7 mol%) and uranium(III) chloride (33.3 mol%). The primary loop salt, also referred to as fuel salt, is currently being investigated for use in Terrapower's MCFR-C. [48] The salt used in the secondary loop, also known as secondary salt or coolant salt, was picked for its operating temperature range and its similarity to the fuel salt, with exclusion of the fissile material. The secondary salt is sodium chloride (20.5 mol%), potassium chloride (41.3 mol%), and magnesium chloride (38.2 mol%) in a ternary eutectic. [63, 64] This salt is being experimentally tested as a promising candidate for use in next generation

Table 2.1: The three salts used in the IES model, their location, chemical composition, specific heat capacity, and melting point.

| Salt Location | Chemical Composition | Specific Heat Capacity $[\frac{MJ}{kg \cdot °C}]$ | Melting Point |
|---|---|---|---|
| Primary Loop | NaCl-$UCl_3$ | $6.6065e^{-4}$ | 523 °C |
| Secondary Loop | NaCl-KCl-$MgCl_2$ | $1.1e^{-3}$ | 385 °C |
| Tertiary Loop | $KNO_3$-$NaNO_2$-$NaNO_3$ | $1.54912e^{-3}$ | 142 °C |

high temperature concentrated solar power systems. [65] Lastly, the tertiary salt, formally known as HITEC solar salt [66], is a eutectic mixture of potassium nitrate (53 mol%), sodium nitrite (40 mol%), and sodium nitrate (7 mol%).

The reasoning behind the use of these three salts in the IES model is a combination of realism and practicality. The reactor used in the IES is based on the MCFR, and as such, it was prudent to use the sodium chloride and uranium chloride mixture that Terrapower has been investigating. The secondary salt was picked due to its similarity to the fuel salt and the availability of thermophysical parameters for it. The fuel salt and coolant salt being similar is relevant due to the safety concerns relating to a leak in the primary heat exchanger causing mixing. If some mixing occurred, the expectation is that the similar nature of the salts would minimize undesired effects. However, the IES model is not capable of simulating that event. The major purpose of having a secondary loop is to separate the fissile materials further from the balance of plant. This benefit is increasingly important in an IES, where the heat usage is beyond the reactor building itself. In an industrial setting, where the IES design presented in this work is used, the hydrogen production system would likely be in a different building nearby. As such, the existence of the tertiary loop mirrors the benefits of the secondary loop in having layers of defense between the fissile materials and the outside. The salt used in the tertiary loop of this model, HITEC solar salt, has well-known parameters and is currently used in the solar energy industry. [66] The flow rates and masses of each of the three salts used in the IES model are shown in Table 2.2.

### 2.3.2 Hybrid Sulfur Cycle Dynamic Model

The design depicted in this model is a generic hydrogen production plant utilizing the hybrid sulfur cycle. [67, 19] The methodology builds upon past research on static models. [68, 30] This system receives high temperature molten salt, water, and electricity then outputs hydrogen, oxygen, and molten salt at a lower temperature.

Table 2.2: Salt Flow Rates and Masses Parameters

| | |
|---|---|
| Nominal Thermal Power | 1200 MW |
| Avg Core Inlet Temp | 680 °C |
| Avg Core Outlet Temp | 720 °C |
| Primary Loop Nominal Flow Rate | 45,000 kg/sec |
| Secondary Loop Nominal Flow Rate | 27,272.73 kg/sec |
| Tertiary Loop Nominal Flow Rate | 12,910.56 kg/sec |
| Total Primary Loop Fluid Mass | 638,300 kg |
| Total Fluid Mass in Core | 319,150 kg |
| Total Secondary Loop Fluid Mass | 981,814 kg |
| Total Tertiary Loop Fluid Mass | 465,975 kg |

Within the system, feed fluid goes through a decomposer, which separates sulfuric acid into sulfur dioxide, oxygen, and water. The oxygen is removed via a separator. The sulfur dioxide and water then goes through a condenser, which lowers the temperature. The flow then enters an electrolyzer where, along with an inlet flow of makeup water, completes an electrolysis reaction to convert the sulfur dioxide and water into hydrogen gas and sulfuric acid. The hydrogen is then removed as the primary product, and the sulfuric acid then flows back into the decomposer to complete the cycle. Across the cycle, all sulfur is recycled and the only material inflows and outflows are water, oxygen, and hydrogen, respectively.

### Decomposition

The decomposer is essentially a counterflow heat exchanger which has high temperature molten salt on one side and the working fluid of the hybrid sulfur cycle on the other side. What differentiates the decomposer from a typical heat exchanger is that the fluid on the secondary side is sulfuric acid and water. It inflows as a liquid, fully boils, is superheated, and also undergoes up to two endothermic chemical reactions. The first of these reactions is the decomposition of sulfuric acid into sulfur trioxide and water. The second reaction is the conversion of the sulfur trioxide into sulfur dioxide and oxygen.

As shown in Figure 2.3, the model represents the decomposer as a collection of CVs, similar to the heat exchangers in Section 2.3.1. The fluid CVs are considered well-mixed tanks which have homogeneous properties within the CV.

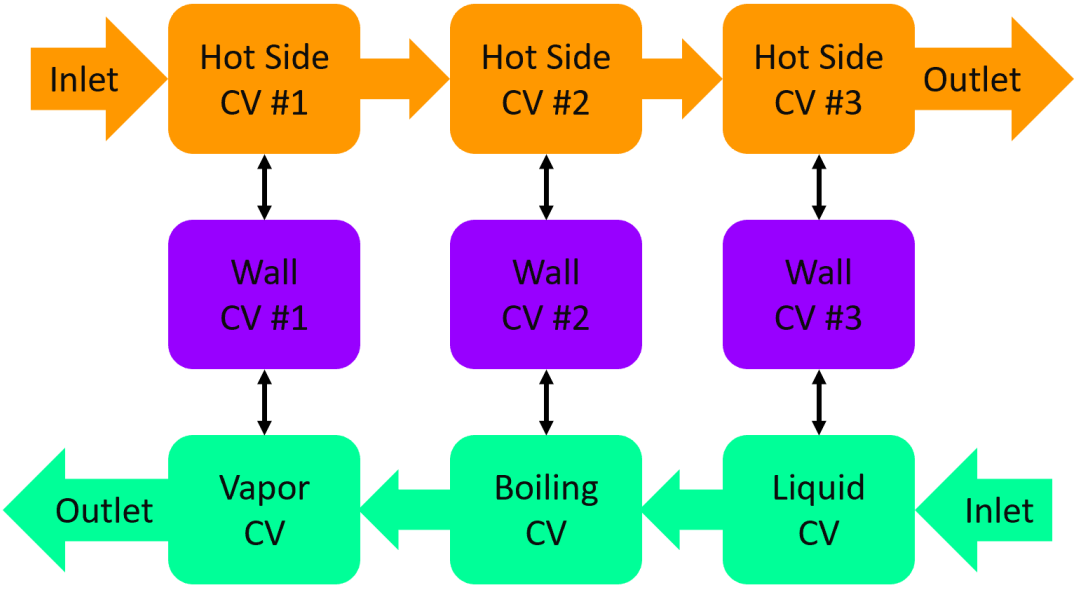


Figure 2.3: Arrangement of the solid and fluid control volumes (CVs) comprising the decomposer component of the Hybrid Sulfur cycle system in the IES model.

The calculated temperature of the CV is the outlet temperature of tank and the average temperature between the inlet and outlet is assumed to be halfway between the two. For solid CVs, they are assumed to be thermally thin with homogeneous properties throughout the CV. Specifically, there is no internal thermal gradient within the solid CV.

*Primary Side (Hot CVs)*

The temperatures of the three fluid CVs on the primary side of the decomposer is calculated and tracked independently as time-dependent differential equations. The temperature of the three CVs are determined by Equations 2.18, 2.19, and 2.20, respectively. The equations are derived from conservation of mass and energy. Specifically, the units of each term simplifies to watts. Collectively, they incorporate the balance of heat flowing in and out of the CV in the fluid, the heat flowing through the tubing (i.e., Wall CVs), and the change in temperature of the fluid in that CV.

$$m_{H1} \cdot Cp_H \cdot \frac{dT_{H1}}{dt} = \dot{m}_H \cdot Cp_H \cdot (T_{H,inlet} - T_{H1}) - \frac{hA_{outer}}{w} \cdot (\frac{T_{H,inlet} + T_{H1}}{2} - T_{W1}) \quad (2.18)$$

$$m_{H2} \cdot Cp_H \cdot \frac{dT_{H2}}{dt} = \dot{m}_H \cdot Cp_H \cdot (T_{H1} - T_{H2}) - \frac{hA_{outer}}{w} \cdot (\frac{T_{H1} + T_{H2}}{2} - T_{W2}) \quad (2.19)$$

$$m_{H3} \cdot Cp_H \cdot \frac{dT_{H3}}{dt} = \dot{m}_H \cdot Cp_H \cdot (T_{H2} - T_{H3}) - \frac{hA_{outer}}{w} \cdot (\frac{T_{H2} + T_{H3}}{2} - T_{W3}) \quad (2.20)$$

Within the equations, $m_H$ is the mass of the CV, $\dot{m}_H$ is the fluid flow rate, $Cp_H$ is the specific heat of the fluid, $hA$ is the heat transfer coefficient times heat transfer area between the solid and fluid CV, and $T_W$ is the temperature of the adjacent wall CV. The fluid on the primary side of the decomposer, the tertiary loop salt, is HITEC

solar salt. [66] This salt is used in the tertiary loops between the secondary side of the SHX, the primary side of the OTSG, and the primary side of the decomposer. At nominal steady state conditions, the temperature of the fluid entering the primary side of the decomposer is 634.75°C.

*Tubing (Wall CVs)*

The temperature of each of the wall CV is tracked independently, but the form differs slightly with each one due to the state of the adjacent secondary side CV. The CVs are referred to as wall CVs instead of tubing to prevent confusion due to other instances of the letter T that are relevant in the equations. For clarity, the determination of the three wall CVs are explained in order of #3, #2, and #1. The reason for this decision is due to that being the order in which the fluid on the secondary side passes by them.

Due to the temperature of the adjacent liquid CV being defined as the outlet temperature of the CV, the temperature of the liquid CV must be the boiling temperature of the fluid. Therefore, to track the energy transfer through the wall CV#3, the temperature difference between the inlet temperature and the boiling temperature is used. This simplification results in the tracking of the temperature of the third wall CV to be given by Equation 2.21.

$$m_{W3} \cdot Cp_W \cdot \frac{dT_{W3}}{dt} = hA_{outer} \cdot (\frac{T_{H2} + T_{H3}}{2} - T_{W3}) - \dot{m}_{liq} \cdot Cp_{liq} \cdot (T_{boil} - T_{L,inlet}) \quad (2.21)$$

In the equation, $m_{W3}$ is the mass of the wall CV#3, $Cp_W$ is the specific heat of the wall, $T_{W3}$ is the temperature of the CV, $T_{H2}$ is the temperature of the second primary side CV, $T_{H3}$ is the temperature of the third primary side CV, $\dot{m}_{liq}$ is the mass flow rate through the liquid CV, $Cp_{liq}$ is the specific heat of the fluid in the liquid CV, $T_{boil}$ is the boiling temperature of the fluid, and $T_{L,inlet}$ is the inlet temperature of the feed flowing into the secondary side of the decomposer.

The tracking of the temperature of the second wall CV is shown in Equation 2.22. The temperature of the boiling CV does not change due to our assumption that only phase change is occurring there. Thus, the fluid enters and exits at saturation temperature. As such, the final term of the equation is the rate of energy used to fully boil the fluid that has entered the CV. The power used to do so is detailed in Equation 2.23.

$$m_{W2} \cdot Cp_W \cdot \frac{dT_{W2}}{dt} = hA_{outer} \cdot (\frac{T_{H1} + T_{H2}}{2} - T_{W2}) - \dot{E}_{boil} \tag{2.22}$$

$$\dot{E}_{boil} = \dot{m}_{SA} \cdot H_{vap,SA} + \dot{m}_{water} \cdot H_{vap,water} \tag{2.23}$$

In these equation, $\dot{E}_{boil}$ is the energy necessary to fully boil the fluid within the CV, $\dot{m}_{SA}$ is the flow rate of sulfuric acid, $H_{vap,SA}$ is the enthalpy of vaporization of sulfuric acid at the operating pressure, $\dot{m}_{water}$ is the flow rate of water, and $H_{vap,water}$ is the enthalpy of vaporization of water at the operating pressure. The pressure within the HyS system can be changed, but the nominal condition for the simulations in this paper is 100 kPa. The sensitivity of the HyS cycle has been shown to be dependent on the operating pressure and temperature, but further analysis is beyond the scope of this work. [67, 68, 30]

Lastly, the equation for tracking the temperature of the first wall CV is shown in Equation 2.24.

$$m_{W1} \cdot Cp_W \cdot \frac{dT_{W1}}{dt} = hA_{outer} \cdot (\frac{T_{H,inlet} + T_{H1}}{2} - T_{W1}) - hA_{inner} \cdot (\frac{T_{boil} + T_{vap}}{2} - T_{W1}) - X \cdot \dot{M} \cdot (Q_{rxn1} + Q_{rxn2}) \tag{2.24}$$

In the equation, $m_{W1}$ is the mass of the wall CV, $Cp_W$ is the specific heat of the wall, $T_{W1}$ is the temperature of the wall CV, $hA_{outer}$ is the heat transfer coefficient

times the heat transfer area on the outer side of the wall, $hA_{inner}$ is the heat transfer coefficient times the heat transfer area on the inner side of the wall, $T_{H1}$ is the temperature on the primary side hot CV#1, $T_{boil}$ is the boiling CV temperature, $T_{vap}$ is the vapor CV temperature, $\dot{M}$ is the sulfuric acid feed flow rate in mols per second, $Q_{rxn1}$ is the energy used per mole in the first decomposition reaction (sulfuric acid to water and sulfur trioxide), $Q_{rxn2}$ is the energy used per mole in the second decomposition (sulfur trioxide to diatomic oxygen and sulfur-dioxide), and $X$ is the fraction of the sulfuric acid feed that successfully decomposes into sulfur dioxide. The fraction of sulfur trioxide that does not convert is assumed to do the reverse of the first reaction. In the reverse form, the reaction recycles some of the energy via reheating. This process is incorporated in the equation via the X term reducing the energy demand of the first reaction. Further details on the energy balance relating to the decomposition reactions are included in the discussion of the secondary side of the decomposer.

*Secondary Side (Cold CVs)*

Due to our assumptions relating to the properties within each CV, the temperature of the liquid CV and boiling CV have previously been determined to be the saturation temperature of the combined fluid (i.e., water and sulfuric acid). Therefore, the vapor CV is the only temperature left to determine on the secondary side of the decomposer. The energy used by the vapor CV has already been accounted for in Equation 2.24. It can also be assumed that the temperature of the wall CV is halfway between that of the two fluid CVs it is adjacent to. As such, the temperature of the vapor CV is determined by Equation 2.25.

$$T_{vap} = T_{H1} - 2(T_{H1} - T_{W1}) \tag{2.25}$$

Next, it is necessary to determine the energy used to complete one mole of each reaction. This determination is accomplished by finding the change in specific heat

of each of the products compared to the reactants, then adding the enthalpy of the reaction, as shown in Equations 2.26 and 2.27.

$$Q_{rxn1} = H_{rxn1} + (Cp_{H2O} + Cp_{SO3} - Cp_{H2SO4})(T_{vap} - T_{ref}) \tag{2.26}$$

$$Q_{rxn2} = H_{rxn2} + (-Cp_{SO3} + Cp_{SO2} + 0.5 \cdot Cp_{O2})(T_{vap} - T_{ref}) \tag{2.27}$$

In these equations, $Q_{rxn1}$ is the energy required to complete one mole of the first decomposition reaction (i.e., sulfuric acid to water and sulfur trioxide), $Q_{rxn2}$ is the energy required to complete one mole of the second decomposition reaction (i.e., sulfur trioxide to sulfur dioxide and oxygen), $H_{rxn1}$ is the heat of reaction for the first decomposition reaction, $H_{rxn2}$ is the heat of reaction for the second decomposition reaction, $T_{ref}$ is the reference temperature for standard enthalpy, and $Cp$ is the specific heat for each of the chemicals as a function of temperature determined by the Shomate equations with constants from NIST. [69, 70].

The first reaction is assumed to progress fully to completion, but the second reaction is not. To determine the conversion ratio of sulfur trioxide decomposed into sulfur dioxide, the reaction equilibrium constant, $K_c$, is used in Equation 2.28. Within the equation, $X$ is the ratio of successful conversion and $P$ is the pressure in the vapor CV.

$$K_c \cdot e^{[\frac{Q_{rxn2}}{R}(\frac{1}{T_{ref}} - \frac{1}{T_{vap}})]} = \frac{[4.86 * 10^{-5} \cdot P(\frac{X}{1+\varepsilon X})(\frac{1173}{T_{vap}})][4.86 * 10^{-5} \cdot P(\frac{0.5 \cdot X}{1+\varepsilon X})(\frac{1173}{T_{vap}})]^{0.5}}{[4.86 * 10^{-5} \cdot P(\frac{1-X}{1+\varepsilon X})(\frac{1173}{T_{vap}})]} \tag{2.28}$$

This equation is taken from other research focused on the HyS cycle and developing static models with it. The methodology behind this form of the equilibrium equation is discussed further therein. [30, 68] To validate the HyS cycle dynamic model produced in this work, the sulfur trioxide conversion ratio, $X$, has been calculated across a range of pressures and vapor temperatures, then compared to

the afforementioned static models. The results of the HyS validation are shown in Figure 2.4.

The results of the HyS validation tests demonstrate that the model produced in this work is in agreement with the other two models it is being compared to. In particular, the overall S-curve shape is seen for each pressure and the curve is similarly shifted rightward at higher pressures. There is comparably less agreement between 500°C and 800°C, and again at the highest temperatures, above 1000°C. However, the HyS cycle model is a low-fidelity dynamic model with simplifying assumptions made to allow rapid computation even when coupled with separate heat and electricity generation systems in one single model. The fact that this HyS remains overall comparable to the other two models, which are higher fidelity static models focused solely on the HyS cycle, demonstrates that the simplifying assumptions are valid and effective. At the nominal operating temperature of a vapor CV temperature of 593°C, the model presented in this work gives a lower conversion ratio than the other two models. Therefore, any hydrogen production results from this model may be seen as slightly underestimated.

*Mass Balance*

The equations explained thusfar are based on energy and mass conservation. Due to the chemical reactions taking place in the decomposer and the separation of the different chemicals after, some specific attention must be made to the mass balance through the system. The mols of net decomposition reaction occurring per second is determined by Equation 2.29, in which, $Wt\%$ is the weight percentage of sulfuric acid (H2SO4) in the incoming fluid stream coming from the boiling region, $\dot{m}_{boil}$, which is in units of kilograms per second. From there, $M_{H2SO4}$ is the molar mass of sulfuric acid, which is 98.079 grams per mol. [69]

$$\dot{M} = \frac{\dot{m}_{boil} \cdot Wt\%}{M_{H2SO4}} \tag{2.29}$$

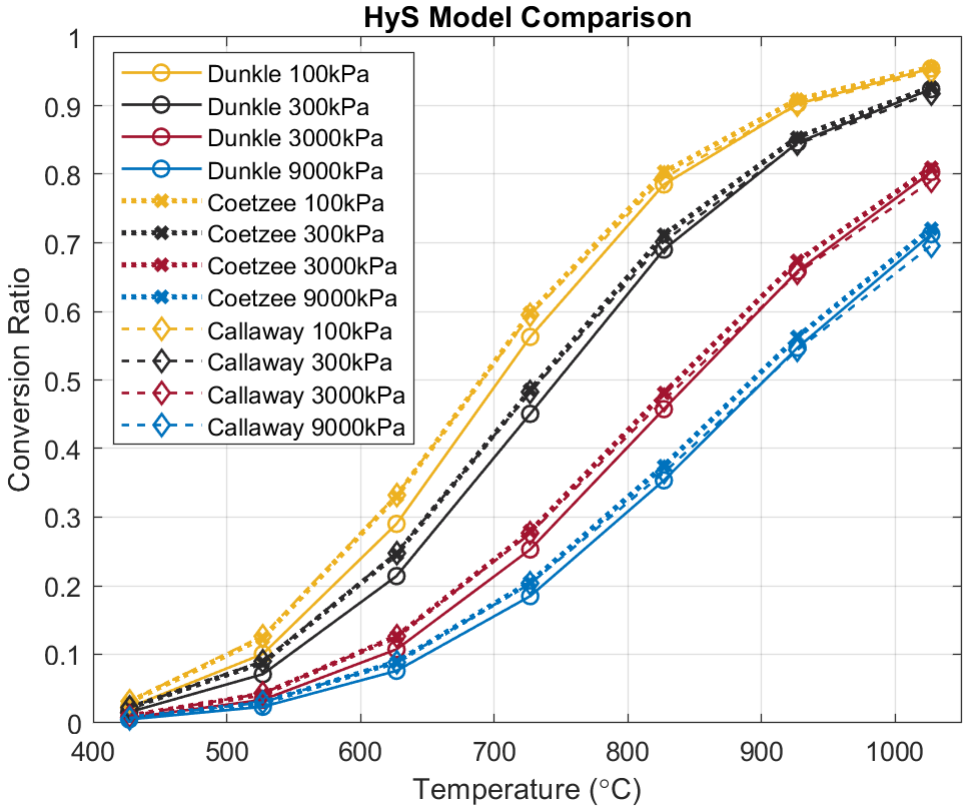


Figure 2.4: The sulfuric acid to sulfur-dioxide conversion ratio, $X$, as determined by the equilibrium constant equation across a range of temperatures and pressures. Results shown with solid lines and circles are from this model. Results shown in dotted lines with crosses is from Coetzee (2008). Results shown in dashed lines with diamonds is from Callaway (2024).

The previously determined value, $\dot{M}$, is the mols of sulfuric acid entering the decomposer. The rate of reaction occurring within the decomposer is thus the rate of sulfuric acid entering times the conversion ratio, $X$. This relationship is then used to calculate the mols of the different compounds leaving the decomposer. This determination is done with the sulfur trioxide conversion ratio, $X$, and the stoichiometric ratios of the participants. The resulting equations are shown as Equations 2.30, 2.31, 2.32, and 2.33.

The rate of sulfuric acid leaving the decomposer is the fraction of the sulfuric acid that did not convert times the rate of sulfuric acid entering the decomposer, given by Equation 2.30.

$$\dot{M}_{H2SO4} = \dot{M} \cdot (1 - X) \tag{2.30}$$

For every one mole of sulfuric acid that reacts, one mole of water is produced. Water is also entering the decomposer along with the sulfuric acid. The amount of water leaving the decomposer per second is therefore the sum of these two, given in Equation 2.31.

$$\dot{M}_{H2O} = \dot{M} \cdot X + \frac{\dot{m}_{boil} \cdot (1 - Wt\%)}{M_{H2O}} \tag{2.31}$$

The determination of the rate of sulfur dioxide from the decomposer is simply equal to the amount of sulfuric acid that reacted within the decomposer, given by Equation 2.32.

$$\dot{M}_{SO2} = \dot{M} \cdot X \tag{2.32}$$

For every two moles of sulfuric acid that reacts, only one mole of diatomic oxygen is produced, as given in Equation 2.33.

$$\dot{M}_{O2} = \frac{\dot{M} \cdot X}{2} \tag{2.33}$$

The outflow of the decomposer is sulfur dioxide, water, oxygen, sulfur trioxide, and sulfuric acid. The water and aqueous sulfur dioxide are both sent through the condenser and then to the electrolyzer for the electrolysis side of the HyS cycle. The oxygen outflow from the decomposer is removed from the cycle as a byproduct. The sulfur trioxide is sent through the recuperation side of the bayonet decomposer to recombine with water, which produces heat that is refunded into the decomposer. The product of the recuperation is sulfuric acid, which along with the sulfuric acid that came out of the decomposer, is recycled back into the decomposer. The net products of the decomposer are thus oxygen, water, and sulfur-dioxide.

### Electrolysis

On the electrolysis side of the HyS cycle system, the important variables to determine are the electric power demands, the hydrogen production rate, and the amount of supplementary water necessary to continue the reaction at nominal conditions. The electric energy necessary to successfully react one mole of the reaction is determined with a form of the Gibbs free energy equation, shown in Equation 2.34.

$$dH_0 = dG_0 + T \cdot dS = zFE^0_{cell} + T[(S_{H2SO4} + S_{H2}) - (S_{SO2} + 2S_{H2O})] \tag{2.34}$$

In the equation, the units of $dH_0$ is joules per mole. The desired cell potential for PEM electrolysis, $E^0_{cell}$ is equal to 0.6 V. [20] Each of the entropy constants, $S$, are determined using Shomate equations with constants (A, B, C, D, E, and F) acquired from NIST, in the from of Equation 2.35, in which, $t$ is the temperature of the fluid divided by 1000. [69]

$$S_i = A \cdot log(t) + B(t) + \frac{C(t)^2}{2} + \frac{D(t)^3}{3} + \frac{E}{2(t)^2} + F \tag{2.35}$$

From there, the nominal electric power demand is thus the energy necessary to complete one mole of the electrolysis reaction times the moles per second inflow of sulfur dioxide, $\dot{M}$, as shown in Equation 2.36. In this equation, it is assumed that the sulfur dioxide is fully reacting. As such, with ample water and power, the limit to the reaction is the inflow rate of sulfur-dioxide.

$$P_{nom} = dH_0 \cdot \dot{M} \tag{2.36}$$

One mole of water is necessary to complete one mole of the reaction. Thus, the rate of water consumed by the reaction is equal to the inflow rate of sulfur dioxide. Water is flowing into the electrolyzer via the condenser, but it is not enough to sustain the reaction due to mass losses from the production of diatomic hydrogen and diatomic oxygen. Supplementary water is therefore necessary to continue the cycle. The rate of supplementary water required to sustain the reaction is given by Equation 2.37. In the equation, $M_{H2O}$ is the molar mass of water, $\dot{M}$ is the rate of the decomposition reaction in moles per second, and $\dot{m}_{H2O}$ is the rate of water usage in units of kilograms per second.

$$\dot{m}_{H2O} = \frac{2 \cdot \dot{M}}{M_{H2O}} \tag{2.37}$$

Lastly, the amount of hydrogen produced by the hybrid sulfur system is determined by Equation 2.38. In the equation, $M_{H2}$ is the molar mass of hydrogen gas and $\dot{m}_{H2}$ is the rate of hydrogen production in units of kilograms per second.

$$\dot{m}_{H2} = M_{H2} \cdot \dot{M} \tag{2.38}$$

### 2.3.3 Rankine Balance of Plant Dynamic Model

In the dynamic model, the electricity producing system utilizes the regenerative Rankine cycle. [71] The system operates by receiving hot salt from the secondary

heat exchanger, using it to produce superheated steam, and then running that steam through two sets of turbines and accompanying regenerative components. The steam generator used in this model is a once-through steam generator (OTSG) inspired by BW&T's design. [21] The specific modeling methodology of the OTSG is discussed further in the next section. The remainder of the balance of plant components are: the steam valve, high pressure turbine (HPT), low pressure turbine (LPT), moisture separator, reheater, condenser, and feedwater heater. The overall design and methodology builds upon similar models. [72, 73, 74]

### Once-Through Steam Generator

The OTSG is characterized as a group of control volumes (CV) that transfer mass and energy between each other. The methodology is similar to that used for the heat exchangers discussed in Section 2.3.1. The same assumptions are used here: fluid CVs are well-mixed tanks and solid CVs are thermally thin. The important difference between the OTSG methodology and that of the other heat exchangers is that the secondary side of the OTSG experiences two-phase flow. Subcooled feedwater enters the OTSG, is heated to saturation temperature, fully boiled, and then heated further into high quality superheated steam, which then exits the OTSG. To represent the two-phase flow, it is necessary to increase the number of CVs for each state. The arrangement of CVs in the OTSG is shown in Figure 2.5. A key difference between the OTSG and the other heat exchangers in the IES is the inclusion of a moving boundary approximation where the lengths of each CV can change depending on the two-phase flow conditions on the secondary side.

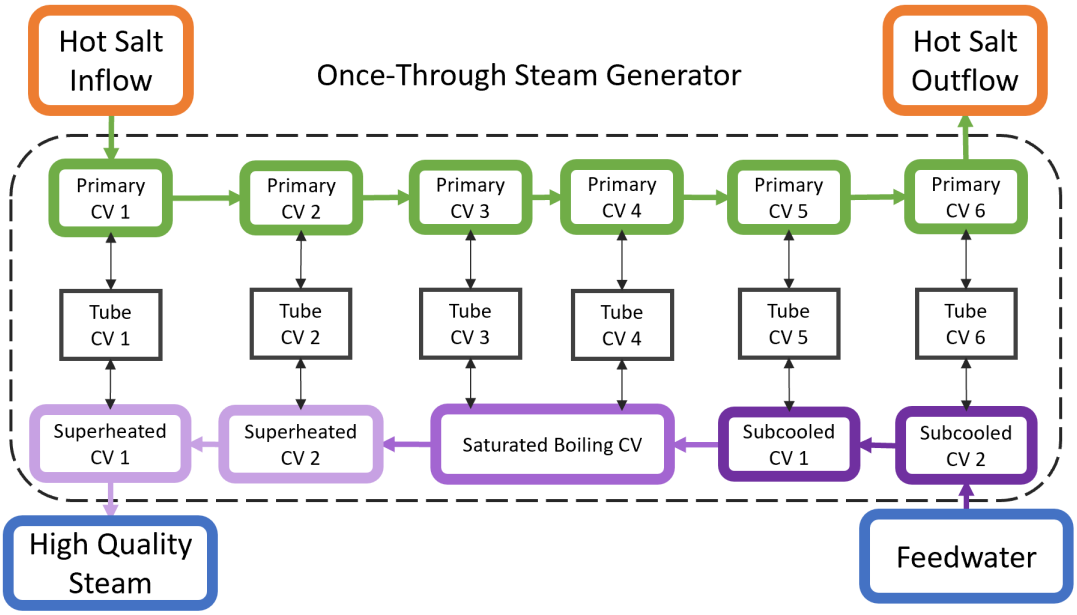


Figure 2.5: Arrangement of the solid and fluid CVs comprising the OTSG component within the regenerative Rankine cycle electrical production system in the IES model.

*Primary Side*

Hot molten-salt enters the primary side of the OTSG, transfers heat through the tubes, and then exits to return to the SHX. The temperature is determined in the same way as with the other heat exchangers, with mass and energy accountancy, shown in Equation 2.39, wherein, $m_p$ is the mass of the molten salt in that CV, $Cp_p$ is the specific heat capacity of the salt, $T_p$ is the temperature of the salt in that CV, $T_{in}$ is the temperature of the salt flowing into that CV, $hA_{pt}$ is the heat transfer coefficient times heat transfer area between the fluid on the primary side and the tubing for that CV, and $T_t$ is the temperature of the tubing adjacent to that CV.

$$m_p Cp_p \frac{dT_p}{dt} = \dot{m}_p Cp_p (T_{in} - T_p) + hA_{pt}(T_t - T_p) \tag{2.39}$$

*Tubing*

Similarly, the temperature of one of the tubing CVs is found via the accountancy of the heat flowing into it from the primary fluid, and the heat flowing out of it and into the secondary fluid, as shown in Equation 2.40, wherein, $m_t$ is the mass of the tube CV, $Cp_t$ is the specific heat capacity of the tubing, $T_t$ is the temperature of the tubing for that CV, $hA_{pt}$ is the heat transfer coefficient times heat transfer area between the primary side and the tubing, $hA_{ts}$ is the heat transfer coefficient times heat transfer area between the tubing and the secondary side, and $T_s$ is the temperature of the fluid on the secondary side.

$$m_t Cp_t \frac{dT_t}{dt} = hA_{pt}(T_p - T_t) + hA_{ts}(T_s - T_t) \tag{2.40}$$

*Secondary Side*

The secondary side of the OTSG is where the methodology differs from that used for the regular salt to salt heat exchangers. The changes are due to the complexity involved with two-phase flow. Water enters the OTSG as a subcooled liquid, which

has been preheated by the feedwater heater in the balance of plant, is heated to saturation in the first domain (primary CVs #5 and #6), boiled in the saturated boiling domain (primary CVs #3 and #4), and heated further in the superheated steam domain (primary CVs #1 and #2). The CVs are arranged in that order due to the OTSG being a counterflow design. This design puts the hottest primary side fluid adjacent to the hottest fluid on the secondary side for maximal heating.

The OTSG is essentially a collection of straight tubes, wherein, the three aforementioned domains (i.e., subcooled liquid, saturated boiling, and superheated vapor) are not clearly delineated in realistic operation. There is no component in the design that forces the domain to begin or end at any specific lengths. However, for our heat transfer equations, it is necessary to know the lengths and areas associated with the domains on the secondary side of the OTSG. To accomplish this, the modeling methodology allows for flexible lengths as a moving boundary between the CVs that can change dependent on the conditions in the OTSG. For example, if there is an increase in heat transfer to the secondary side, it is expected that the lengths needed to heat the water to saturation temperature and then boil it would decrease. As consequence of the length of those two domains decreasing and the overall length of the OTSG remaining constant, the length of the superheated vapor domain would thus increase. A more lengthy superheated vapor domain also allows for further heating of the steam and thus a higher outlet temperature. Conversely, if the heat flow to the secondary side of the OTSG decreases we would expect a decrease in the length of the superheated vapor domain due to an increase in the lengths of the subcooled and saturated domains. The modeling methodology used in this work accounts for these changes by making the lengths be variable.

*Subcooled Liquid Domain*

The subcooled liquid domain is comprised of two CVs. One receives the feedwater and the other outflows to the saturated boiling CV. Due to our assumptions that a CV is a well-mixed tank with homogenous conditions within, the temperature of a CV is

its outlet temperature. As such, the temperature of the subcooled CV #1, shown in Figure 2.5, is simply the saturation temperature of the fluid. That leaves subcooled CV #2 as the only temperature necessary to be solved for. The temperature of subcooled CV #2 is determined by Equation 2.41.

$$\frac{dT_{sc,2}}{dt} = \frac{h_{tsc} N \pi D_{ot}}{A_s \rho_{sc} Cp_{sc}} + \frac{2[(Cp\dot{m}T)_{fdw} - (Cp\dot{m}T)_{sc}]}{A_s \rho_{sc} Cp_{sc} L_{sc}} + \frac{\dot{P}_{sc}}{\rho_{sc} Cp_{sc}} - \frac{T_{sc}\dot{L}_{sc}}{L_{sc}} \tag{2.41}$$

In the equation, $T_{sc,2}$ is the temperature of the fluid in the CV, $h_{tsc}$ is the heat transfer coefficient between the tubing and the subcooled domain, $N$ is the number of tubes in the OTSG, $D_{ot}$ is the outer diameter of those tubes, $A_s$ is the area of flow on the secondary side, $\rho_{sc}$ is the average density of the subcooled liquid, $Cp_{sc}$ is the average specific heat capacity of the subcooled liquid, the $fdw$ subscript denotes properties belonging to the feedwater, $\dot{m}$ is the mass flow rate, $\dot{P}_{sc}$ is the rate of change of the pressure in the subcooled domain, $\dot{L}_{sc}$ is the rate of change of the length of the subcooled domain, and $L_{sc}$ is the length of the subcooled domain.

The length of the subcooled domain changes due to the heat flux through it and the pressure of the fluid. Specifically, the changes to the subcooled domain length are due to: the amount of heat flowing into it through the tubing, the heat flux due to the net flow of water between the entrance of the OTSG and the saturated boiling domain, the change in density within the subcooled domain per change in pressure, the change in pressure itself, and the change in saturated boiling temperature per change in pressure. The summation of these effects is shown in Equation 2.42, wherein, the $tsc$ subscript denotes properties relating to the tubing to subcooled domain boundary, and the $sat$ subscript denotes the saturated domain.

$$\dot{L}_{sc} = \frac{h_{tsc}A_{tsc}(T_{t,5} - T_{sat})}{A_s\rho_{sc}C_{sc}(T_{sc,2} - T_{sat})} + \frac{2\dot{m}_{fdw}T_{sc,2} - \dot{m}_{sc}T_{sat}}{A_s\rho_{sc}(T_{sc,2} - T_{sat})} + \left(\frac{L_{sc}\dot{P}_{sc}(K_{sc}C_{sc}(T_{sc} - 2T_{sat}) - 1)}{\rho_{sc}C_{sc}(T_{sc} - T_{sat})}\right) - \left(\frac{K_{sat}L_{sc}\dot{P}_{sat}}{T_{sc} - T_{sat}}\right) \tag{2.42}$$

The constant, $K_{sc}$, is the change in the fluid density per change in pressure of the subcooled domain. Similarly, the constant, $K_{sat}$ is the change in the saturation temperature per change in pressure of the saturated boiling domain. Using the assumption that the pressure losses in the three domains are constant, the pressure in each domain is thus equivalent, as shown in Equation 2.43.

$$P_{sc} = P_{sat} = P_b = P_{sh} \tag{2.43}$$

In the equation, $P_{sc}$ is the subcooled domain pressure, $P_{sat}$ is the saturation pressure of the fluid, $P_b$ is the pressure in the saturated boiling domain, and $P_{sh}$ is the pressure in the superheated vapor domain. The pressure for the secondary side of the OTSG is determined by the compressibility modified ideal gas law in the superheated vapor domain.

*Saturated Boiling Domain*

The saturated boiling domain is the length between the subcooled and superheated domains. Water flows in from the subcooled domain at its saturation temperature and is then heated further until it is fully boiled, at which the superheated domain begins. This domain is the only one with two phase flow in our consideration of the OTSG. Within the saturated boiling domain, the temperature is equal to the saturation temperature. The main variables to be determined are thus the length of the saturated boiling domain and the flow rate out of it.

The length of the subcooled boiling domain is derived from mass accountancy, as shown in Equation 2.44, wherein, $\dot{m}_{sat}$ is the flow entering from the subcooled domain, $\dot{m}_b$ is the flow exiting the saturated boiling domain, $A_s$ is the cross-sectional

flow area on the secondary side of the OTSG, $L_b$ is the length of the boiling domain, the constant $K_b$ is the change in the density of the two-phase fluid per change in pressure, $\dot{P}_{sat}$ is the rate of pressure change, and $\rho_b$ is the average density of the two-phase fluid in the domain.

$$\dot{L}_b = \frac{\dot{m}_{sat} - \dot{m}_b - A_s L_b K_b \dot{P}_{sat}}{A_s \overline{\rho_b}} \tag{2.44}$$

The saturated boiling domain is not a specific portion of the OTSG and is only conceptualized as its own control volume for the purposes of this lumped parameter model. In reality, the volume in which saturated boiling occurs in the OTSG would not be expected to neatly begin and end at specific lengths. The length of the saturated boiling domain discussed in this work is what satisfies the volume of the two-phase fluid in the OTSG given the cross-sectional area of flow. As such, the amount of saturated vapor flowing out of the boiling domain is determined by the heat flowing into the control volume and the heat necessary to fully change a unit of saturated liquid into saturated vapor, as shown in Equation 2.45.

$$\dot{m}_b = \frac{h_{tb} N \pi D L_b}{H_{fg}} \left( \frac{T_{t,3} + T_{t,4}}{2} - T_{sat} \right) \tag{2.45}$$

In the equation, $h_{tb}$ is the average heat transfer coefficient between the tubing and the saturated boiling domain, $N$ is the number of tubes, $D$ is the inner diameter of the tubes in which the fluid is flowing, $L_b$ is the length of the boiling domain, $T_{t,3}$ and $T_{t,4}$ are the temperatures of the two adjacent tubing control volumes, $T_{sat}$ is the saturation temperature, and $H_{fg}$ is the latent heat of vaporization of the fluid.

*Superheated Steam Domain*

The superheated domain has saturated vapor entering from the boiling domain, which is heated through the remaining length of the OTSG. The fluid then outflows from the OTSG as high quality dry steam for use in the turbines and other components of the balance of plant. In this model, there are two control volumes for the

superheated steam domain, which are numbered as CV#2 and CV#1. The saturated vapor flows into superheated CV#2 and the outflow of the OTSG comes from superheated CV#1. The reason for arranging them seemingly in backwards order is to mirror the numbering convention on the primary side. Due to the OTSG being a counterflow design, the primary CV#1 is adjacent to the tube CV#1, which is adjacent to the superheated CV#1. The pattern then holds true for the second set of CVs and so forth, as seen earlier in Figure 2.5. The temperature of the CV on the inlet side of the of superheated vapor domain is given by Equation 2.46, and the temperature of the CV on the outlet side is given by Equation 2.47.

$$\frac{dT_{sh,2}}{dt} = \frac{h_{tsh}N\pi DL_{sh}}{2M_{sh,2}C_{sh}}(T_{t,2} - T_{sh,2}) + \frac{\dot{m}_b}{M_{sh,2}}(T_{sat} - T_{sh,2}) + \frac{A_s L_{sh}\dot{P}_{sh}}{2M_{sh,2}C_{sh}} - \frac{\dot{P}_{sh}}{C_{sh}}\left(\frac{\delta H}{\delta P}\right)_{sh} \tag{2.46}$$

$$\frac{dT_{sh,1}}{dt} = \frac{h_{tsh}N\pi DL_{sh}}{2M_{sh,1}C_{sh}}(T_{t,1} - T_{sh,1}) + \frac{\dot{m}_{sh,1}}{M_{sh,1}}(T_{sh,2} - T_{sh,1}) + \frac{A_s L_{sh}\dot{P}_{sh}}{2M_{sh,1}C_{sh}} - \frac{\dot{P}_{sh}}{C_{sh}}\left(\frac{\delta H}{\delta P}\right)_{sh} \tag{2.47}$$

For the previous two domains (i.e., subcooled liquid and saturated boiling), the lengths are determined as the necessary amount to fully prepare the fluid for the next domain, given the heat transfer rate along that length. The total length of the OTSG is constant. Therefore, the length of the final domain, for superheated vapor, is determined via simple arithmetic shown in Equation 2.48. Likewise, the rate of change in the length of the superheated domain is determined by the derivative of the other two lengths, given in Equation 2.49.

$$L_{sh} = L_{total} - L_b - L_{sc} \tag{2.48}$$

$$\dot{L}_{sh} = -\dot{L}_b - \dot{L}_{sc} \tag{2.49}$$

The superheated steam pressure is determined by the derivative of the compressibility adjusted ideal gas law, as shown in Equation 2.50. [73, p.185] In the equation,

$\dot{P}_{sh}$ is the change in steam pressure per second, $Z_s$ is the compressibility factor of the steam, $A_s$ is the cross-sectional area of flow, $L_{sh}$ is the length of the superheated vapor domain, $M_{stm}$ is the molar mass of steam, and $M_s$ is the mass of steam in the domain. The temperature of CV#2 is used because, due to our assumptions, it is the average steam temperature within the superheated steam domain.

$$\dot{P}_{sh} = \frac{Z_s R}{A_s L_s M_{stm}} \left( \dot{M}_s T_{s,2} + M_s \dot{T}_{s,2} \right) - \frac{P_s \dot{L}_s}{L_{sh}} \tag{2.50}$$

**Regenerative Rankine Cycle**

In previous MSR dynamic modeling work, the system ended at the OTSG due to the assumption that controls further down the balance of plant would be able to provide feedwater at constant pressure and temperature. [11] This assumption has not been made in this work. Furthermore, in the interest of having a complete IES model that tracks heat flow from its production to its utilization and waste removal via condenser to the atmosphere, the remainder of a Rankine cycle balance of plant has been included in the model.

The electricity generation system used in this work is comprised of the OTSG and a regenerative Rankine cycle Balance of Plant (RBOP). The RBOP is intended to be a conventional design that is generic enough to be representative of many plants. The components that comprise the system are high and low pressure turbines, a moisture separator, reheater, condenser, and a reheater for the OTSG feedwater. The RBOP has high, intermediate, and low pressure fluid flow lines situated around high pressure and low pressure turbines. The arrangement of the components is shown in Figure 2.6.

Heat regeneration is accomplished in the design in two ways. First, by reheating the outflow from the high pressure turbine (HPT) and using it to drive the low pressure turbine (LPT). Secondly, flow is bled off of the two turbines and combined with the remaining flow lines: the saturated liquid from the moisture separator, the primary side outlet from the reheater, and the outlet from the condenser.

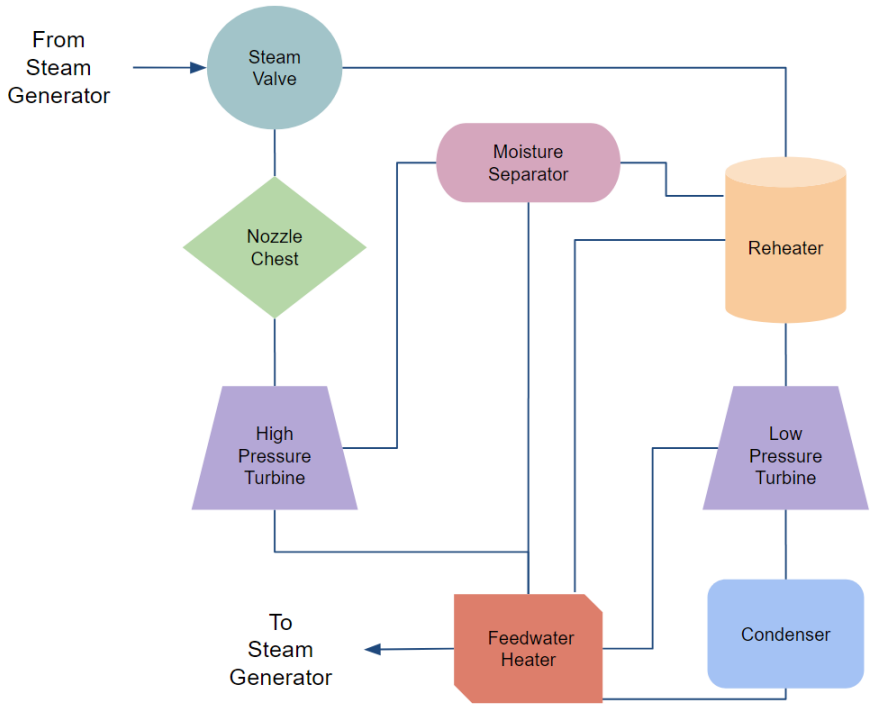


Figure 2.6: Arrangement of the components comprising the balance of plant (excluding the steam generator) in the regenerative Rankine cycle electrical production system in the IES model.

To aid in determining the properties of the fluid throughout the RBOP loop, media data libraries in OpenModelica were used. The two media libraries used are StandardWater and MoistAir. [75, 76] The StandardWater library uses the IF97 steam/water properties table. [77] The OpenModelica MoistAir library was developed as part of the Clean Sky JTI project titled "Modelica Model Library Development for Media, Magnetic Systems and Wavelets". [78] StandardWater was used in this model to determine three properties throughout the model. These properties are: (1) specific enthalpy as a function of pressure and temperature; (2) isentropic enthalpy change in the turbines as a function of the inlet enthalpy, inlet pressure, and outlet pressure; and (3) temperature as a function of pressure and enthalpy. MoistAir was used to determine the saturation temperature and enthalpy of vaporization in the moisture separator and condenser.

The steam valve is the first component in the overall RBOP loop. Hot high quality steam flows in from the OTSG and into the steam valve. The steam valve separates the flow into two lines: the main flow line directed towards the HPT and the regeneration line through the reheater. In this model, the flow rate for the regeneration line is 20% of the flow into the steam valve. The other 80% of the flow is directed toward the HPT.

Before entering the HPT, some of the flow is bled off toward the feedwater heater. The high pressure bleed has higher enthalpy than the other flow lines into the feedwater heater, which helps the outlet meet its pressure and temperature goals. In this work, the bleed rate for the HPT is 2% of the flow through the nozzle chest.

The main steam line goes through the high pressure turbine. Due to the superheating of the steam in the OTSG, the inlet of the HPT is high quality dry steam. Work is performed by the steam as it experiences isentropic expansion through the turbine. The change in specific enthalpy is determined as a function of its inlet enthalpy, inlet pressure, and outlet pressure. The energy extracted by the turbine is determined by the specific enthalpy change and the mass flow rate through the turbine, shown in Equation 2.51.

$$Q = \dot{m} \cdot \Delta H \tag{2.51}$$

Now at a lower pressure and temperature, the outlet of the HPT is expected to be at lower steam quality. The quality of the steam is determined as a function of its current enthalpy, as shown in Equation 2.52. In the equation, $X$ is the steam quality, $H_{HPT}$ is the enthalpy of the HPT outlet fluid, $H_f$ is the enthalpy of saturated liquid at that pressure, and $H_{vap}$ is the enthalpy of vaporization at that pressure. A steam quality of $X > 1$ is dry high quality steam, between $0 < X < 1$ is saturated steam, and below zero is liquid.

$$X = \frac{H_{HPT} - H_f}{H_{vap}} \tag{2.52}$$

If the outlet flow from the HPT is still dry high quality steam, then the flow passes through the moisture separator and goes to be reheated. If the outlet flow is saturated, then the moisture separator dries the steam by removing the liquid droplets. The outlet of the moisture separator is thus dry steam to be reheated, and saturated liquid headed towards the feedwater heater. The saturated liquid is at a higher enthalpy than the outlet of the feedwater heater and thus aids in the energy regeneration. If the steam quality is between $0 < X < 1$, then the outlet flow rate from the moisture separator to the reheater is given by Equation 2.53, wherein, $\dot{m}_{MS}$ is the flow rate from the moisture separator to the reheater, and $\dot{m}_{HPT}$ is the flow rate from the HPT to the moisture separator.

$$\dot{m}_{MS} = X \cdot \dot{m}_{HPT} \tag{2.53}$$

The reheater is a counterflow heat exchanger which receives hot, high pressure steam that had been diverted from the steam valve and uses it to superheat the intermediate pressure working steam from the moisture separator. As a heat exchanger, the reheater cannot easily be modeled in the same manner as the other

heat exchangers throughout the IES model. The reason is that the steam properties are not constant when temperature changes near the saturation temperature, and especially across the phase change. For an example, let us use the primary side of the reheater, where the flow from the steam valve is. There the pressure is high enough such that, as it transfers heat to the secondary side, it could change phase and be liquid while still maintaining a high enough temperature to heat the intermediate pressure steam on the secondary side. The potential for two-phase flow on the primary side of the reheater greatly complicates the modeling of the component. In the OTSG, the two-phase flow is expected to be present. However, in the reheater, the flow may or may not be two-phase, given the pressure and temperature on both sides of the heat exchanger.

The relevance of the reheater as a component in the IES model is the outlet properties of the high pressure and intermediate pressure sides. Specifically, the flow on the intermediate pressure side is heated by receiving energy from the flow on the high pressure side. The inlets on both sides are known, but the outlets are not. The energy transfer is due to Newton's law of cooling, which means the thermodynamic driving force is the temperature difference between the two sides. As a counterflow heat exchanger, it can thus be reasoned that either the hot side flow can be cooled to the temperature of the cold side inlet, or that the cold side flow be heated to the temperature of the hot side inlet. These two possibilities constitute the limits of an effective reheater design. A reheater with infinite heat transfer area would have the outlet and inlet on one half reach nearly the same temperature. With a finite heat transfer area, the minimum temperature difference would be a known quality based on the area and heat transfer coefficient.

A novel method for the reheater was developed in this work which provides realistic results while being lightweight enough to keep the model running rapidly. The outlet temperatures are calculated in a multi-step process. First, the maximum energy the hot side can give and the cold side can give are determined and compared. The lower number is the heat transfer limit for the reheater. It is assumed that an effective

reheater design will reach that realistic limit. With the energy transfer from one side to the other known, the specific enthalpies of the two outlet flows can be calculated with simple arithmetic. In this way, the outlet temperature of both sides can be determined while remaining design agnostic and generically representative.

Now that the steam has been reheated, it is directed into the low-pressure turbine (LPT). It enters at intermediate pressure and exits at low pressure before flowing to the condenser. The method for determining the work performed by the LPT is the same as for the HPT. The LPT also has a portion of its inlet flow bled off to be used in the feedwater heater. In the current version of the model, the LPT bleed rate is set to change in order to keep the outlet flow of the feedwater heater constant.

The condenser receives the outlet flow from the LPT and cools it back into liquid. The specific design of the condenser is not necessary in this model, but the inspiration is a conventional cooling tower. In the condenser, the hot inlet flow is sprayed into a chamber that is cooled by a large flow of atmospheric pressure cooling water. The fluid in the chamber cools, condenses, and flows out at near saturation temperature. The outlet flow then heads to the feedwater heater to be heated and returned back to high pressure.

The feedwater heater is a open-channel design in which all the inlet flows are combined into a single outlet flow. There are five inlet flows: the HPT bleed, liquid removed via the moisture separator, the reheater outflow from the steam valve side, the LPT bleed, and the condenser outflow. The HPT bleed and reheater flows are at high pressure. The moisture separator and LPT bleed flows are at intermediate pressure. The condenser flow is at low pressure. The enthalpy and outlet flow rate from the feedwater heater is determined by Equation 2.54. In the equation, $fdw$ denotes feedwater, $HPB$ denotes high pressure bleed, $MS$ denotes moisture separator, $vRH$ denotes valve-side reheater, $LPB$ denotes low pressure bleed, and $con$ denotes condenser.

$$(H\dot{m})_{fdw} = (H\dot{m})_{HPB} + (H\dot{m})_{MS} + (H\dot{m})_{vRH} + (H\dot{m})_{LPB} + (H\dot{m})_{con} \tag{2.54}$$

## 2.4 Example Scenarios

Multiple types of accidents are simulated in this work. The primary scenarios are a reactivity initiated accident (RIA) in the core, a loss of flow accident (LOFA) in the primary loop, a loss of heat sink accident (LOHSA) in the electricity production system, and a LOHSA in the hydrogen production system. The methodology for each accident scenario is described further in this section.

*Reactivity Initiated Accident*

The RIA scenario simulated in this work is a total reactivity insertion of 600 pcm across 54.55 seconds. The reactivity is inserted at a constant ramp rate of 11 pcm per second. The basis for this scenario is design documentation for the EBR-II reactor, which was a sodium-cooled fast reactor (SFR) designed in the late 1950s. [79] Specifically, the primary concern for RIA scenarios was a control rod withdrawal. For the EBR-II system, the maximum control rod drive speed was mechanically limited to five inches per minute. At that drive speed, the maximum reactivity addition rate was 11 pcm per second up to a maximum of 600 pcm. Control rod withdrawal is the basis for the RIA scenario due to the low pressure in the system precluding control rod ejection, which is a concern in conventional LWR designs. For that reason, the EBR-II design is a more comparable example for the MCFR in this work than a LWR would be. For comparison, the estimated reactivity insertion for a rod ejection accident in an average PWR at hot full power is a maximum of 290 pcm in as little as 400 seconds. [80, page 35] In an average BWR at hot full power, the estimated reactivity insertion is a maximum of 1300 pcm in as little as 45 seconds. The RIA

scenario chosen in this work is therefore between the PWR and BWR rod ejection estimates. [81, 82]

*Loss of Flow Accident in Primary Loop*

The LOFA scenario simulated in this work is a pump trip in the primary loop of the system. For the MCFR, the primary loop is the flow through the core and the eight heat exchangers in parallel which together comprise the primary heat exchanger in this model. After a pump trip, the flow rate decreases as an exponential decay curve due to the momentum in the system. The exact flow rate decrease rate would be dependent on the design of the piping and the fluid involved. Our model strives to be design agnostic as a generic fast-spectrum MSR. As such, a decay constant of $0.092\,\mathrm{sec}^{-1}$ was used as a realistic estimate based on pump coastdown research from the Argonne national laboratory. [83, 84] The minimum flow rate reached after the pump trip in this LOFA scenario is set to 12.5% that of the nominal flow rate. This minimum flow rate is a conservative approximation of a partial loss of flow in which seven of the eight primary loop pumps in the MCFR fail and no natural circulation occurs. The amount of natural circulation that could be expected in a system is design dependent and non-trivial to determine. As such, the minimum flow rate in this scenario was determined via engineering judgment with a basis from the design of the MCFR. In this model, the eight PHXs of the MCFR are represented by a single combined PHX, as shown in Figure 2.2. Therefore, the failure of seven pumps is represented by a reduction in flow rate down to 12.5%. The resulting primary loop flow fraction as a function of time after pump trip is given in Figure 2.7.

*Loss of Heat Sink Accident*

The heat produced by the reactor flows through the primary and secondary heat exchangers before going to the separate electricity and hydrogen production systems. From the perspective of the heat production system, the electricity and hydrogen systems are the heat sinks. A flow failure in either system is therefore representative

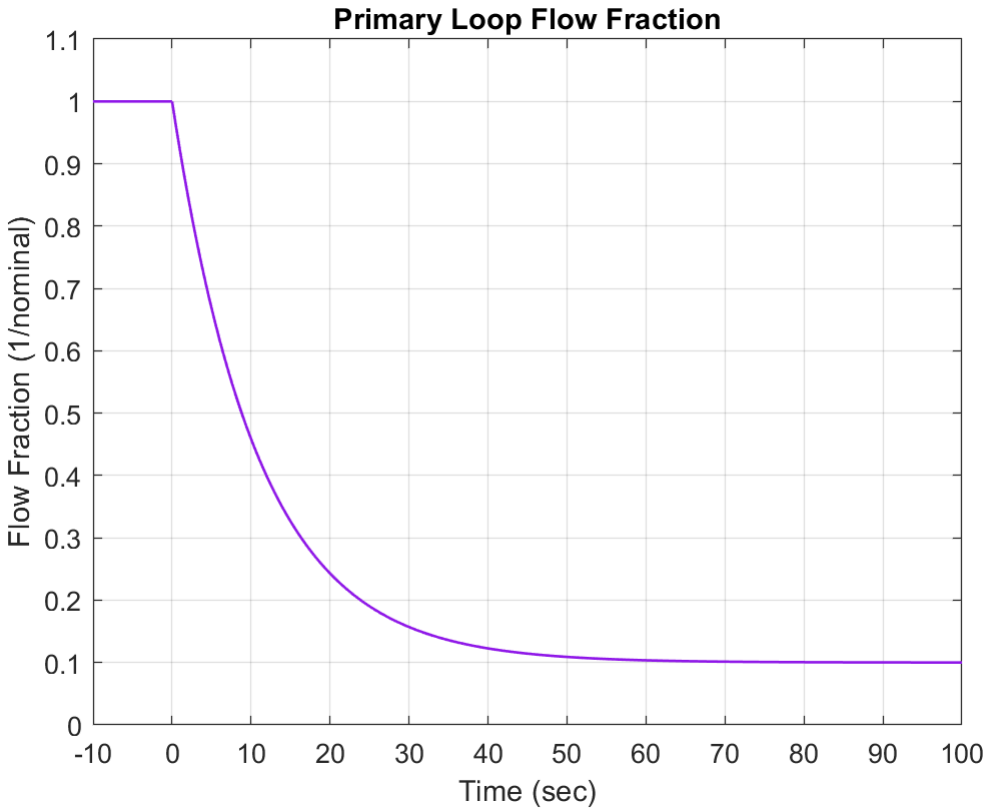


Figure 2.7: Primary loop flow rate in response to a pump trip. The flow rate is expressed as a fraction of the nominal flow rate.

of a potential loss of direct access to the ultimate heat sink. [85] A Loss of Heat Sink Accident (LOHSA) scenario in this paper is one which has either of those two systems unable to receive as much heat than at nominal. In this work, two LOHSA scenarios were tested: a failure in the electrical production system and a failure in the hydrogen production system. For the purpose of comparison between the two different systems, the scenario is a ramp decrease of the flow rate into the heat exchanger receiving heat from the SHX via the tertiary loop. For the electrical production system, the OTSG feedwater flow rate is decreased. For the hydrogen production system, the sulfuric acid and water feed into the decomposer is decreased. For both, the ramp rate is a decrease of 0.0016% of nominal flow rate per second across 500 seconds down to a minimum of 20% nominal flow rate. The minimum flow rate is held for 1000 seconds and then raised back to nominal at the change rate as before.

## 2.5 Results

The results for the four scenarios simulated in this work are included in this section. These scenarios are for a RIA in the core, a LOFA in the primary loop, a LOHSA in the electrical production system, and a LOHSA in the hydrogen production system. The RIA scenario is intended to be representative of a control rod withdrawal from the MCFR core. The LOFA scenario is intended to be a main pump trip in the primary loop of the IES. The two LOHSA scenarios are a simplistic feed flow rate failure intended to provide comparison between the two heat sinks.

### 2.5.1 Reactivity Initiated Accident

In the control rod withdrawal scenario, the reactivity insertion begins at the zero second mark. The results of the power response are shown in Figure 2.8. In the figure, the fission power increases rapidly within the first minute and brings the total reactor power to peak at approximately 5.2 times nominal power. The difference in thermal

power production and usage logically leads to accumulation in the heat transfer fluids. As such, the salt temperature in each loop increases, as shown in Figure 2.9. The temperature difference across each loop remains mostly constant, with changes due primarily to transport delays. With similar temperature differences and constant flow rates, the heat transfer of each component likewise remains mostly constant. The increase in fuel temperature then leads to a negative reactivity insertion due to the negative fuel temperature coefficient. This negative insertion thus increases in response to the positive external reactivity insertion due to the control rod withdrawal, as shown in Figure 2.10. The reactivity coefficient due to the temperature of the reflector is positive, but the effect is much smaller than from the fuel. Specifically, the reactivity feedback coefficient from temperature in the fuel is -4.4378$\times 10^{-5}$, and in the reflector it is 0.1164$\times 10^{-5}$. Thus, the total reactivity coefficient of the reactor from temperature is still negative due to the magnitude of the fuel feedback being thirty-eight times larger for the same temperature change.

The results from this transient show the potential inherent safety of the reactor system that we expect to see. Without any operator action, the power pulse ends by dropping down to a new steady state level. The concern then goes from a high peak power to a continued high temperature stressing the loops within the system. The results show a sustained increase of approximately 150°C in each of the loops at the new steady state compared to the pre-transient nominal level. However, it is important to reiterate that these results are with no operator or system action. The behavior demonstrated in these results is purely the inherent behavior of the system. In a realistic accident scenario following a control rod withdrawal, like in this transient, the reactor would quickly be shutdown. In the IES model, shutdown would be performed by an external insertion of a negative reactivity. As for a physical MCFR-C, Terrapower has yet to release public information on their planned control surfaces.

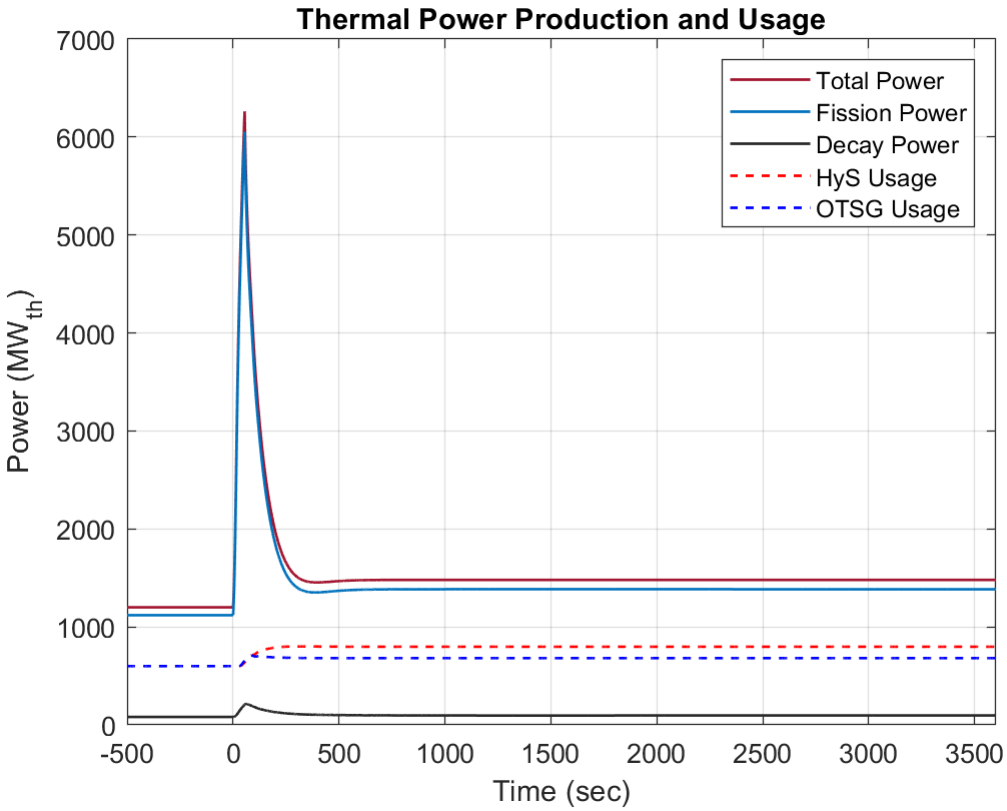


Figure 2.8: The power production and usage in response to the control rod withdrawal scenario. Solid lines are indicative of power production and dashed lines are power usage.

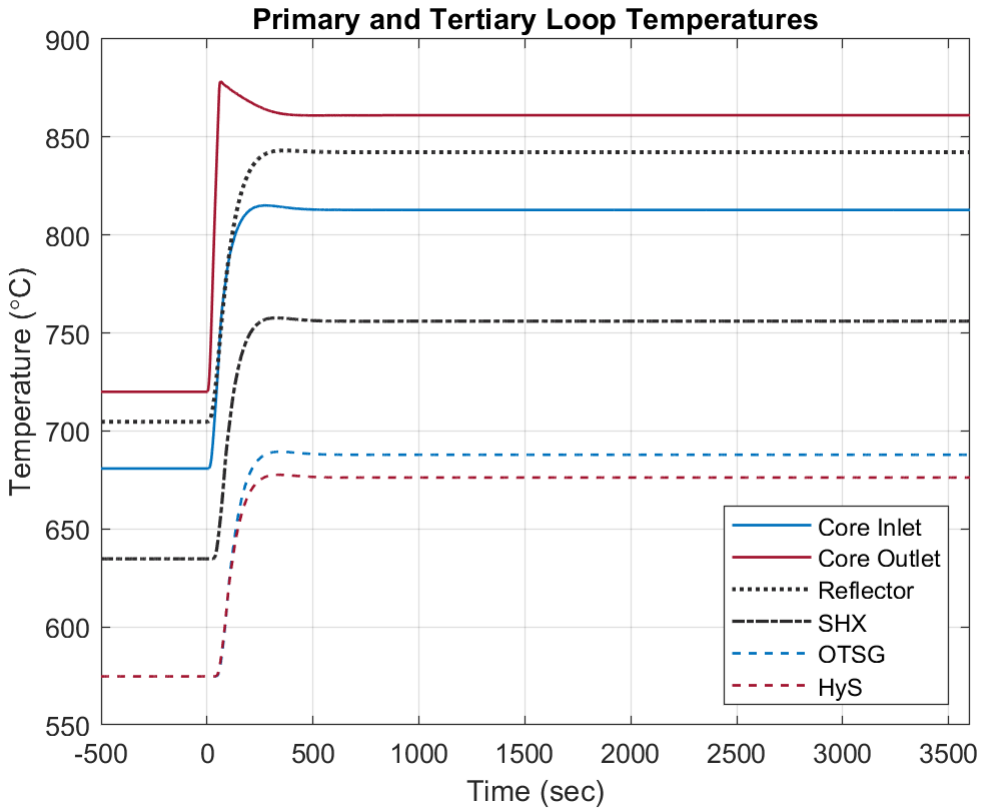


Figure 2.9: The primary and tertiary loop temperatures in response to the control rod withdrawal scenario. The core inlet, core outlet, and reflector temperatures are in the primary loop. The SHX secondary side outlet, OTSG primary side outlet, and HyS decomposer primary side outlet temperatures are in the tertiary loop.

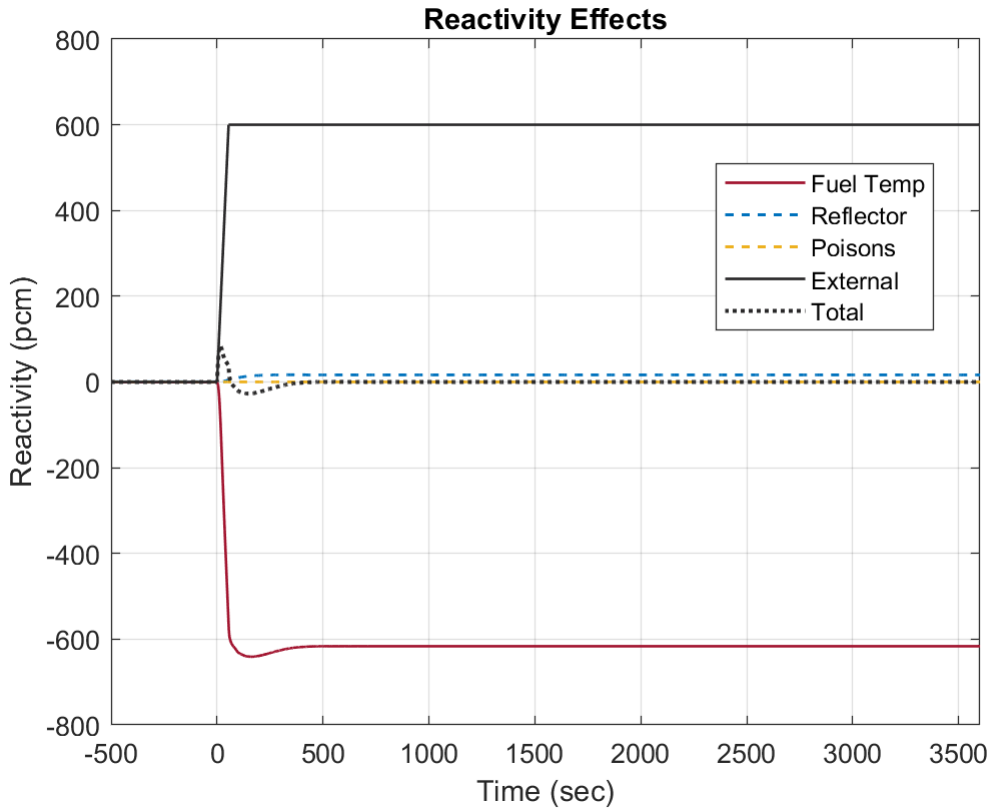


Figure 2.10: The reactivity feedbacks in response to the control rod withdrawal scenario. The external reactivity insertion is directly caused by the withdrawal.

### 2.5.2 Loss of Flow Accident in Primary Loop

In the LOFA scenario, the primary loop pump is tripped at the zero second mark. After which, the flow rate in that loop decreases according to the exponential decay curve shown in Figure 2.7. The resulting effect on the power production and usage in the IES is shown in Figure 2.11. In the figure, the power production is shown in solid lines as fission power, decay power, and the total thermal power generated by the two. Likewise, the thermal power usage of the HyS decomposer and OTSG in the RBOP are shown as dashed lines.

As the flow rate in the primary loop decreases, the ability for the core to heat an individual unit of fuel salt increases and, likewise, the primary heat exchanger's ability to cool a unit of fuel salt increases. The core outlet temperature increases and the PHX primary side outlet temperature decreases. Therefore, the combined effect is that the temperature difference across the loop increases, as shown in Figure 2.12. As the system reaches a new steady state, the temperatures in each of the loops likewise settles. The temperature gradient of the primary loop broadens such that the core outlet is over 40 °C higher than nominal, whereas the core inlet temperature decreased by approximately 140 °C. In the secondary and tertiary loops, the temperature of the salt likewise decreases. The minimum temperature reached by the secondary salt is 488 °C, which is approximately 103 °C more than its melting point. The minimum temperature reached by the tertiary salt is lower at 425 °C, which is 283 °C higher than its melting point. The salt that came closest to its melting point is the fuel salt, which reached approximately 10 °C of its melting point at its minimum. The topic of salt freezing is complex and local differences from the cold leg average temperature are dependent on the specific design and its piping arrangement. Specifically, the local temperature within the pipe may differ radially due to the specifics of the flow regime.

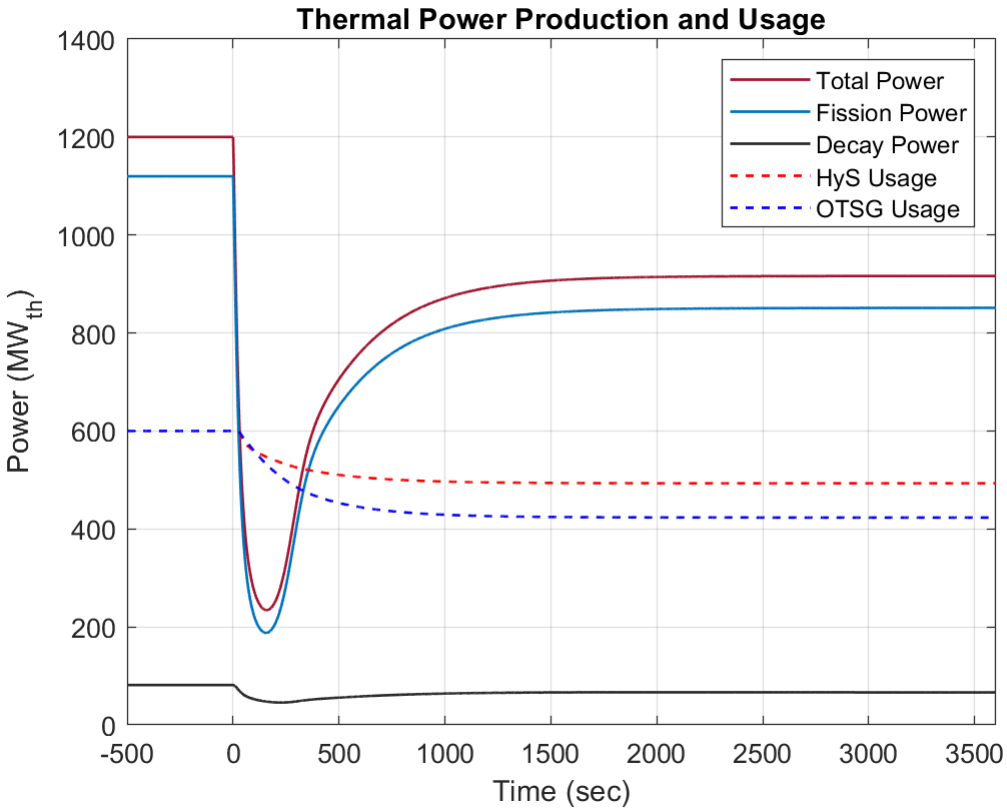


Figure 2.11: The power production and usage in response to the primary loop pump being tripped. Solid lines are indicative of power production and dashed lines are power usage.

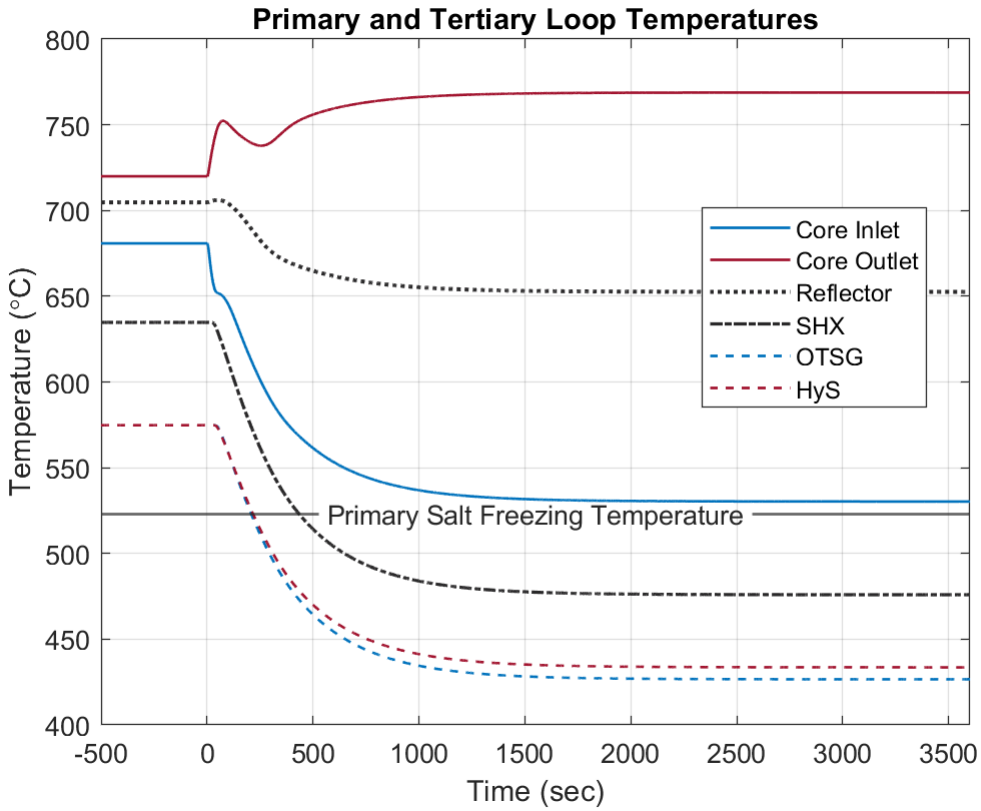


Figure 2.12: The primary and tertiary loop temperatures in response to the primary loop pump being tripped. The core inlet, core outlet, and reflector temperatures are in the primary loop which has a melting point of approximately 523 C. The secondary salt melting point is 385 C. The SHX secondary side outlet, OTSG primary side outlet, and HyS decomposer primary side outlet temperatures are in the tertiary loop. The tertiary salt has a melting point of 142 C.

As for the primary loop, there are a few unique factors there to reduce any potential minimum temperature differences in local areas. These factors include the high flow rate compared to the other loops, the short loop length, and the presence of decay heat in the fuel salt. Though this IES model does not have a specific piping arrangement, the MCFR's design has a relatively short primary loop which is entirely within the vessel. The IES dynamic model presented in this work does not have the capability to represent salt freezing. In regards to the design of this IES, it was found that special consideration must be made as to the identity of the salt in the secondary loop to preclude the possibility of freezing in scenarios such as this one. Given the three-loop arrangement of the IES salt loops and the temperature gradients expected in both accident scenarios and potential load following, the secondary salt was required to have both a low melting point and a wide operating temperature range.

The reactivity effects throughout the transient are shown in Figure 2.13. In the figure, the dominant reactivity effect is from fuel temperature feedback. The temperature in each of the loops reaches a new steady state which is lower than their nominal temperature. At this lower steady state temperature, the fuel temperature feedback and reflector temperature feedback balance each other out.

Overall, the average core temperature increases in the first hundred seconds, which causes a negative reactivity insertion that subsequently decreases reactor power. The negative reactivity continues to decrease reactor power until the fuel temperature begins to decrease, which causes a switch to be a positive reactivity insertion. After which, the system stabilizes at a new steady state fuel salt temperature of approximately 652.6 °C and a total reactor power of approximately 76.4% after having reached a brief minimum of 19.6%. The major concern with sustained low power while maintaining the same fluid flow rates in the other loops is that the mismatch in power generation and cooling may lead to salt freezing in some of the loops. With this IES design, the secondary and tertiary loops are not close to freezing.

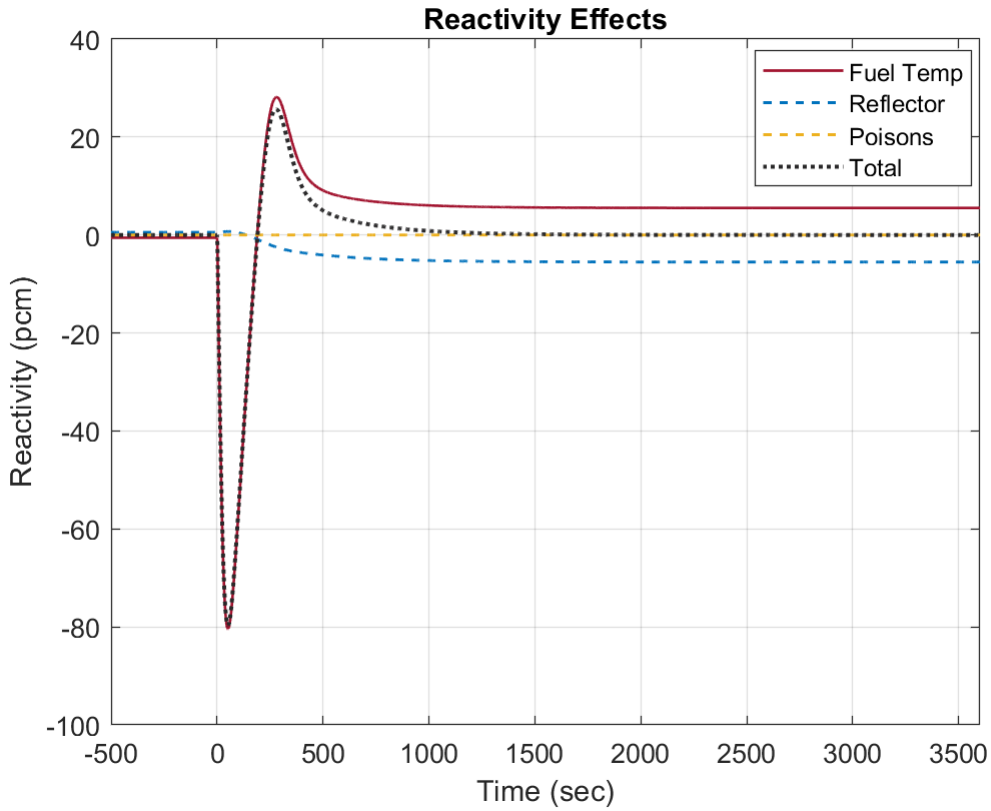


Figure 2.13: The reactivity feedbacks in response to loss of flow in the primary loop of the IES.

The secondary salt in this design was specifically chosen because of its operating temperature range and low melting point. This decision allows for greater flexibility and safety for the overall IES. As such, consideration of the salts chosen for a design will affect the ability of the IES to handle both accident scenarios and load following conditions.

### 2.5.3 Loss of Heat Sink Accidents

In the LOHSA scenarios, the feed flow rate into one of the two energy conversion systems (i.e., Rankine cycle and Hybrid Sulfur cycle) is linearly decreased down to 20% of nominal, held there, and then linearly increased back to nominal. The overall behavior of the system is similar across both versions of the LOHSA scenario. The general expected behavior is that when the power usage is below nominal the temperatures in the loops will increase and cause the fission power to decrease until a new steady state is reached. Also, due to the IES tertiary loop connecting the three systems, as the average tertiary salt temperature increases, the power usage on the system being held at nominal conditions will increase. This effect is due to the system being able to accept more power when there is an increased temperature on the hot side of its main heat exchanger. In the case of the OTSG, hotter tertiary salt allows for quicker boiling and thus more length for further superheating of the steam. For the HyS system, the decomposer is similarly able to boil its feed and provide energy for the decomposition reactions, which leads to a higher conversion rate.

*OTSG Feedwater Flow Failure*

The power production and usage, temperature, and reactivity results for the OTSG side LOHSA scenario are shown respectively in Figures 2.14, 2.15, and 2.16. In these results, we see the general expected behavior of an increase in temperatures across the loops and a decrease in power production. The thermal power production curves below the new steady state at approximately 600 seconds and above the new steady state at 2100 seconds, which indicates that the system is slightly underdamped.

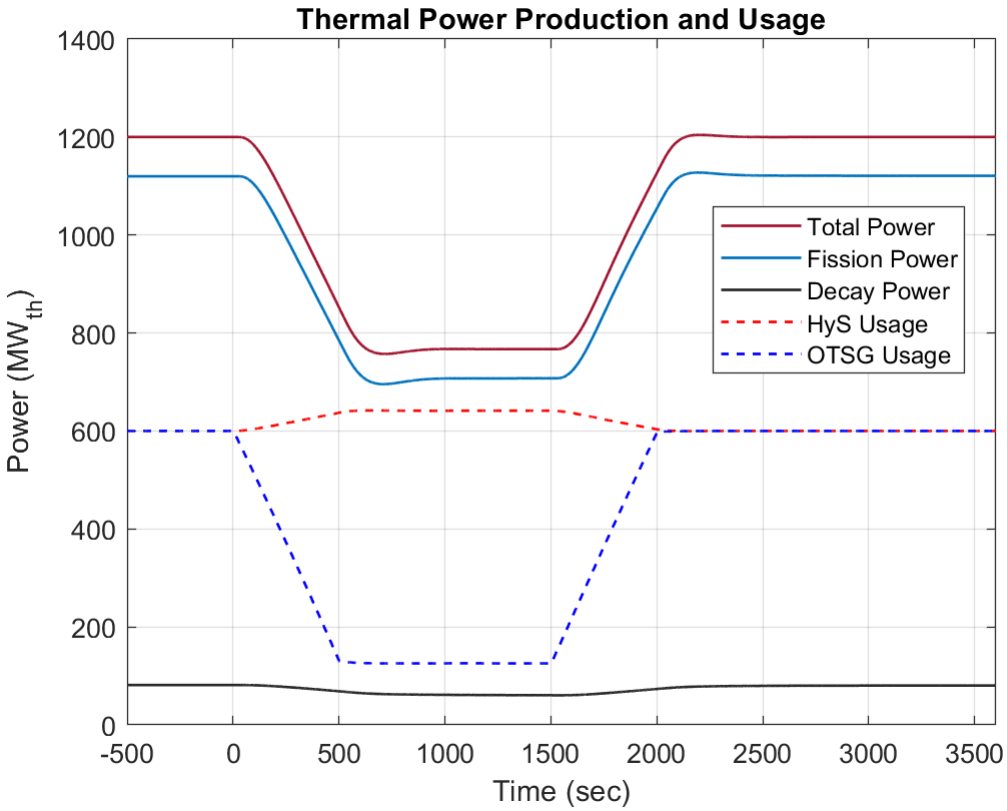


Figure 2.14: Thermal power production and usage in response to the decrease in OTSG feedwater flow rate. Solid lines are indicative of power production and dashed lines are power usage.

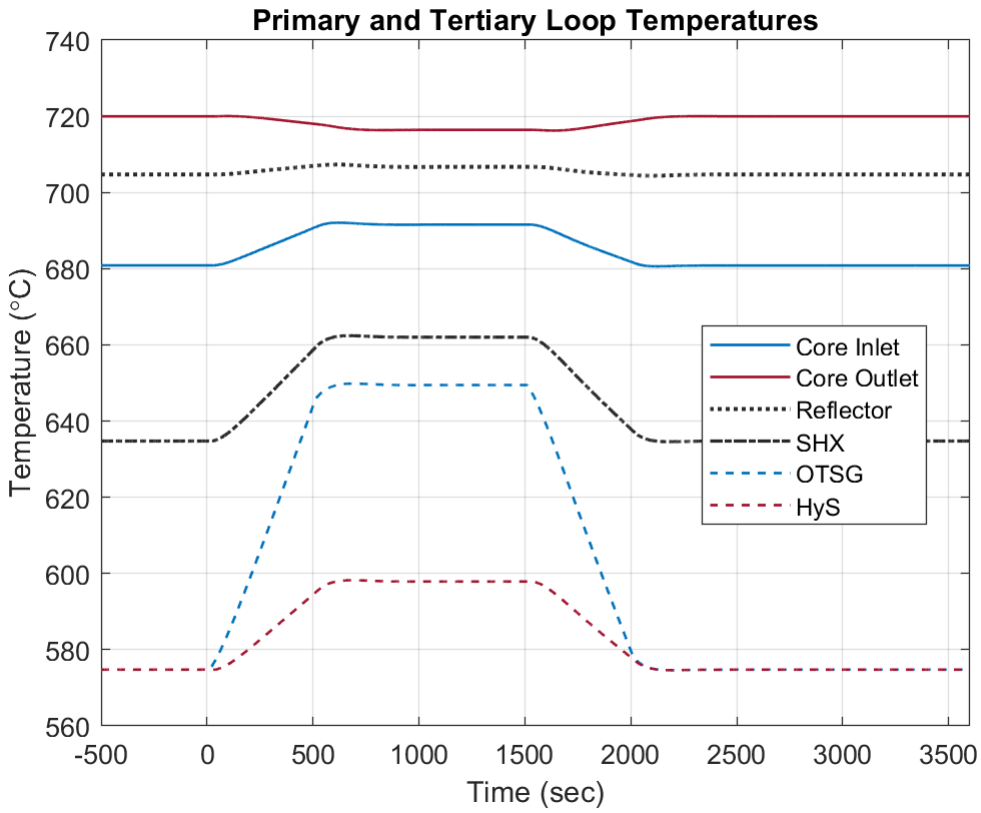


Figure 2.15: Primary and tertiary loop temperatures in response to the decrease in OTSG feedwater flow rate. The core inlet, core outlet, and reflector temperatures are in the primary loop. The SHX secondary side outlet, OTSG primary side outlet, and HyS decomposer primary side outlet temperatures are in the tertiary loop.

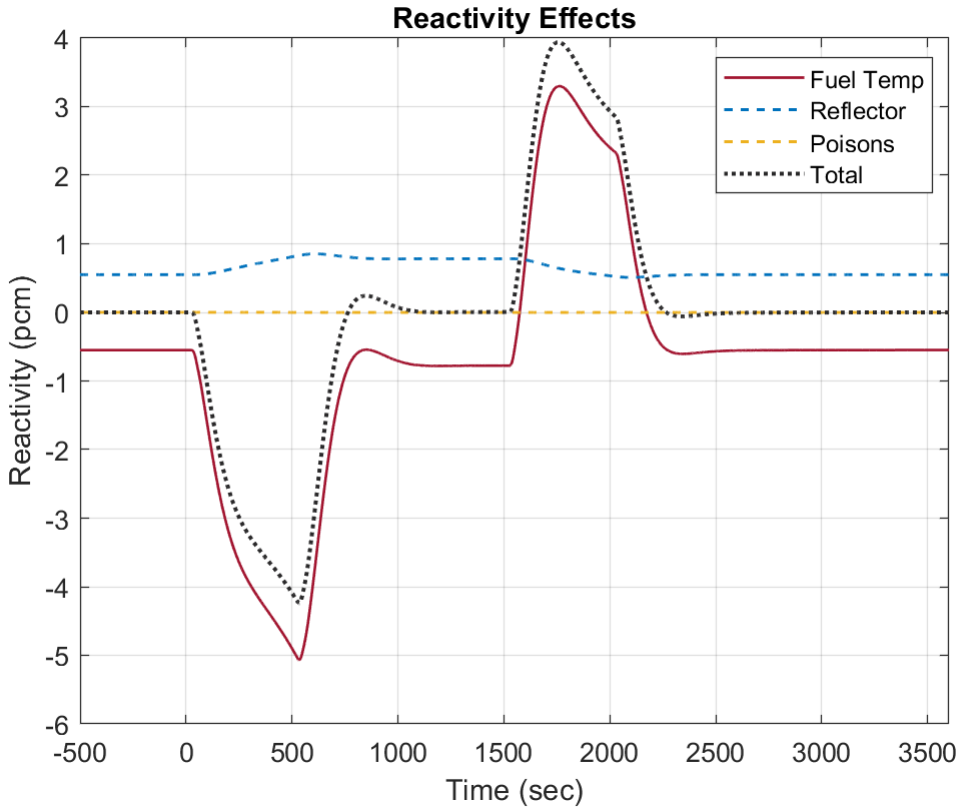


Figure 2.16: Reactivity feedbacks in response to the decrease in OTSG feedwater flow rate for the RBOP LOHSA scenario. Fuel temperature feedback is shown in solid red. Reflector temperature feedback is shown in dashed blue. Reactivity effect from Xenon and Samarium fission product poisons are shown in dashed yellow. The total net feedback response is shown in dotted black.

The average fuel salt temperature increases in the primary loop as less power is removed from the system, shown in Figure 2.15. As the power production from fission subsequently decreases, the core outlet temperature similarly declines. Overall, the temperature difference across the primary loop decreases, which due to the constant flow rate, is expected as less heat transfer through the system. In the tertiary loop, the temperature at the outlets of all three components (SHX, OTSG, and HyS decomposer) increases. The tertiary loop outlet temperature of the OTSG sees the highest increase, as expected due to the lower feedwater flow rate through it. As the OTSG removes less heat from the system, the outlet salt temperature would increase to near that of the SHX outlet. A OTSG outlet temperature nearly equivalent to the SHX would represent no power removed by the OTSG.

The fuel temperature feedback dominates the total reactivity response throughout the scenario, shown in Figure 2.16. The reflector does not comparably have much of a reactivity effect due to its temperature only increasing slightly and the fact that its reactivity coefficient is much smaller than that of the fuel. The reactivity effect from the poisons is magnitudes less due to the hardened high-energy spectrum of the neutrons in the fast reactor making the poisons have small absorption cross sections. The overall reactivity effect throughout the scenario is small, at only a few pcm. At this smaller scale, it can clearly be seen that the fuel and reflector temperature feedbacks are non-zero and countering each other. The reason for this effect is that the steady state core temperatures are slightly different than what the model has for what the nominal conditions should be. These temperatures differ slightly due to the initialization of the model at the start of a simulation.

*Hybrid Sulfur Cycle Decomposer Feed Flow Failure*

The LOHSA results for the HyS side of the tertiary loop strongly resemble the LOHSA results for the OTSG side. This similarity is expected due to both sides nominally using the same thermal power and the flow rate decrease from the LOHSA being the same in both scenarios with the only difference being the location. In

both scenarios, as the feed flow rate is decreased, the power usage of that system proportionally decreases. The power production and usage across the HyS LOHSA scenario is shown in Figure 2.17.

The decrease in heat removal by the HyS decomposer leads to a increase in the tertiary loop temperature. The increase in the tertiary loop temperature causes a subsequent increase in the temperature of the other loops, which leads to a decrease in reactor power due to the fuel temperature feedback coefficient. The result is a new steady state with lower power production at higher temperatures. The temperatures in the primary loop and tertiary loops are shown in Figure 2.18.

The reactivity feedbacks across the transient are shown in Figure 2.19. As expected, the feedback due to fuel temperature is the dominant effect. The maximum reactivity change is only within several pcm and peaks when the feed flow rate stops being changed. The fuel temperature and reflector feedbacks are not exactly zero before the transient begins. This phenomenon is due to the steady state temperature conditions reached before the scenario are slightly different than the values stated in the model. Essentially, the core is slightly hotter (by 0.3 Kelvin) at the pre-transient nominal conditions it settles at than the initial conditions that are set in the model. This level of specificity helps demonstrate how small the amount of reactivity being discussed is in the wider context of the IES.

Overall, the results for the OTSG and HyS LOHSA transients are mostly identical; which is expected. The major difference is with the temperature reached in the tertiary loop between 500 and 1500 seconds. The reason for this difference is due to the thermal power use of the other system. In both scenarios, the power use of the other system increases slightly as the tertiary loop temperature increases.

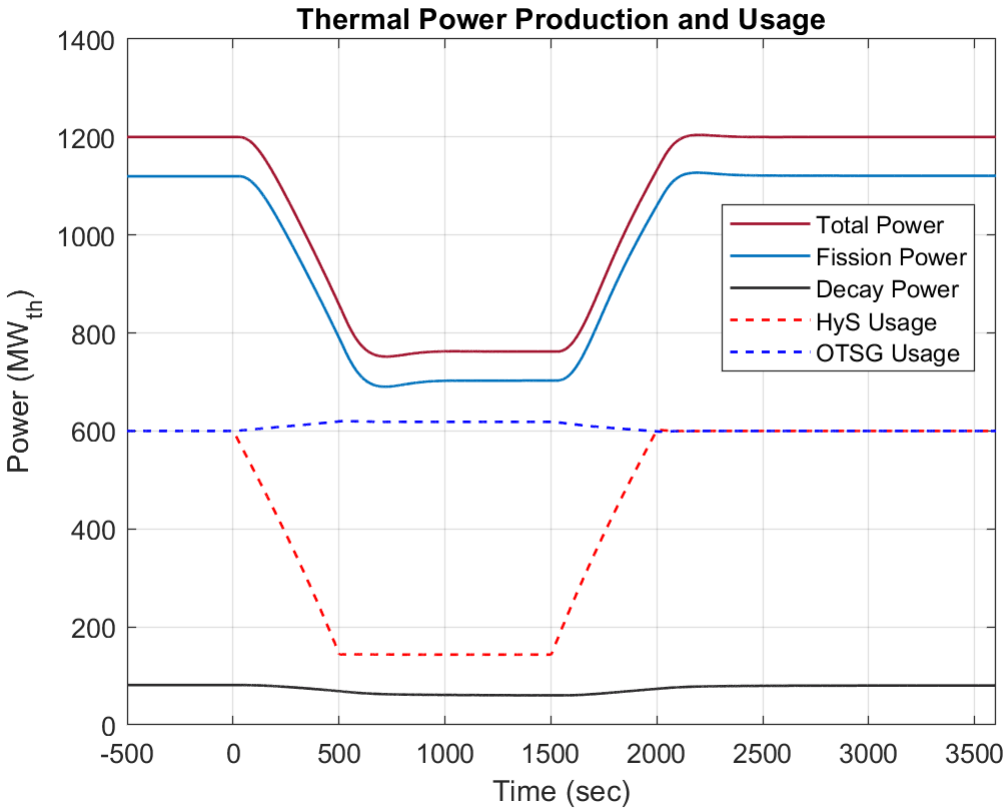


Figure 2.17: Thermal power production and usage in response to the decrease in HyS decomposer feed flow rate. Solid lines are indicative of power production and dashed lines are power usage.

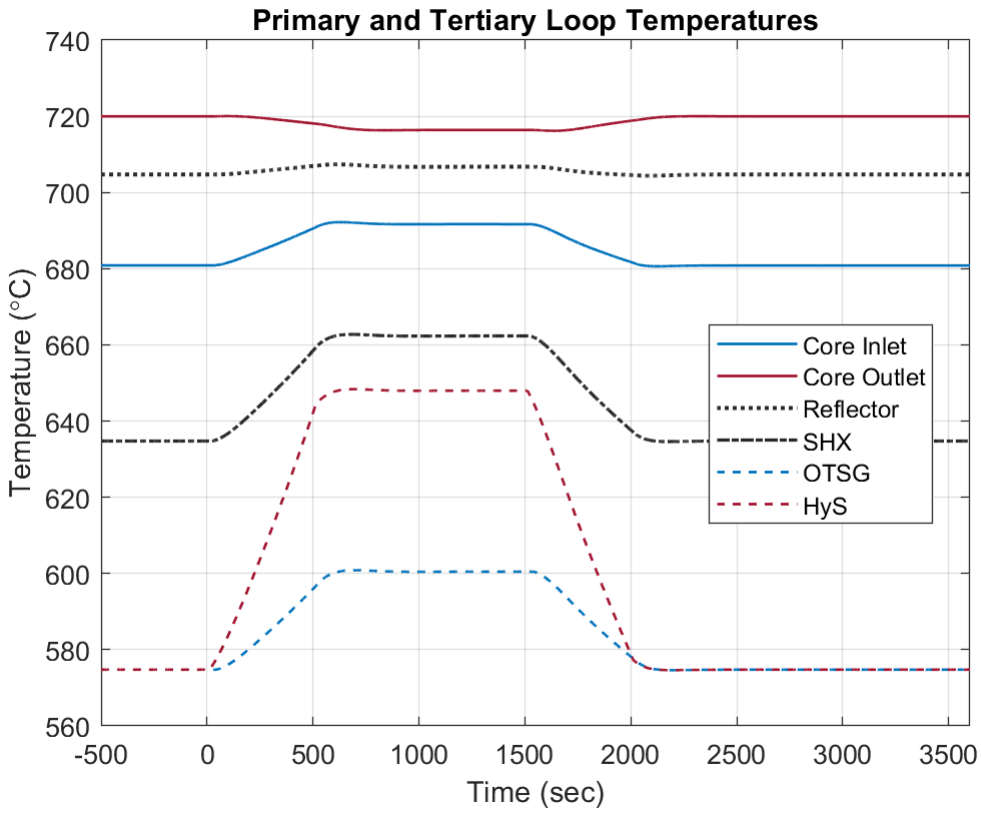


Figure 2.18: Primary and tertiary loop temperatures in response to the decrease in HyS decomposer feed flow rate. The core inlet, core outlet, and reflector temperatures are in the primary loop. The SHX secondary side outlet, OTSG primary side outlet, and HyS decomposer primary side outlet temperatures are in the tertiary loop.

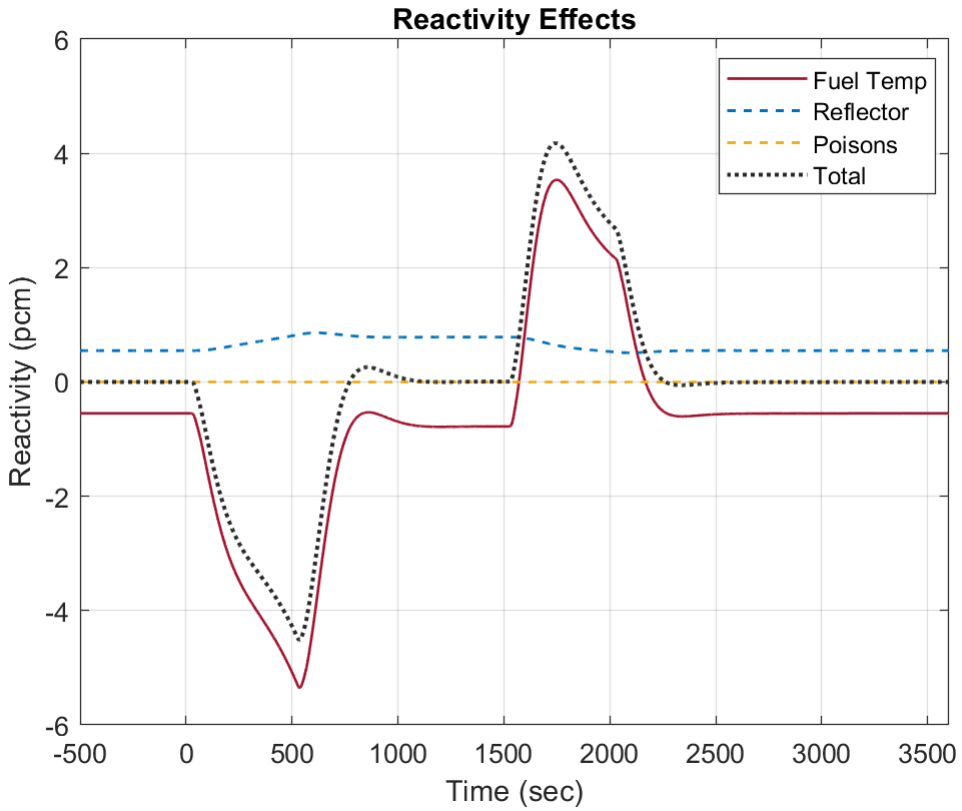


Figure 2.19: Reactivity feedbacks in response to the decrease in HyS decomposer feed flow rate.

With the OTSG, the higher temperature allows for it to further superheat the steam. However, with the HyS decomposer, the higher temperature allows for both further superheating of the sulfuric acid and steam mixture, and also a higher fraction of the sulfuric acid to decompose. The chemical reaction allows for the HyS system to use more energy. This phenomenon is evident by the HyS power usage at 1000 seconds in Figure 2.14 being higher than the OTSG power usage at the same time in Figure 2.17.

## 2.6 Conclusion

Closer connection between power production and usage in an Integrated Energy System (IES) allows for greater efficiency and utilization of nuclear power. The majority of hydrogen production today emits carbon. Clean hydrogen produced from nuclear power represents a novel utilization of nuclear energy outside of electrical production. The purpose of this work is to perform initial scoping analysis on the behavior and safety of a nuclear powered IES which produces both hydrogen and electricity. The IES dynamic model developed in OpenModelica and used in this work tracks the heat transfer through the system from production in the MCFR core with modified point kinetics to electricity production using the Rankine cycle and hydrogen production using the hybrid sulfur cycle. The four scenarios simulated in this work were a RIA based on control rod withdrawal, a LOFA in the primary loop, a LOHSA on the electricity production system, and a LOHSA on the hydrogen production system.

In the RIA scenario, the power pulse from the reactivity insertion peaked at 5.22 times the nominal power level 54.55 seconds after the start of the transient. Without any operator action, the negative feedback coefficient due to temperature brings the power down to a new steady state of 1.2 times nominal power within 500 seconds of the start of the transient. At that new steady state, the temperature in each of the loops is approximately 150°C higher than nominal. In the LOFA

scenario, after the primary pumps are tripped, the reactor power reaches a minimum of 14% nominal at approximately 200 seconds before ascending to a new steady state of 69% nominal power at approximately 2000 seconds. At the new steady state, the maximum fuel salt temperature increased by 50°C whereas the minimum decreased nearly 180°C. As expected, the two LOHSA scenarios produced similar results wherein the reactor power decreases to a steady state of approximately 64% nominal. The system experiencing the feed flow rate decrease also sees a proportional decrease in thermal power usage. Conversely, the other system will slightly increase its thermal power usage due to the 25°C increase in the SHX secondary side outlet.

The results presented in this work provide initial information about the safety of a MCFR style advanced reactor and its use in powering an IES. The potential inherent safety of the system in response to off-nominal conditions is primarily due to the negative fuel temperature reactivity coefficient, which decreases reactor power without operator input. Furthermore, the fast-spectrum of the MCFR core and the offgas removal keep the reactivity effect from fission product poisons five orders of magnitude lower than the other effects. This feature allows for the reactor to load follow far easier than convention light water reactors. The research conducted in this work is planned to continue with an investigation of the frequency response characteristics of this IES model and their dependence on the mass of the SHX.

# Chapter 3

# Expanded Accident Scenarios and Frequency Characteristics for a Molten Salt Reactor in an Integrated Energy System

*This chapter is planned to be submitted as an individual journal article. It will be submitted to Nuclear Science and Engineering for an article collection on Nuclear Energy Research and Development at the University of Tennessee. I am the primary author. The other authors are Dr. Sandra Bogetic and Dr. Nicholas Brown. I primarily wrote the entire paper. Dr. Bogetic and Dr. Brown both helped review and improve the content of the paper. The only edit between the version presented here and that planned to be submitted to the journal is the removal of the abstract. The published version is likely to have changes from the review process.*

## 3.1 Introduction

Advanced nuclear reactor designs coupled directly with multiple industrial processes, particularly for non-electric uses, have many potential advantages but little to no operating experience. As energy demand rapidly increases globally, there is added value in novel computer modeling of these complex interconnected systems to scope their behavior. The work presented in this paper takes an open-source dynamic model of an integrated energy system (IES) and uses it to investigate the frequency characteristics of the system and two accident scenarios specific to the heat utilization systems. The specific IES being tested is a fast spectrum molten salt reactor (MSR) with circulating fuel, and is being used to power two industrial processes: a regenerative Rankine cycle for electricity production, and a hybrid-sulfur cycle for hydrogen production.

The frequency characteristics of the IES are tested by inputting a small sinusoidal reactivity wave of a known amplitude and frequency into the reactor core, then observing the resulting sinusoidal response in terms of thermal power production, electrical power production, and hydrogen production. The objective of these simulations is to isolate and determine the effect that the frequency of a repeated perturbation has across the IES. Furthermore, the simulations are repeated at all points within the tested frequency range but with a different thermal manifold mass to investigate the potential effects its size may have, due to it being the connection between the three systems. The hypothesis behind this study is that the IES has one or more resonant frequencies, in which the amplitude of the production response will be higher than at other frequencies. Similarly, it is hypothesized that the mass of the thermal manifold will proportionately affect the amplitude at a resonant frequency.

Two accident scenarios specific to the heat utilization systems in the IES are simulated in this work. The accident scenario for the Rankine cycle balance of plant is a loss of cooling water in the condenser. For the hybrid-sulfur cycle hydrogen production system, the accident scenario simulated in this work is a loss of the

chemical separator. The loss of the separator leads to the removal of the sulfur from the cycle. The organization of this paper is as follows. First, detailed discussion on the context of this paper within its project and the wider state of understanding on this topic in Section 3.2. Next, explanation on how the the simulations and data analysis in this work are performed in Section 3.3. The results of the simulations and discussion on the lessons learned from them in Section 3.5; followed by the conclusions of this work along with potential future work in Section 3.6.

## 3.2 Background

This paper is a direct followup to a previous paper on the development of the open-source IES dynamic model which was used in this work. The previous paper, titled "Dynamic Modeling of a Fast Spectrum Molten Salt Reactor Integrated Energy System", focuses on the design methodology and capabilities of the model along with accident scenarios relating to the reactor. [86] The wider context of these papers is a Department of Energy Nuclear Energy University Program (NEUP) project on the use of MSRs directly coupled to industrial processes in an IES. The specific title of the NEUP project is "Design and intelligent optimization of the thermal storage and energy distribution for the TerraPower Molten Chloride Fast Reactor in an Integrated Energy System (IES)". [22, 23] The project is led by the University of Tennessee in collaboration with the University of Illinois at Urbana-Champaign (UIUC), Oak Ridge National Laboratory, and Terrapower. Detailed specifics of the project goals are described in the project abstract. [24]

The NEUP project that this work is apart of has already published several papers and summaries. The first of these publications include an investigation of what chemical processes could be included in an MSR powered IES. [25] In parallel, a historical analysis was written on the Aktau nuclear power plant, which was a sodium-cooled fast reactor that produced primarily desalinated potable water but also electricity and district heating as byproducts. [26] Terrapower's Molten Chloride

Fast Reactor (MCFR) was determined to be the primary MSR design focused on in the project. A detailed neutronics model has been developed and demonstrated based on the MCFR's design. [27, 28] The neutronics model has since been used to provide the neutronics parameters (i.e. point kinetics, feedback coefficients, etc) for the reactor in the IES dynamic model used in this work. [29] While the IES model used here is for hydrogen and electricity production, a separate IES model was developed through this NEUP project that focuses on desalination and district heating similar to the Aktau nuclear power plant. [31] Another aspect of the NEUP project has been investigating and postulating IES specific transient events and their safety related consequences. [32]

## 3.3 Methodology

The IES model used in this work is an open-source dynamic model built in OpenModelica. The model is comprised of three systems: an MCFR-like MSR for heat production, a regenerative Rankine cycle with a once-through heat exchanger (OTSG) for electricity production, and a hybrid sulfur (HyS) thermochemical and electrolysis cycle for hydrogen production. [86] The model tracks the production, transfer, and usage of energy throughout the IES along with the tracking of decay heat, fission product poisons, neutron population, and chemical reaction rates. The main grouping of components in the three systems of the IES are shown in Figure 3.1. In the IES, heat is produced in the MSR core and primary loop, flows through the primary heat exchangers, and then out through the secondary heat exchanger (SHX). The secondary heat exchanger also acts a thermal manifold that controls the flow of heat to the Rankine and HyS sides of the IES. The nominal situation in the IES is that half of the flow out from the SHX secondary side goes to the decomposer in the HyS system and half goes to the OTSG in the Rankine system. Both the HyS and Rankine systems nominally use the same amount of thermal power, and thus the flow rate back into the SHX is nominally at the same temperature.

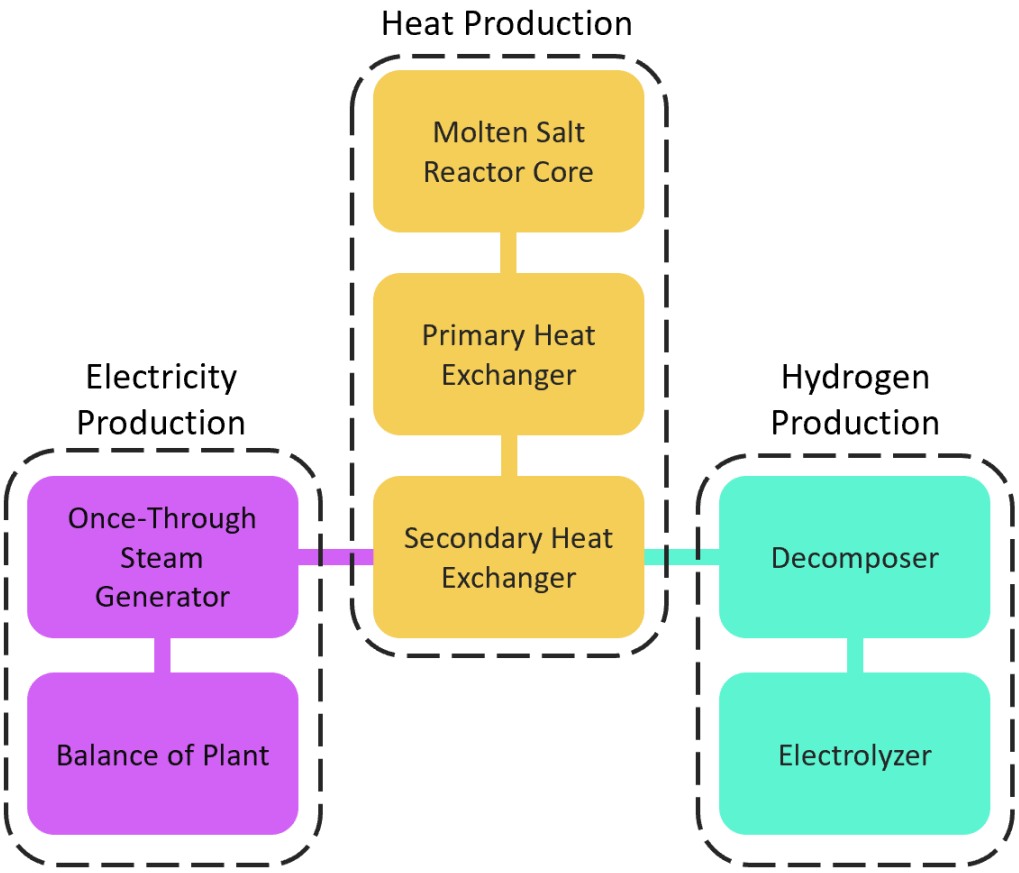


Figure 3.1: Arrangement of the three systems in the IES model, their connection through the secondary heat exchanger, and the organizational grouping of their components.

To determine the frequency characteristics of the IES, a standard transient is tested with only the frequency of the input signal being changed between simulations. The standard transient is a small sinusoidal reactivity insertion in the core. Specifically, the standard transient is a sine wave reactivity insertion with an amplitude of one pcm. The frequencies tested range from 0.0001 radians per second to 100 radians per second (0.000015915 Hz to 15.915 Hz). Each set of simulations are comprised of 150 frequency points spaced evenly on a logarithmic scale within the frequency range. Three sets of simulations were performed for a total of 450 runs. One set was with all nominal masses, one set was with the SHX secondary side mass halved, and one set was with the SHX secondary side mass doubled.

For each simulation, the start of the sinusoidal reactivity insertion is delayed by 1000 seconds to allow the model to settle at nominal conditions across the IES. The total duration of each run was set to a total of 2000 seconds plus the amount necessary for ten periods of the insertion wave. The reason for a variation was to allow for at least several response waves to occur while also keeping the processing time and output file sizes manageable. Having enough periods of the response wave in the output is necessary when attempting to accurately fit a sine wave to the output data. Similarly, each simulation was run with a total of 80,000 intervals to manage the processing time and data file sizes while keeping the sampling rate sufficiently high. According to the Nyquist theorem, the sampling rate must be at least twice that of the given frequency to prevent aliasing. [87] The highest frequency tested in this work is 15.915 Hz and the sampling rate at that frequency is approximately 40 Hz, which satisfies the Nyquist criterion. At the lowest frequency, 0.000015915 Hz, the sampling rate is 0.1269 Hz, which is nearly 8000 times larger. These considerations are necessary due to the wide frequency range being investigated, which is six orders of magnitude. To put that frequency range into a more easily understood context, it goes from one cycle every 17.47 hours to one every 0.0628 seconds, which is at the lower limits of human hearing. [88]

The output data file produced by each run is a csv file with the time at each step, the thermal power output of the reactor, the electrical power output of the turbines in the Rankine cycle balance of plant (RBOP), and the hydrogen production in the HyS electrolyzer. To process the data, a python script is used to fit a sine wave equation to the output data, starting from where the input signal reaches that component. The sine function fit produces an amplitude and phase shift for that particular production output and frequency. The primary results of the frequency analysis are gain and phase bode plots across the frequency range for each of the three outputs: thermal power output, electrical power output, and hydrogen production output. These results are presented and discussed along with the lessons learned and limitations of this method in Section 3.5.

There are major caveats of analyzing the frequency characteristics of this IES dynamic model due to the assumptions in the modeling methodology. These specific assumptions are: the model is design agnostic and has no spatial distribution or set piping arrangement; the model describes components as a collection of lumped-parameter control volumes; and the model describes transit times as time delays between components. The assumptions used in the IES model allow for rapid processing times and investigation of energy transfer behavior generic to most designs. In regards to frequency analysis, the specific piping arrangement and residency times within specific parts of a heat exchanger or similar component could reasonably expected to effect the frequency characteristics. For example, a sinusoidal temperature change flowing into the primary side of a physical heat exchanger at a suitably high frequency or transit speed could travel through the component without maximally propagating itself into a corresponding temperature sinusoid leaving the secondary side of the heat exchanger. Similarly, the spatial design of the heat exchanger may lead to differences in local temperature that have a corresponding effect on the transmission of the temperature signal. However, the focus of this work is on the use of frequency analysis across the entirety of a novel fast spectrum MSR-powered IES design with non-electric energy application. It is for that reason that the

outputs analyzed herein (i.e., thermal power production, electrical power production, and hydrogen production) are at opposite ends of the IES. Additional discussion on the limitations and veracity of frequency analysis on this model is included with the results.

To further investigate the safety related energy transfer behavior due to having an IES coupled to an MSR, two accident scenarios were simulated with the model. Both scenarios are specific variants of what could generally be categorized from the perspective of the reactor as a loss of heat sink accident. Each scenario is specific to one of the two heat utilization systems in the IES design (i.e., regenerative Rankine cycle for electrical power production, and hybrid-sulfur cycle for hydrogen production). The accident scenario for the electrical production side is a loss of cooling water to the condenser. The scenario begins with the cooling water flow rate at its nominal flow rate of 20,000 $\frac{kg}{s}$. The cooling water pump is then tripped and decreases along an exponential decay curve with a decay constant of 0.092 and a minimum of 1% of the nominal flow rate. The hypothesis is that the decreased heat rejection rate will increase the temperatures throughout the Rankine cycle and decrease the thermal power used by it. The physical basis for the heat sink failure specific to the HyS cycle hydrogen production system is rupture in the chemical separator between the condensation and electrolysis steps of the cycle. The failure in the separator leads to a loss of sulfur in the system. Without sulfur, the decomposition and electrolysis reactions cannot occur and only water will flow through the HyS components. The scenario is similarly modeled as a flow rate trip with an exponential decay curve. The hypothesis for the separator failure is that with only water going through the HyS cycle, the thermal power used by the cycle will decrease, which will cause an increase in temperatures in the other loops. The results of these two accident scenarios are shown in Section 3.4.

## 3.4 Heat Sink Accident Results

Two loss of heat sink accidents were simulated to investigate the effects that a significant failure in one of the two energy utilization systems in the IES would have to the system without any automated or operator action. The two accident scenarios included here are: a loss of cooling water in the Rankine cycle condenser, and a separator failure leading to loss of sulfur in the hybrid sulfur cycle. Both scenarios are represented by a respective flow rate trip. The results of the condenser failure are shown and discussed in Section 3.4.1. The results of the separator failure are shown and discussed in Section 3.4.2.

### 3.4.1 Loss of Cooling Water in Rankine Cycle Condenser

The thermal power production and usage in response to the loss of cooling water in the Rankine cycle condenser are shown in Figure 3.2. In the figure, the thermal power usage by the OTSG decreases by nearly 17% and settles there as a new steady state within the first hundred seconds. The thermal power production in the core proportionally decreases by approximately 8.5% to a new steady state reached after a few hundred seconds. These steady state thermal power production and usage hold for the remainder of the one hour simulated scenario window. The primary and tertiary loop temperatures are shown in Figure 3.3. In the figure, the temperature gradient in the primary loop narrows to nearly 35.5 °C. The primary side outlet temperature of the OTSG increases by approximately 20 °C. The increased temperature propagates back upstream through the fluid loops, which leads to the decrease in reactor power. The individual reactivity feedbacks for the transient are shown in Figure 3.4.

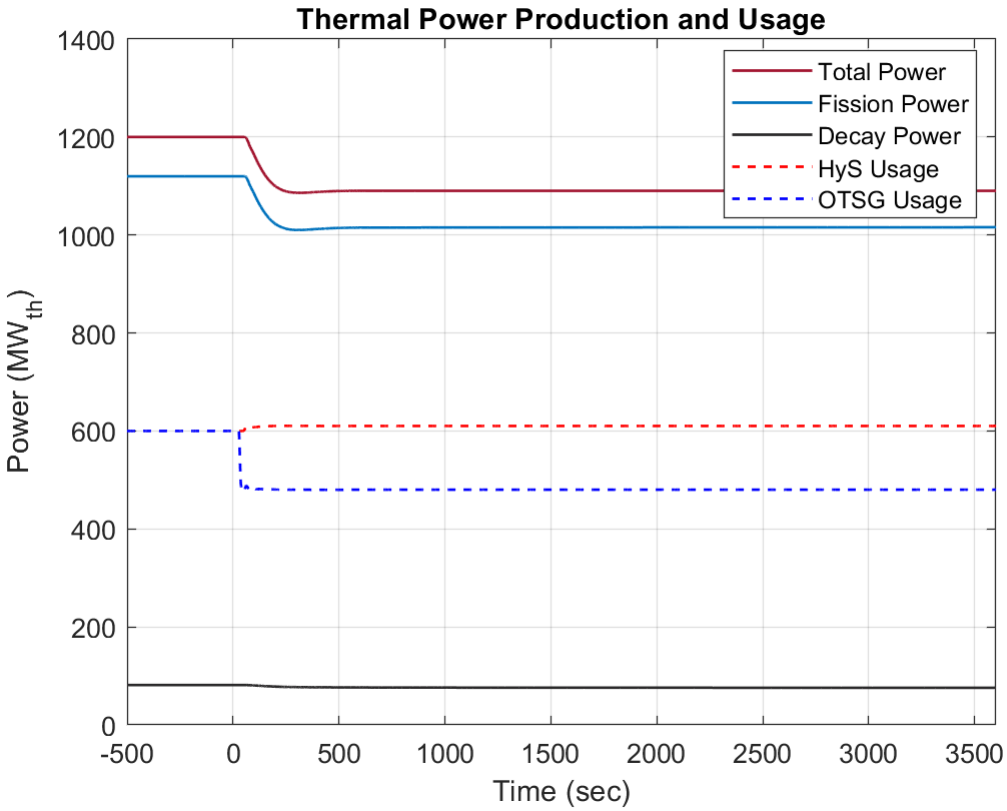


Figure 3.2: The thermal power production and usage in response to the condenser cooling water pump being tripped. Solid lines are indicative of power production and dashed lines are power usage.

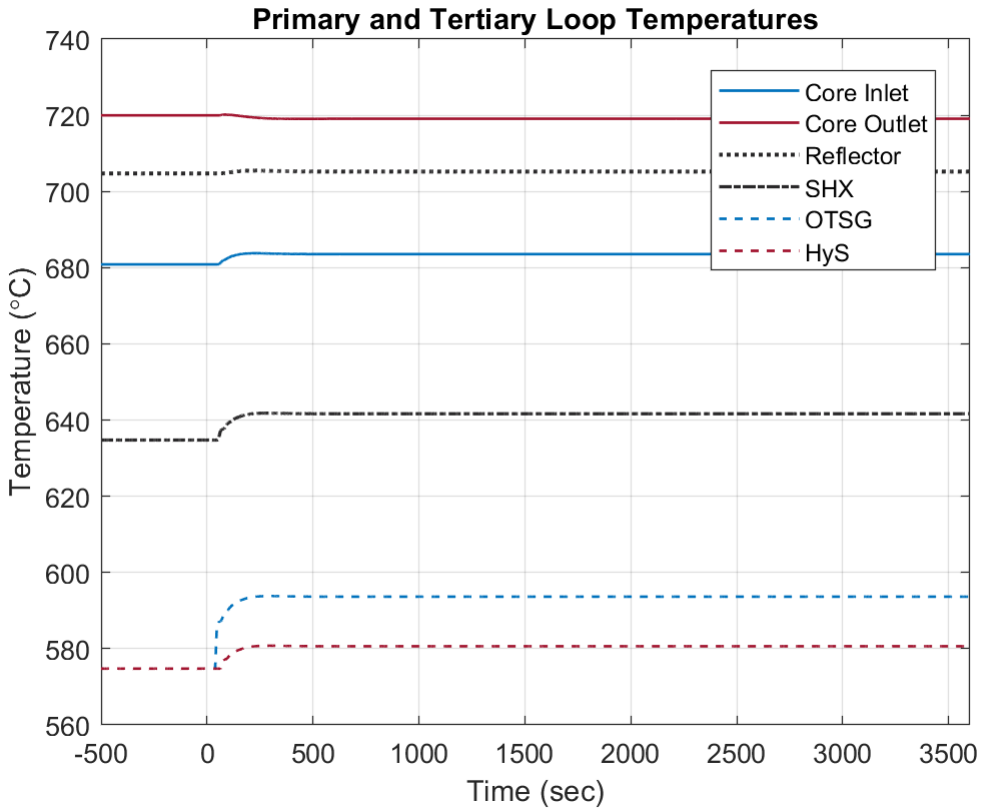


Figure 3.3: The primary and tertiary loop temperatures in response to the condenser cooling water pump being tripped. The core inlet, core outlet, and reflector temperatures are in the primary loop. The SHX secondary side outlet, OTSG primary side outlet, and HyS decomposer primary side outlet temperatures are in the tertiary loop.

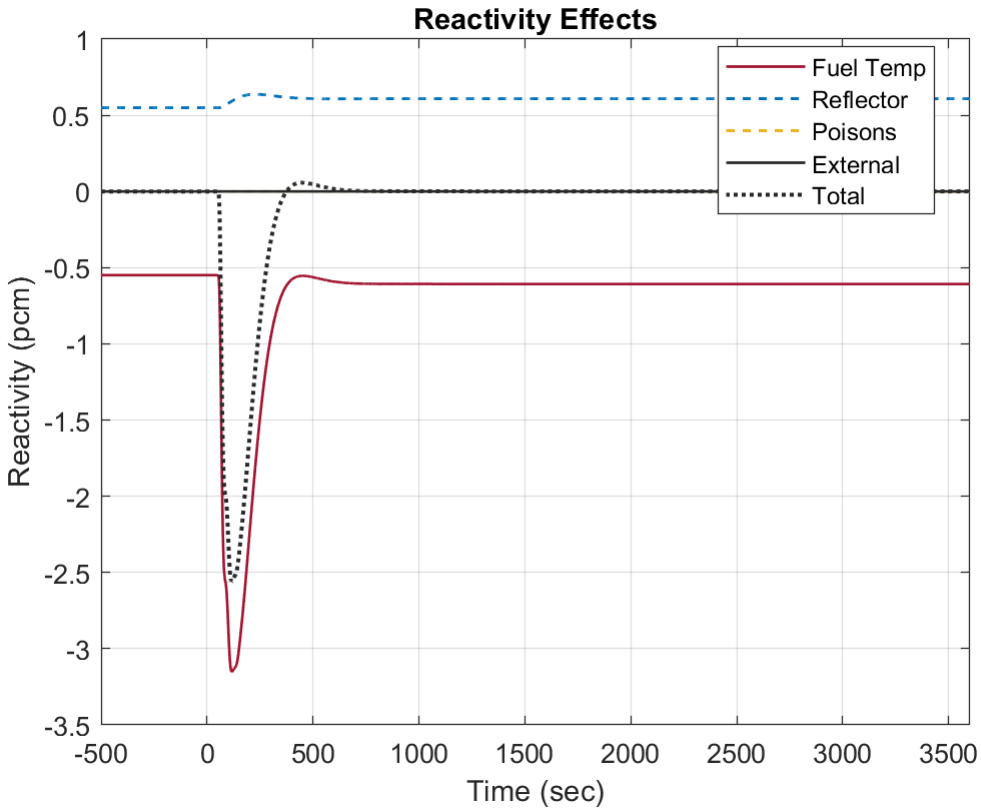


Figure 3.4: The reactivity feedbacks in response to loss of flow in the condenser cooling water pump being tripped.

The net reactivity remains low with a maximum magnitude of 2.5 pcm at approximately one hundred seconds into the scenario. For context, the non-zero reactivity due to fuel and reflector temperature settling 0.3 °C apart from what is set as nominal in the model parameters after initialization. Overall, these results show inherent safety behavior for the IES in response to a failure in the Rankine cycle. When the thermal power usage decreases, the temperatures in the loop increase and lower the thermal power production.

### 3.4.2 Loss of Sulfur in Hybrid Sulfur Cycle Separator

The thermal power production and usage in response to the loss of the separator in the HyS are shown in Figure 3.5. In the figure, the thermal power usage by the OTSG decreases by nearly 95.5% and settles there as a new steady state within the first hundred seconds. Notably, this power usage level is less than even the decay power production. With the overall thermal power usage nearly halved, the temperatures in the loops increase, which causes a decrease in the thermal power production. The thermal power production in the core decreases by approximately 46% to a new steady state reached after several hundred seconds. These steady state thermal power production and usage hold for the remainder of the one hour simulated scenario window with no power fluctuations. The primary and tertiary loop temperatures are shown in Figure 3.6. In the figure, the temperature gradient in the primary loop narrows to nearly 21.1 °C. The primary side outlet temperature of the HyS decomposer increases to only 2.7 °C difference than the SHX secondary side outlet temperature, which similarly increases by nearly 30 °C. The increased temperature propagates back upstream through the fluid loops, which leads to the decrease in reactor power. The individual reactivity feedbacks for the transient are shown in Figure 3.7.

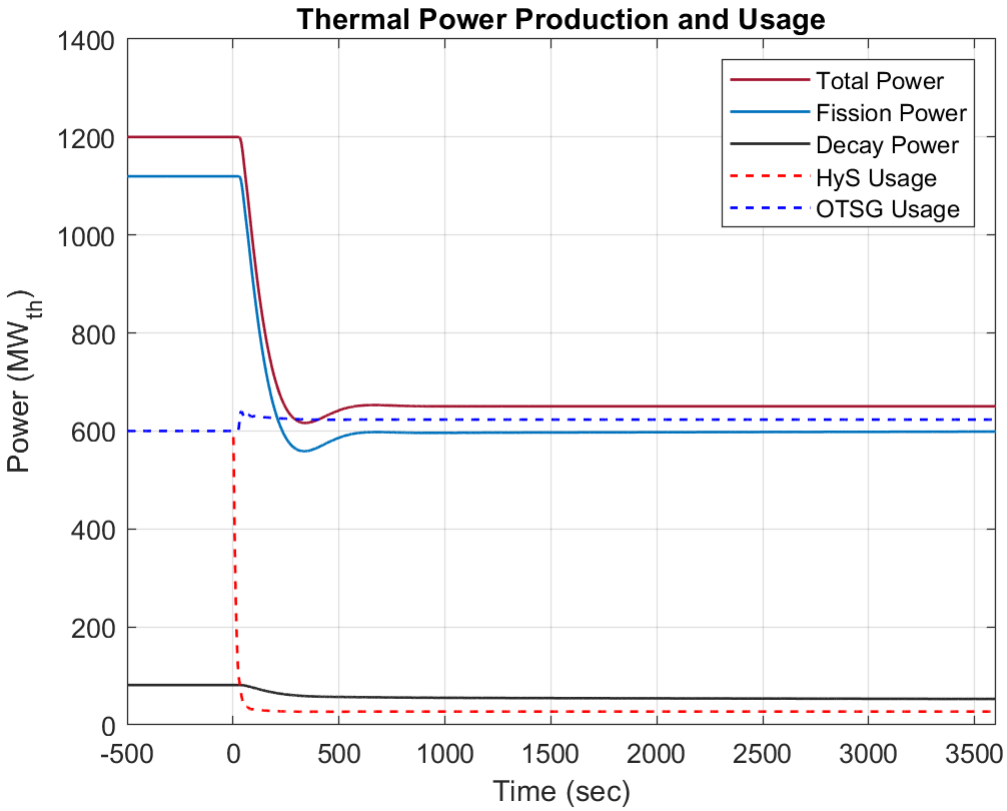


Figure 3.5: The thermal power production and usage in response to the HyS separator failure. Solid lines are indicative of power production and dashed lines are power usage.

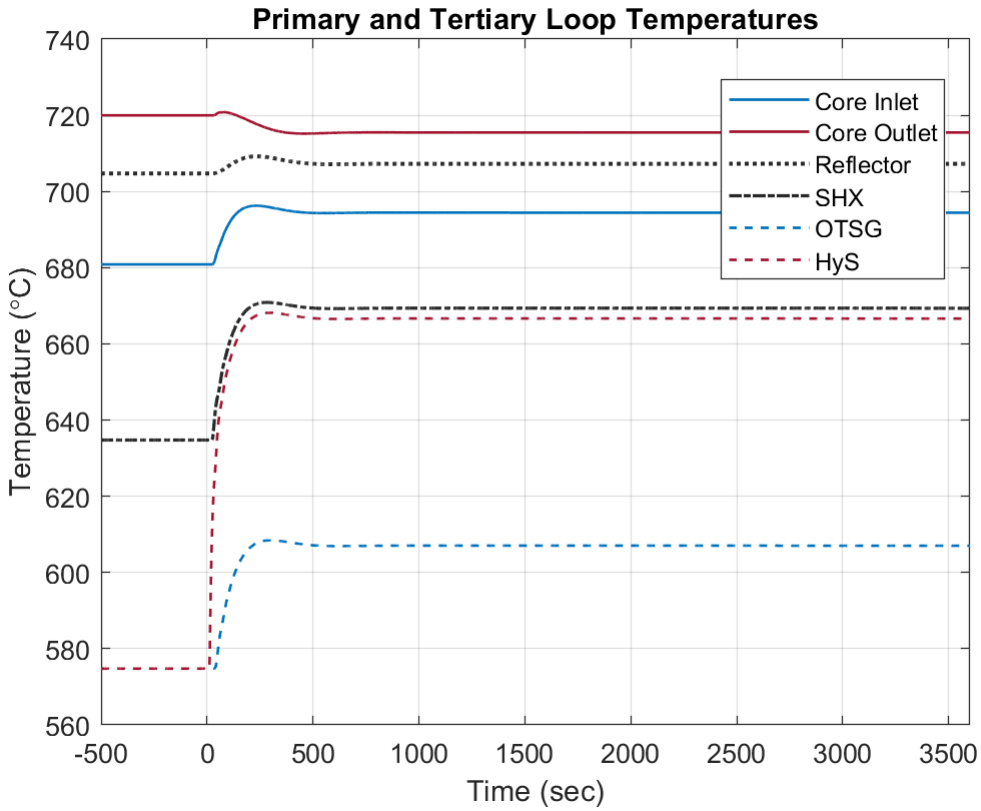


Figure 3.6: The primary and tertiary loop temperatures in response to the HyS separator failure. The core inlet, core outlet, and reflector temperatures are in the primary loop. The SHX secondary side outlet, OTSG primary side outlet, and HyS decomposer primary side outlet temperatures are in the tertiary loop.

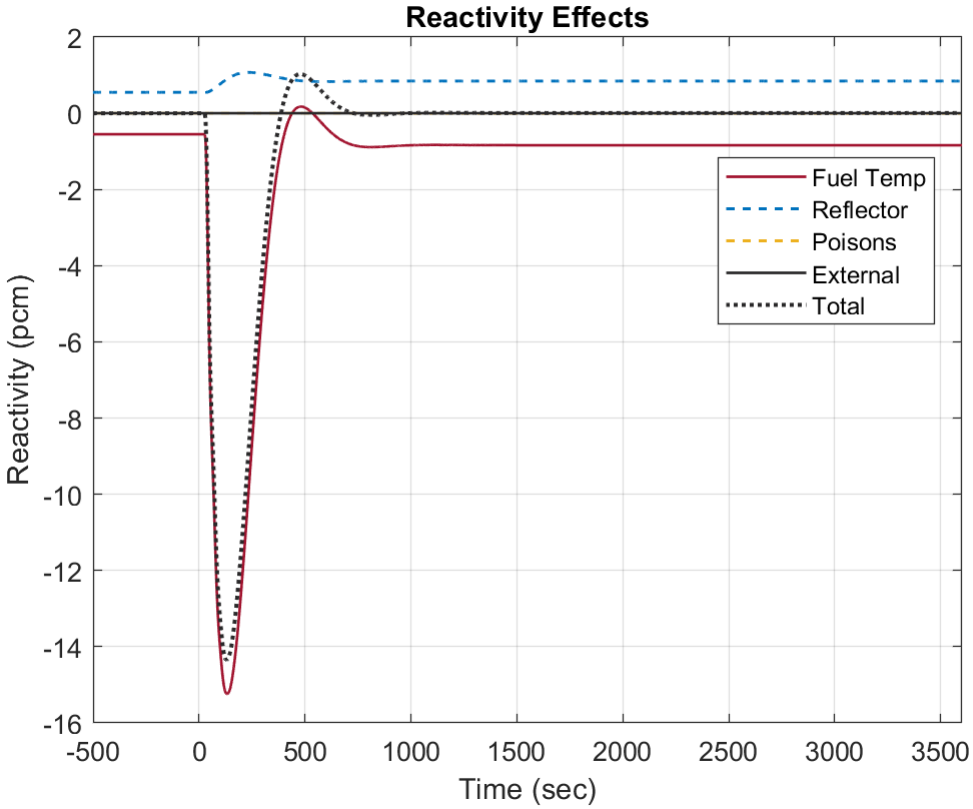


Figure 3.7: The reactivity feedbacks in response to loss of flow in the HyS separator failure.

The shape of the overall curve is the same as with the Rankine cycle condenser failure scenario but with a larger magnitude. The net reactivity has a maximum magnitude of approximately 14.2 pcm at around one hundred seconds into the scenario. Overall, these results show also inherent safety behavior for the IES in response to a heat sink failure. In comparison to the previous scenario, the HyS separator failure results in similar but more severe changes than the Rankine cycle condenser failure.

## 3.5 Frequency Analysis Results

The results shown here are the gain and phase shift bode plots for the three outputs: thermal power, electrical power, and hydrogen production. Each result is repeated with the SHX secondary side fluid mass either at nominal, halved, or doubled in an effort to investigate the effect that the size of the thermal manifold has on the frequency characteristics of the IES. Gain and phase are useful descriptors due to the results being displayed in the form of bode plots. However, it is important to remember the physical reality being modeled here. The use of bode plots to describe the frequency characteristics of a large and complex interconnected system, such as the IES in this work, is novel and not wholly analogous to the small electrical systems which are generally described by bode plots. The use of bode plots here is purely to isolate the effect frequency has on the IES. In this work, gain is displayed linearly as the relative increase of the output sine wave amplitude corresponds to. Phase is represented by degrees, which is a difference in time between the crest in the input wave to the output wave, relative to the period of the waves, which are shared.

The arrangement of this section is as follows. First, the thermal power output, hydrogen production output, and electrical power output results are shown and discussed in Sections 3.5.1, 3.5.2, and 3.5.3, respectively. Lastly, examples of the outputs at the middle and high frequencies are shown in Section 3.5.4 to aid in the discussion of the physical phenomenon.

### 3.5.1 Thermal Power Output

The thermal power gain results in response to the 1 pcm reactivity sine wave are shown in Figure 3.8. In the figure, it can be seen that the effect due to the mass of the thermal manifold is minimal, with exception to the size peak seen at approximately 0.022 radians per second (0.0035 Hz). At larger thermal manifold masses, the peak is smaller. For the thermal power output, it is expected that the effect due to SHX mass will be minimal. This expectation is due to the reactivity input and thermal power output being primarily within the core. Any effect from the SHX mass would have to propagate first through the primary and secondary loops, and then return through the same path. The peak at 0.022 radians per second is indicative of resonance occurring at and around that frequency. At the lower frequencies, the amplitude of the thermal power output decreases linearly before plateauing at an amplitude of around 0.037%. Likewise, for higher frequencies, the amplitude decreases steadily until it reaches an amplitude of 0.24% at around one radian per second frequency. From there, the amplitude does not fully plateau like with the low frequency side, and instead slowly decreases for the next two highest frequency magnitudes, at which it reaches an amplitude of 0.152% at 100 radians per second.

The thermal power phase results in response to the standard transient across the frequency range is shown in Figure 3.9. In the figure, it is seen that the effect due to the SHX mass is negligible. The agreement between the three sets of runs is nearly absolute, with only slight difference around 0.01 radians per second. At the lowest frequencies, the phase shift starts at approximately 10 degrees and increases steadily to 66.96 degrees at about 0.003 radians per second. After which, it decreases down to a local minimum of -27.62 degrees before raising back to around -5 degrees.

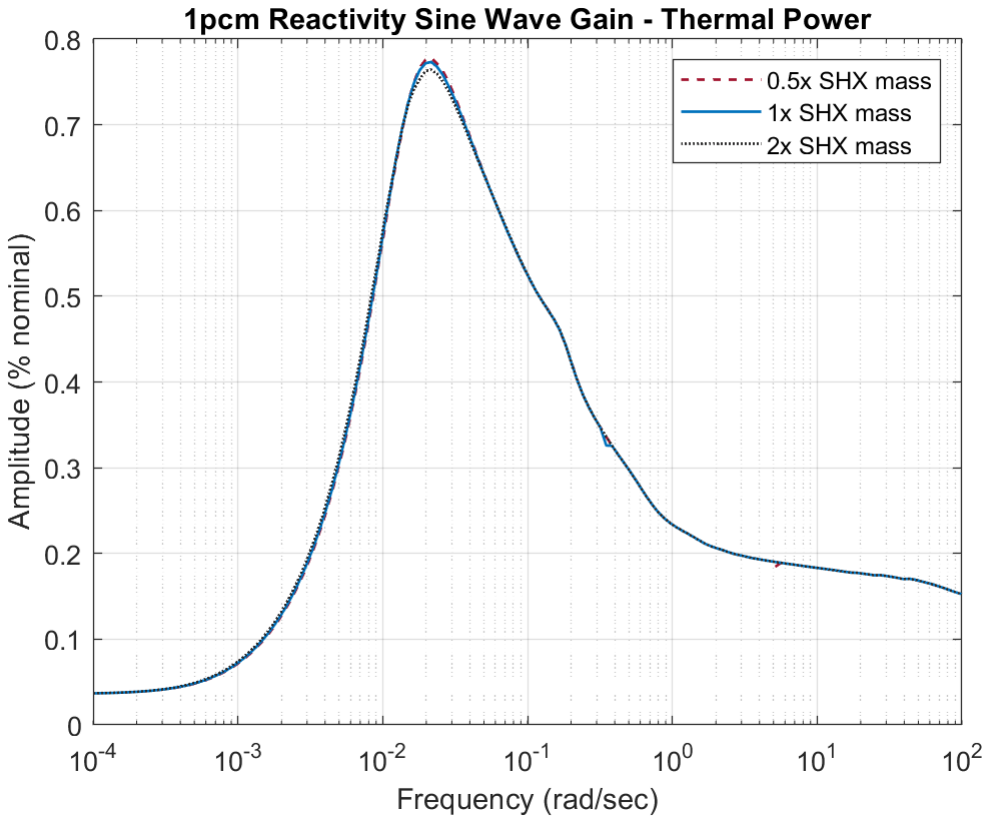


Figure 3.8: Amplitude of the thermal power output, in response to a 1 pcm amplitude sine wave insertion across the frequency range, as percentage relative to nominal conditions.

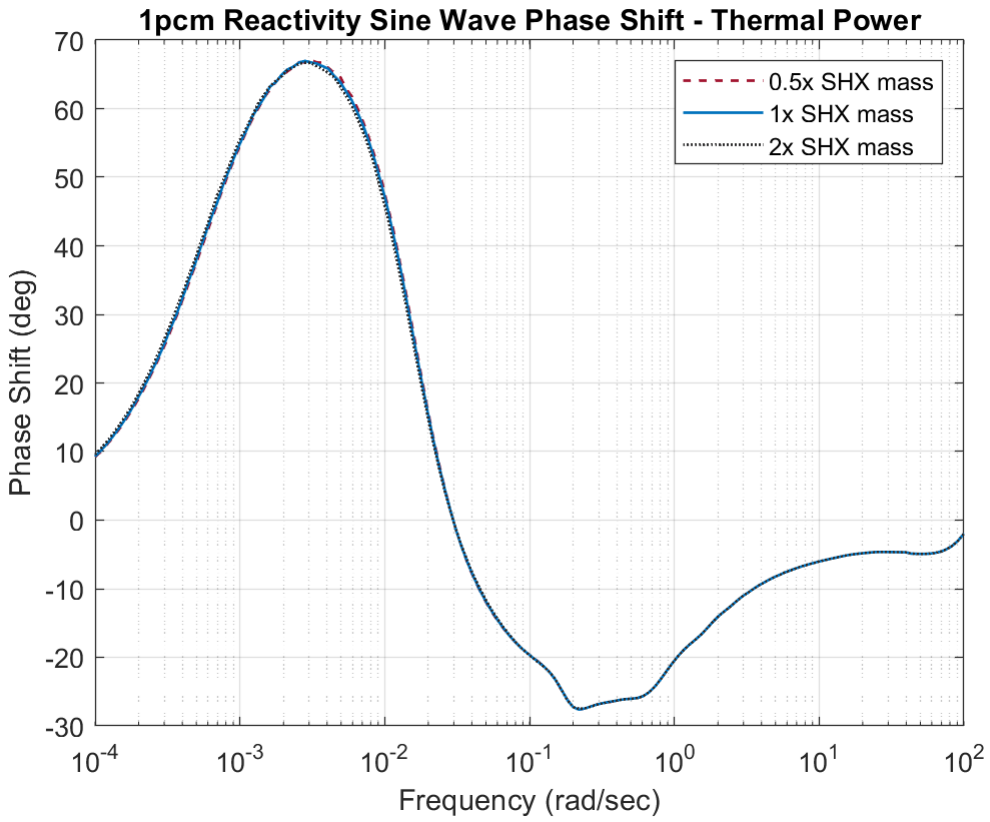


Figure 3.9: Phase shift of the thermal power output, in response to a 1 pcm amplitude sine wave insertion across the frequency range, as degrees relative to the period of the input signal.

In this context, it is beneficial to remember that degrees are relative to the period of the input and output waves. At the lowest frequency, a phase shift of 10 degrees represents a time delay of approximately 1745 seconds. Whereas, the peak of 66.96 degrees at about 0.003 radians per second represents a time delay of approximately 407 seconds. At the highest frequency magnitudes, where the period of the waves is less than a second, the phase shift similarly represents a time delay of less than a second.

### 3.5.2 Hydrogen Production Output

The hydrogen production output gain results are shown in Figure 3.10. There are a few clear differences between the hydrogen production gain and thermal power gain discussed previously. Firstly, the maximum relative amplitude for the thermal power was 0.77%, whereas for the hydrogen production, it is multiple times smaller at 0.16%. Another difference is that there is not one single large resonance peak. Instead, the hydrogen production amplitude is at global maximum plateau at the lower two frequency magnitudes. From there, as the frequency increases, the amplitude steadily decreases until it reaches a local maximum between 0.1 and 0.2 radians per second. The local maximum in that frequency range, centered at approximately 0.18 radians per second, indicates some resonance occurring around there. After which, at higher frequencies (i.e., 0.3 radians per second and above), the amplitude decreases further to nearly zero. Specifically, the amplitude in the highest frequency magnitude plateaus at around $10^{-5}$ % of nominal hydrogen production. Overall, the effect the SHX mass has on the hydrogen production amplitude is that the entire curve is shifted leftward with higher thermal manifold mass. From the input signal in the core, the temperature perturbation caused by the reactivity change has to propagate through the primary loop, secondary loop, tertiary loop, and then through the HyS decomposer. Therefore, with more fluid in the tertiary loop, more material needs to change temperature before the hydrogen production is affected at all.

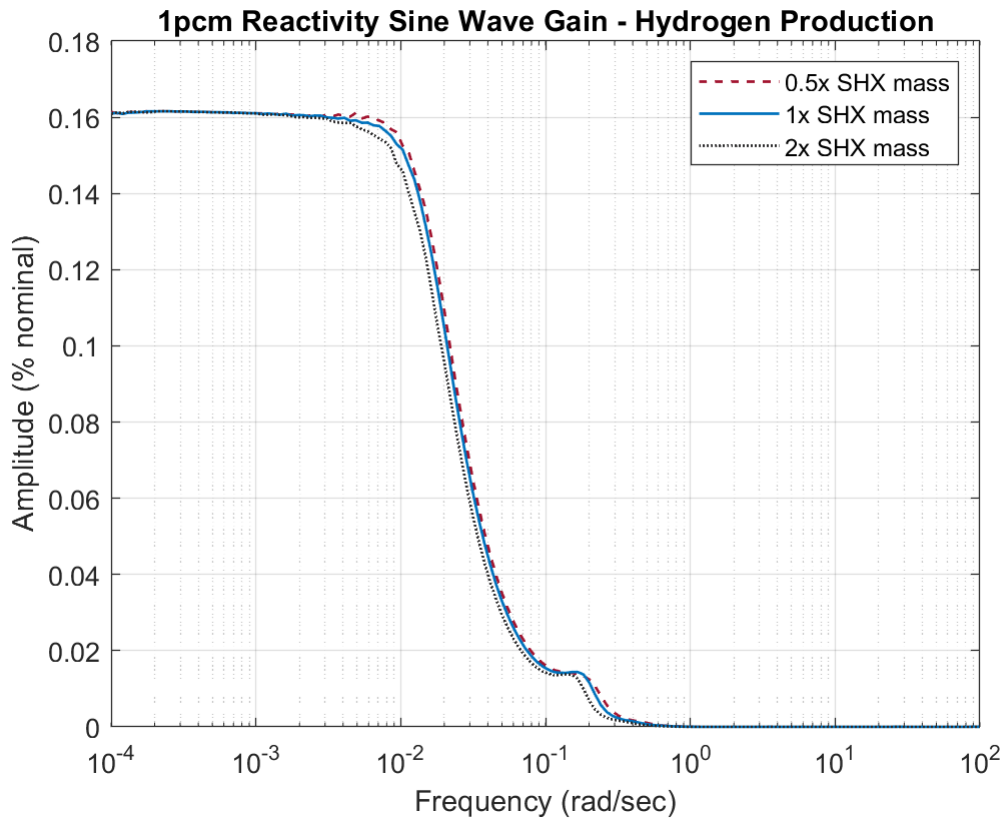


Figure 3.10: Amplitude of the hydrogen production output in response to a 1 pcm amplitude sine wave insertion across the frequency range as percentage relative to nominal conditions.

The hydrogen production output phase results are shown in Figure 3.11. The highest two magnitudes of frequency are not included due to numerical noise dominating at the upper values. The gain results showed that at the higher frequencies the gain goes to nearly zero. As such, the output is more accurately described as a straight line than as a sinusoid, which leads to numerical noise from attempting to fit a sine equation to it. Specific examples of what the output is at the higher and lower frequencies are provided in Section 3.5.4. What the remainder of the results here show is that at the very low frequencies, the hydrogen production is nearly in phase with the reactivity wave. As the frequency increases, the output shifts more and more out of phase with a positive time delay. The phase shift peaks twice at approximately 0.045 and 0.25 radians per second. From there, if the drastic change is ignored, it seems that the magnitude of the phase shift decreases back to zero, where it returns to being in phase with the input signal. The overall effect due to the SHX mass is a downward shift in the curve. With a higher thermal manifold mass, more fluid has to change temperature before the signal through the IES can affect the HyS system. In these results, as the SHX mass increases, the magnitude of the phase shift in the middle frequencies increases.

### 3.5.3 Electrical Power Output

The electrical power production gain results are shown in Figure 3.12. In the figure, a similarly shaped curve to the hydrogen production gain results is seen. This similarity is to be expected, as both systems are separated from the core by a similar amount of material. The differences begin at the tertiary loop, where thermal perturbations have to go through the steam generator and balance of plant to affect the electrical production. Whereas, after the tertiary loop, thermal perturbations have only to go through the HyS decomposer to affect the hydrogen production, discussed in the previous section.

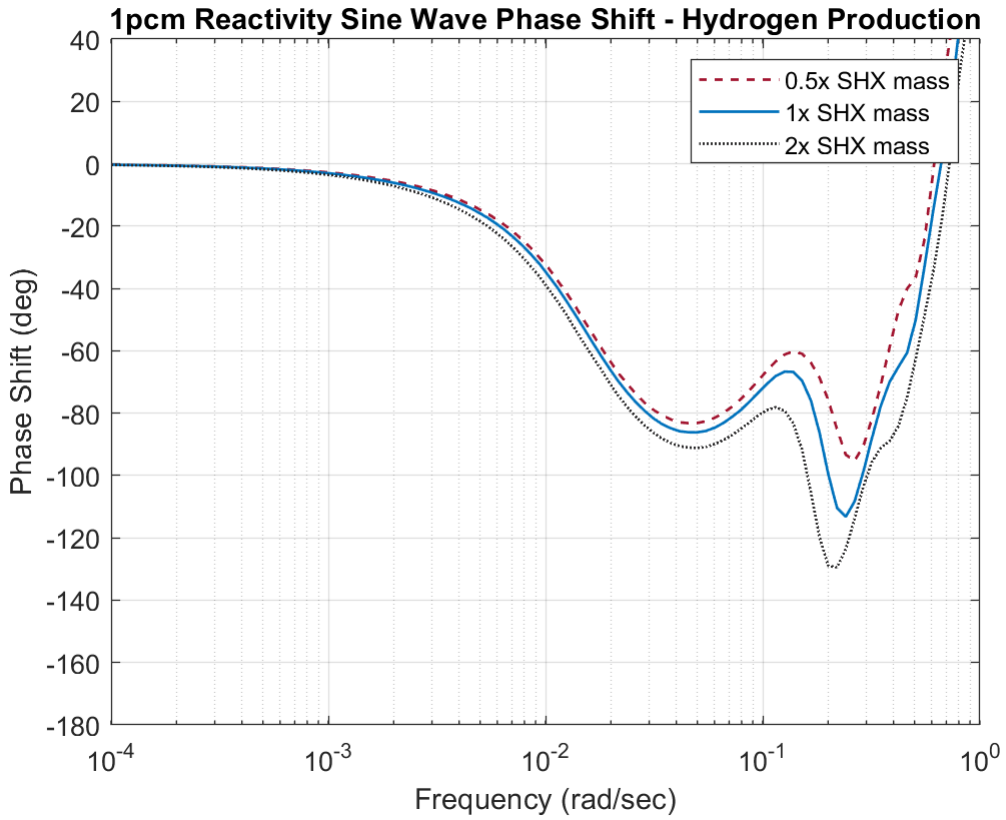


Figure 3.11: Phase shift of the hydrogen production output, in response to a 1 pcm amplitude sine wave insertion across the frequency range, as degrees relative to the period of the input signal.

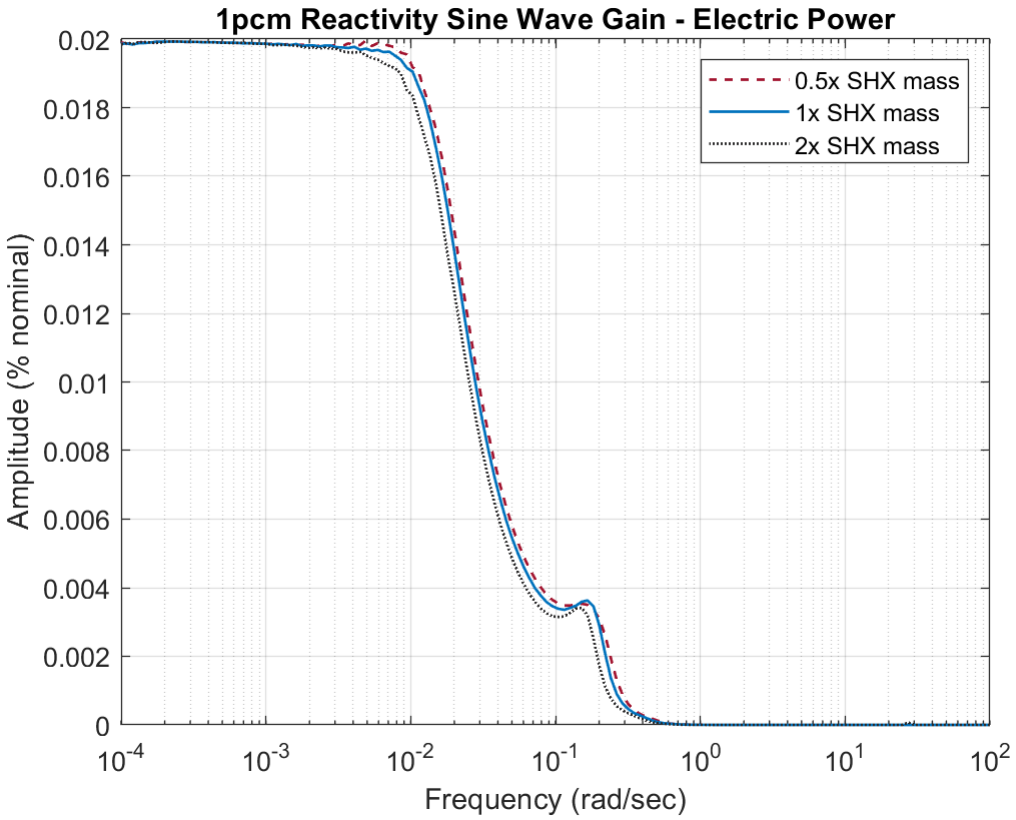


Figure 3.12: Amplitude of the electrical power output in response to a 1 pcm amplitude sine wave insertion across the frequency range as percentage relative to nominal conditions.

Despite the similarly shaped curve, the primary difference between the hydrogen production output results and the electrical power output results is the magnitude of the gain. For the electrical power output, the maximum amplitude seen is nearly 0.02% of the nominal value. This result is comparatively eight times less than seen for the hydrogen production. Keeping with the similarities, it is seen that the effect from the SHX mass is a leftward shift in the curve and that there is resonance centered at approximately 0.18 radians per second. In both the hydrogen and electricity production results, it is seen that, at higher frequencies, the amplitude seen from an input signal diminishes to negligible levels. The leftward shift in the curve due to the SHX mass in both outputs suggests that the true effect of SHX mass is determining the frequency point at which the amplitude at higher frequencies begin to be damped down to nothing. Moreover, this initial study seems to indicate the inaccuracy of the hypothesis that, as the thermal manifold, the SHX mass has particular importance over the frequency characteristics of the IES. Instead of location, the results show that more mass between the input and output signals lowers the frequency beyond which the output gain is minimized. The benefit of this phenomenon is that high frequency noise in one system, due possibly to worn pumps or cavitation, will not be appreciably experienced by the other systems in the IES. Conversely, for lower frequencies, the gain that occurs from input to output signals through the IES will increase as frequency decreases only up to a certain point. Overall, these results indicate that, in regards to the frequency effects between the systems, that the IES is stable and would not suffer due to noise from one system affecting another.

The electrical power production phase results are shown in Figure 3.13. In the figure, the overall pattern is similar to that for the hydrogen production phase results. Specifically, that at the lowest frequencies it starts new zero and decreases further as the frequency increases. Both also experience some numerical noise at the highest two frequency magnitudes.

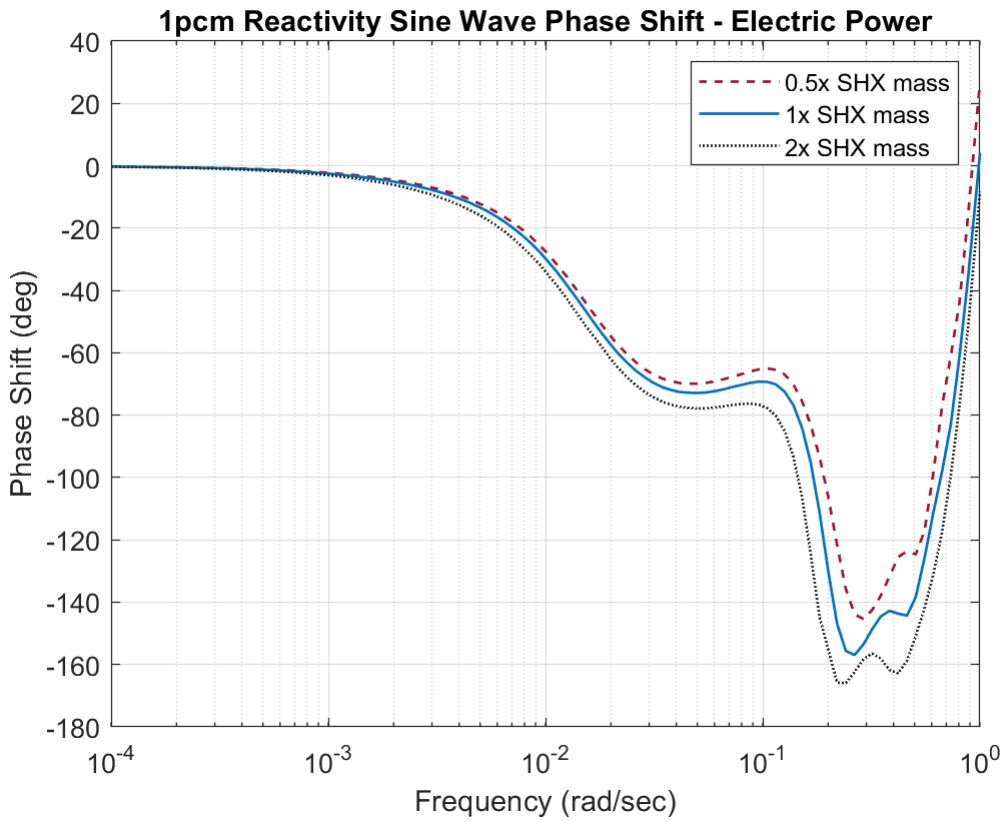


Figure 3.13: Phase shift of the electrical power output, in response to a 1 pcm amplitude sine wave insertion across the frequency range, as degrees relative to the period of the input signal.

In particular, both experience the start of that drastic change at approximately one radian per second. For that reason, the highest two magnitudes of frequency are not included due to the numerical noise dominating at the upper values. The gain results showed that at the higher frequencies the gain goes to nearly zero. As such, the output is more accurately described as a straight line than as a sinusoid, which leads to numerical noise from attempting to fit a sine equation to it. Specific examples of what the output is at the higher and lower frequencies are provided in Section 3.5.4.

### 3.5.4 Results Output Example

One of the foundational assumptions of using bode plots to investigate the frequency characteristics of an IES is that a sinusoidal input signal will produce a sinusoidal output signal. Fitting a sine function to non-sinusoidal data results in numerical noise when determining the phase shift. In the phase shift results for the hydrogen production and electrical power production output signals the higher frequencies were not included due to the numerical noise. The noise in these results is not due to aliasing, as the sampling rate is well above the Nyquist limit, so the possibility for aliasing should be precluded. To determine the cause behind this issue, the output data for two example runs is presented here.

The output data of two example runs at two different frequencies was looked at to demonstrate the general behavior. The output at the lower and middle frequencies is sinusoidal and looks similar to Figure 3.14. In the figure, the electrical power output for the standard transient wave at a frequency 0.0344 radians per second is shown. The reactivity wave input signal begins at the zero second mark. The power output is at nominal up to that point and for an additional amount of time as the temperature differences travel through the loops and propagate through the IES. The first peak in the output signal is larger than the subsequent peaks, which are more similar in size.

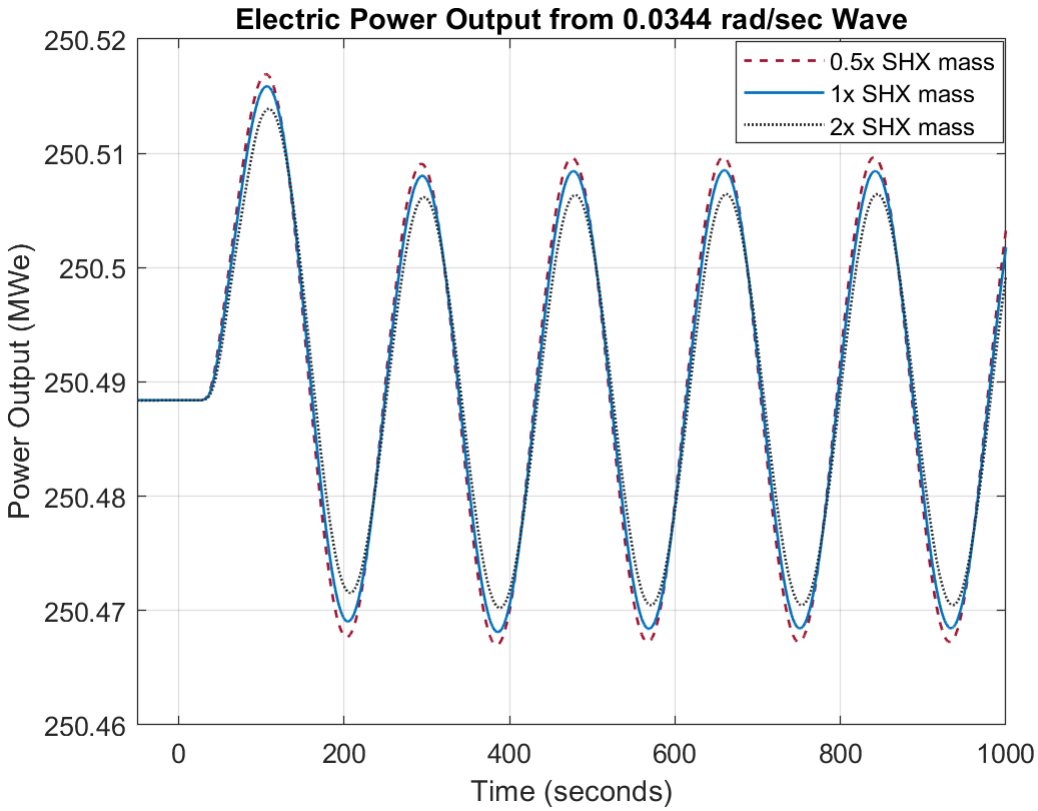


Figure 3.14: Electrical power output from the regenerative Rankine balance of plant in response to a sinusoidal reactivity insertion in the MCFR core with one pcm amplitude and a frequency of 0.0344 radians per second. The solid blue line is the simulation with nominal SHX mass, the dashed red line is for the simulation with the SHX secondary side fluid mass halved, and the dotted black line is for the simulation with the SHX secondary side fluid mass doubled.

This phenomenon is one of the reasons why the simulation needs to be run long enough to produce a sufficient number of peaks. The effect that the SHX mass has on the amplitude and phase of the wave can also be seen in these results. Specifically, that a higher thermal manifold mass decreases the gain and increases the phase shift of the wave. The results at each of the frequency points between $10^{-4}$ and $10^{0}$ radians per second are similarly sinusoidal.

The previous power output results were from near the middle of the frequency range being investigated in this work. The next set of results is in the highest frequency magnitude within the range. These results, shown in Figure 3.15, are the electrical power output results at a frequency of 47.627 radians per second.

A few major differences are made apparent by this figure. Particularly, the non-sinusoidal nature of the data, the small size in the power output amplitude, and the inconsistency from the three SHX masses. The exact cause behind these results is not fully understood, but is conjectured here to be due to the very small amplitude in the power output. The time range on the axes in both of the two example figures is identical. However, the scale of the power output on the y-axis is different by a factor of 750. At the scale used for the sinusoidal results, the non-sinusoidal results appear to be a straight line. Therefore, despite the inability to determine a consistent and specific phase shift, the minimization of the output signal gain reinforces the trends seen in the results. Specifically, the trend that the amplitude at high frequencies gets reduced to near zero.

## 3.6 Conclusion

The use of an advanced nuclear reactor in an integrated energy system (IES) allows for more uses for nuclear power beyond electricity generation. In this paper, two heat sink failures specific to the industrial process they take place in were simulated along with an investigation of the frequency characteristics of the entire IES.

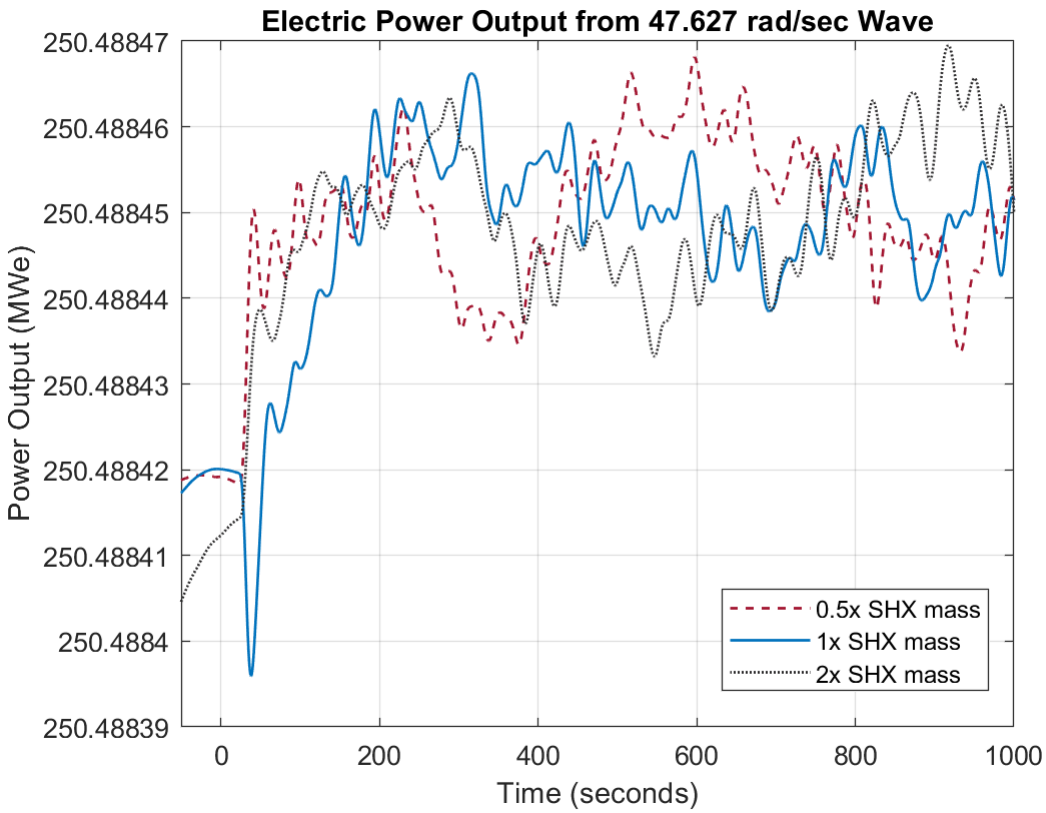


Figure 3.15: Electrical power output from the regenerative Rankine balance of plant in response to a sinusoidal reactivity insertion in the MCFR core with one pcm amplitude and a frequency of 47.627 radians per second. The solid blue line is the simulation with nominal SHX mass, the dashed red line is for the simulation with the SHX secondary side fluid mass halved, and the dotted black line is for the simulation with the SHX secondary side fluid mass doubled.

The two heat sink failures examined are a loss of cooling water in the Rankine cycle condenser, and a loss of sulfur in the hybrid sulfur cycle separator.

The frequency characteristics were determined by producing bode plots from the thermal power, electrical power, and hydrogen production outputs in response to a small sinusoidal reactivity insertion. The insertion has an amplitude of one pcm of reactivity and a frequency ranging from 0.0001 to 100 radians per second. To have a shared unit between the different outputs, the gain in the bode plots is given as the amplitude of the output as a percentage of the nominal amount. The phase shift in the results is given as degrees. The full set of simulations across the frequency range was repeated with the fluid mass of the thermal manifold halved and repeated a third time with the mass doubled.

The results of the two heat sink failure scenarios showed that, in response to the failure, the thermal power used by that system decreases, which increases the temperature in each of the IES loops, decreases the power production in the core, and narrows the temperature gradient across the primary loop. Within minutes of the failure, the IES has reached a new steady state with lower power production and higher average temperatures in each loop. The results of the sinusoidal insertion simulations in this work provide several insights into the frequency characteristics of the IES. First, for the thermal power output, there is a resonance frequency which peaks around 0.022 radians per second. For the electrical power and hydrogen production outputs, there is a small resonance peak at approximately 0.18 radians per second. Otherwise, the gain is highest at the lowest two frequency magnitudes (i.e., $10^{-4}$ to $10^{-2}$), decreases steadily across the middle two frequency magnitudes (i.e., $10^{-2}$ to $10^{0}$), and is minimized to near zero at the highest two frequency magnitudes (i.e., $10^{0}$ to $10^{2}$). The effect due to the mass of the SHX secondary side shows that a higher tertiary loop fluid mass decreases the peak thermal power gain but does not appreciably affect the thermal power phase. For the electrical power and hydrogen production, higher SHX mass decreases the frequency at which the gain begins to decrease, and increases the magnitude of the phase shift. Overall, the results show

that the mass of the IES dampens high frequency signals crossing the IES. The benefit of this phenomenon is that noise, possibly from cavitation or worn pumps, coming from one system in the IES will not appreciably affect the other systems. This paper is part of a wider NEUP project on the use of the MCFR in an IES. The IES dynamic model used here was developed previously within the NEUP project and is also being used to investigate the use of the MCFR in powering a high-performance computing data center.

# Chapter 4

# Molten Salt Reactor Loss of Flow Accident Analysis using the NERTHUS Dynamic Model

*This chapter has been conditionally accepted and published with reservations as an individual journal article by NSTOR. I am the primary author. The other author is Dr. Sandra Bogetic. I primarily wrote the entire paper. Dr. Bogetic helped review and improve the content of the paper. The only edit between the version presented here and that submitted to the journal is the removal of the abstract.*

## 4.1 Introduction

Molten-salt reactors (MSRs) are among advanced reactor concepts which have garnered increased interest in recent years. There are several MSRs in development by different companies and each design has a variety of fuel cycle characteristics. [89, Tab.1] The key characteristic of an MSR is that the primary coolant is a molten salt; generally an alkali-halide melt. [90] Specifically discussed in this work are MSR designs with the fuel melted and in a eutectic mixture with the salt. This mixture, referred to as fuel salt, circulates through the primary loop of the reactor. Circulating fuel salt affects the behavior of delayed neutron precursors and decay heat. [91] The advantage of using fuel salt is that the reactor can be safely operated at higher temperatures and lower pressures than conventional light water reactors (LWR). [92] Together, these aspects are what enable MSRs to boast enhanced efficiency and safety compared to LWRs. The ability to remove gaseous fission products from the fuel salt in an MSR also allows for the capability to perform load following more effectively than LWRs. [38] Further reading on the advantages of MSRs can be found elsewhere. [93, 94, 95]

The development of MSRs dates back to the Aircraft Reactor Experiment and subsequently the Molten-Salt Reactor Experiment (MSRE) in the 1960s. [96] The purpose of the MSRE was to be a means of developing and demonstrating new materials and technology. [61, 97] However, from then until recent years there has been less research performed on MSRs. Therefore, the operating experience and design of the MSRE has made it the most influential MSR design. As such, the MSRE's experience serves as the benchmark to compare other designs to. The design differences and limited operational experience of MSRs, in comparison to LWRs, leads to less familiarity with the types of accidents an MSR could experience and the manner in which issues would arise in such an event. An MSR can experience many of the same types of accidents as an LWR relating to the continued cooling of the fuel. [98] The primary difference is that fuel salt blurs the line between fuel and

coolant. Thus, for example, a loss of fuel salt in an MSR is not analogous to a loss of coolant in an LWR.

The purpose of this paper is to investigate the behavior of an MSR during various types of accidents relating to pump failures in each of the coolant loops of a generic MSR design. For the sake of learning, these pump failure scenarios were performed without any control rod movement or reactor trip. The only response is a steam generator feedwater pump trip sometime after the pump failure, as discussed further in the methods section. The simulations were performed in the NERTHUS dynamic model [11, 99] simulated in version R2022a of MATLAB-Simulink [100] (RRID:SCR_014744). As an open source alternate, a similar model is provided in OpenModelica. [101]

## 4.2 Methods

NERTHUS is a conceptual generic MSR design meant to be a useful tool for teaching and research on MSRs. The development of the NERTHUS model was conducted in a previous project. A thorough explanation of the model's methodology, specifications, and capabilities is available in previously published work. [11] The aspects of the design that have the most relevance in this work are the heat exchangers, once-through steam generator, decay heat tracking, fission product tracking, and pump trip coastdown. Some discussion on these components is thus included herein. The system components (*i.e.,* core, heat exchangers, and steam generator) are represented in the model as a group of nodes. Each node is a collection of time-dependent equations determining the energy flow and thus temperature in that portion of its respective component. The full nodalization of the heat transfer system in the NERTHUS dynamic model is shown in Figure 4.1. Heat from fission is only produced in the core nodes, whereas decay heat is produced in all nodes of the primary loop. Overall design parameters, including the three salts used in each of the loops, are displayed in Table 4.1.

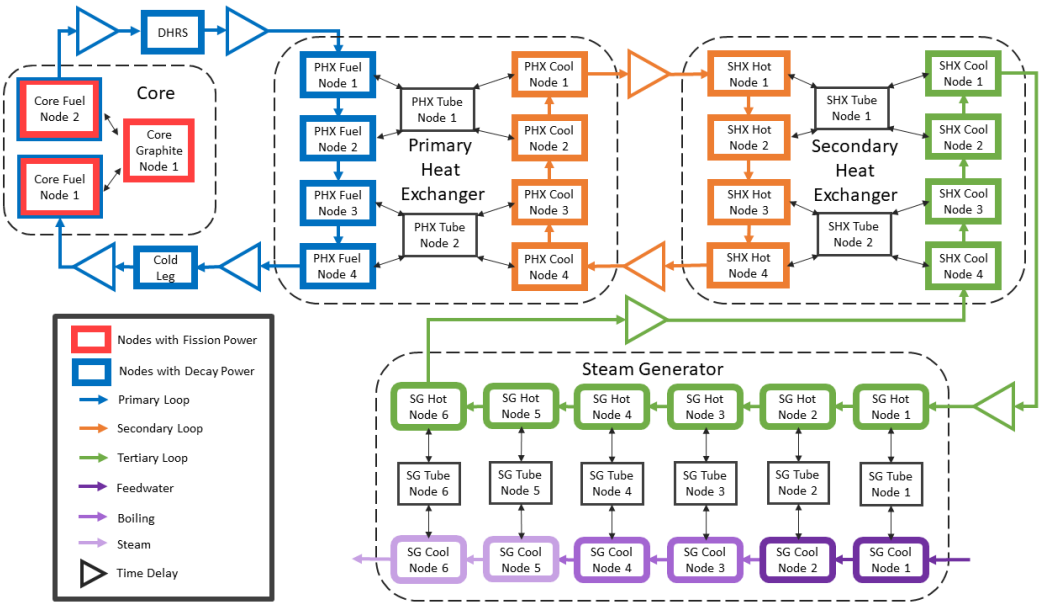


Figure 4.1: Nodalization of the NERTHUS dynamic model. The components of the model are the primary heat exchanger (PHX), secondary heat exchanger (SHX), and steam generator (SG). Also included in the primary loop is the decay heat removal system (DHRS).

Table 4.1: Overview of NERTHUS design parameters

| | |
|---|---|
| Thermal power | 557 MW |
| Average core inlet temperature | 610 C |
| Average core outlet temperature | 668 C |
| Fuel | Uranium |
| Uranium enrichment | 2.09% |
| Moderator | Graphite |
| Primary coolant | LiF-$BeF_2$-$ZrF_4$-$UF_4$ |
| Secondary Coolant | LiF-$BeF_2$ |
| Tertiary Coolant | Hitec salt [66] |
| $\beta$ [%] | 0.637773 |
| $\Lambda$ [$10^{-4}$ sec] | 7.1870 |
| $\alpha_f$ [pcm/K] | -7.0183 |
| $\alpha_g$ [pcm/K] | -3.2492 |

In which, $\beta$ is the total delayed neutron fraction, $\Lambda$ is the average neutron generation time, $\alpha_f$ is the fuel temperature coefficient of reactivity, and $\alpha_g$ is the moderator temperature coefficient of reactivity. These neutronics parameters are for the FLiBe (LiF-$BeF_2$-$ZrF_4$-$UF_4$) fuel salt at hot beginning of cycle and were determined using the NERTHUS neutronics model developed in Serpent. [11, 102] The neutronics parameters are necessary to determine the production of heat in the core and the reactivity response to changes in fuel and graphite temperature.

A pump failure was simulated by first running the model at nominal conditions until a set time when the desired pump is tripped. The amount of simulated time from start to trip was 2000 seconds, but for clarity, the time axes of all figures in this paper set zero seconds at the start of the first pump trip. There are four pumps in this model. The first three are for each loop (*i.e.,* primary, secondary, and tertiary), and the fourth is the feedwater to the secondary side of the steam generator, as shown in Figure 4.1. Realistically, a tripped pump does not immediately halt the flow of fluid in the loop. A pump has momentum in the flywheel and impeller, which continues to push the fluid as it slows down. Likewise, the fluid itself has momentum. Combined, this fact makes the phenomenon known as pump coastdown and the rate at which it occurs is specific to the design of the pump, the design of the piping system, and the

amount of momentum stored in the fluid itself. To realistically capture this behavior, the model utilizes an exponential decay equation to approximate the coastdown flow rate of a tripped pump. The equation for the fraction of flow in the loop is shown in Equation 4.1. [103, pg.3]

$$F_{flow} = (1 - N_{circ}) * e^{-K_{pump} * T_{trip}} + N_{circ} \tag{4.1}$$

Wherein, $F_{flow}$ is the flow fraction, $N_{circ}$ is the amount of flow due to natural circulation, $K_{pump}$ is the pump coastdown constant, and $T_{trip}$ is the time in seconds since the trip was initiated. Natural circulation in the system is due to the heat differential on each side of each loop. The exact rate of natural circulation is design specific and beyond the scope of this work. Towards the goal of determining generalities in MSR accident behavior agnostic to specific designs the natural circulation rate in each of the loops is assumed to be 5% of the nominal flow rate in that loop. Conversely, the pump coastdown constant used in this work was determined to be 0.092. This determination was made by fitting an exponential decay curve to the results from research performed at the Argonne National Lab. [104] [105] The resulting loop flow coastdown curve is shown in Figure 4.2.

There are three types of pump failures in this work. These three are a pump trip in the primary, secondary, and tertiary loops seen in Figure 4.1. A current limitation in the model is that when not enough heat is transferred to the secondary side of the once-through steam generator (OTSG), the model crashes. The reason for the crash is that the subcooled liquid, saturated boiling, and superheated steam domains are designed to have variable lengths in the OTSG to represent expected behavior in a physical system. When the lengths for the boiling and steam domains get too small, the OTSG loses pressure, which causes the steam temperature to plummet, and then results in a crash. To prevent a crash and to demonstrate the difference made by the timeliness of a response to the pump failure, the feedwater pump to the OTSG is also tripped in each transient. For the sake of comparison, the feedwater

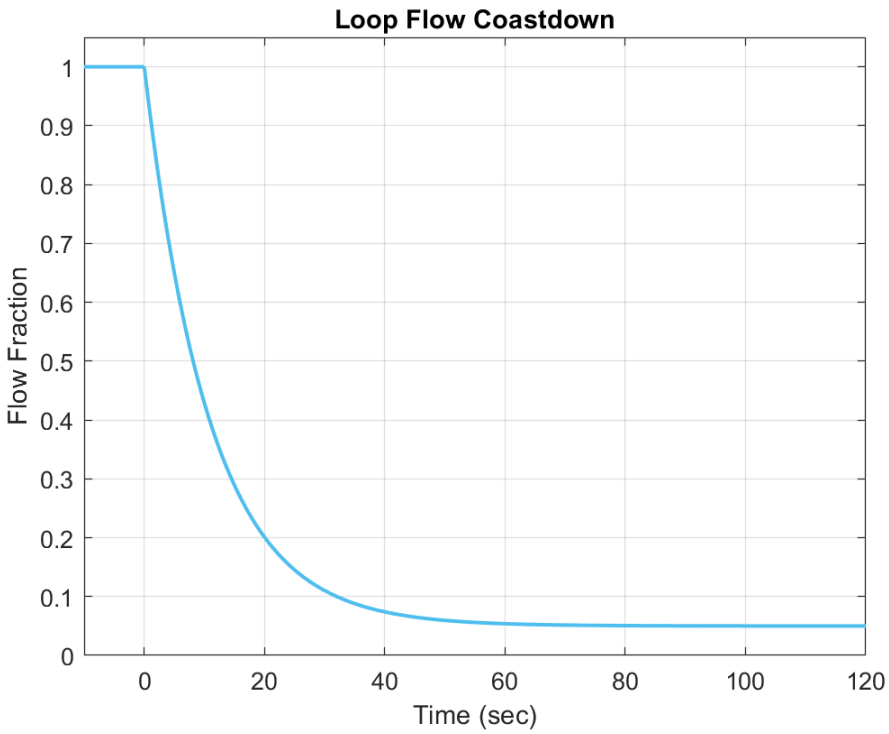


Figure 4.2: Flow rate decrease in the first two minutes after a pump trip

trips were performed at three time points for the primary and secondary loop trips: immediately with the pump failure, one minute after the pump failure, and four minutes after the pump failure. In the case of the tertiary loop, delaying the OTSG trip beyond approximately half a minute results in a loss of steam pressure and thus a crash in the model. Therefore, only an immediate OTSG trip is shown in this paper.

## 4.3 Results

This section is arranged by which loop is experiencing the pump failure: primary, secondary, and tertiary loop. The relevant dependent variables for each loss of flow scenario are the fission and decay thermal power, the temperatures on the hot and cold side of each loop, and the reactivity effects due to temperature and poisons. In all of the simulations there is no control rod movement. The only response to the pump failure is a trip to the once-through steam generator (OTSG) feedwater

pump. The justification for this response is that a pump failure in a loop causes a decrease in heat transferred through that loop which leads to a decrease in the temperatures of the loops downstream from the failure. If the OTSG feedwater flow rate is likewise decreased then the temperature of the fluids downstream from the failure should mostly hold steady. Meanwhile, the temperature of the fluids upstream from the failure will increase, which because of the negative reactivity coefficient due to temperature, the fission reaction rate will decrease even without control rod movement.

For the sake of brevity and clarity, not all possible results can be shown in this paper. Instead, several have been chosen to show the observed trends across the simulations. These results are the power and temperature outputs from a loss of flow in the primary, secondary, or tertiary loop. All data produced and used in this work is shared openly in a stable repository. [106]

## Primary loop pump trip

Firstly, the thermal power of the reactor before and during a primary pump failure with an immediate OTSG feedwater pump trip is shown in Figure 4.3. This figure is indicative of the inherent safety behavior associated with a negative temperature feedback coefficient.

Next, the loop temperatures for the same transient are shown in Figure 4.4. The key characteristic is that the temperature difference between and within each of the loops decreases with exception to the primary loop. In the moment before the primary pump is tripped, the temperature difference in the primary loop is 65.2. At 4000 seconds after the pump, the temperature difference in the primary loop is 59.2. Whereas, the temperature difference in the secondary loop starts at 40.9 and ends at 2.2.

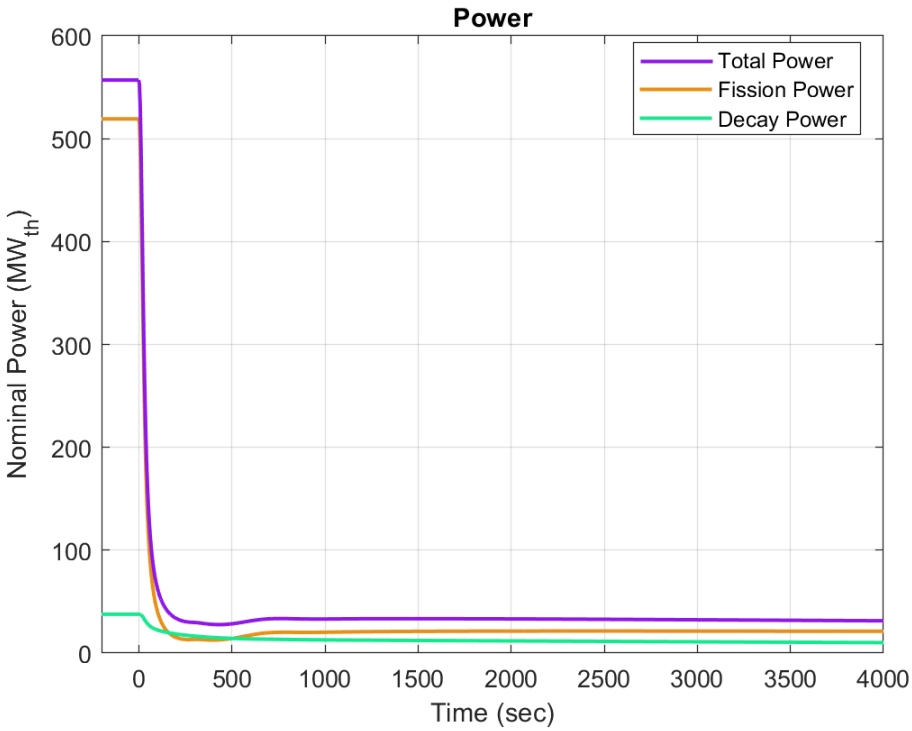


Figure 4.3: Thermal power produced by fission and decay within the reactor system after a trip in the primary coolant loop and a sixty second once-through steam generator trip response

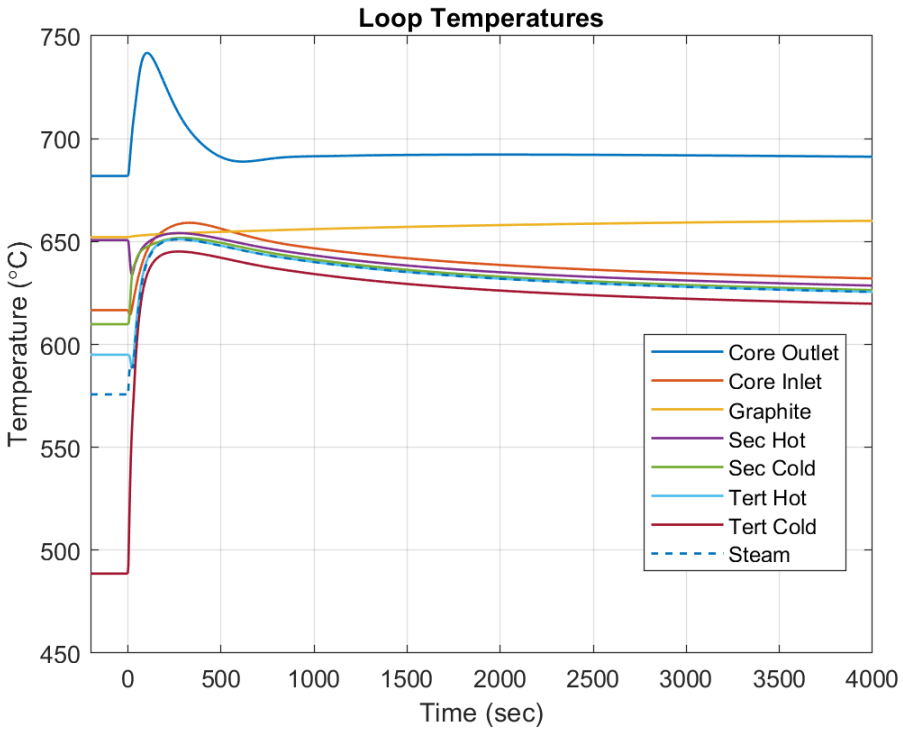


Figure 4.4: Temperatures on the hot and cold side of each loop, average graphite temperature, and steam outlet temperature after a trip in the primary coolant loop and an immediate once-through steam generator trip response. Wherein, the loops are the primary, secondary (Sec), and tertiary (Tert).

This behavior is to be expected, as a decrease in primary loop flow decreases the ability to transfer heat from the core to the rest of the system. The stop to the increase in temperature is due to the reactor power decrease due to that increase in temperature. The end result is a new steady state behavior where the loops downstream of the failure retain an increased temperature. The maximum core outlet temperature is reached at 103.7 seconds after the primary pump trip.

To begin to see the effects of delaying the OTSG trip response, the primary loop pump was again set to fail, but this time with a 60 second delay to the response. The resulting temperatures are shown in Figure 4.5. In which, the key characteristic is that the temperatures drop rapidly after the primary pump failure, with exception to the core outlet temperature, which rises. The temperature difference in the primary loop starts at 65.2 as is nominal, but ends at 59.9, which is nearly one degree higher than in the previous test. The maximum core outlet temperature is reached at 105.4 seconds after the primary pump trip. As the decrease in primary loop flow decreases the ability to transfer heat from the core to the rest of the system the OTSG continues to remove heat at nearly the same rate as before. The decrease in the temperatures is halted due to the trip to the OTSG's feedwater, which likewise decreases the rate of heat removal from the system. The end result is a new steady state behavior similar to the previous simulation.

To determine the effect due to delaying the OTSG trip response even further, the same primary pump failure was simulated, but with a 240 second delay before the OTSG trip. The resulting temperatures are displayed in Figure 4.6. Without the OTSG trip, the temperatures in the loops are allowed to decrease longer and thus reach a greater minimum. The minimum core inlet temperature reached is 468, which occurs at 296.1 seconds after the primary pump trip. This greater temperature minimum also means it takes longer for the temperature to rise and reach its new steady state level. Notably, the steady state level reached by the temperatures is approximately the same as in the previous transient.

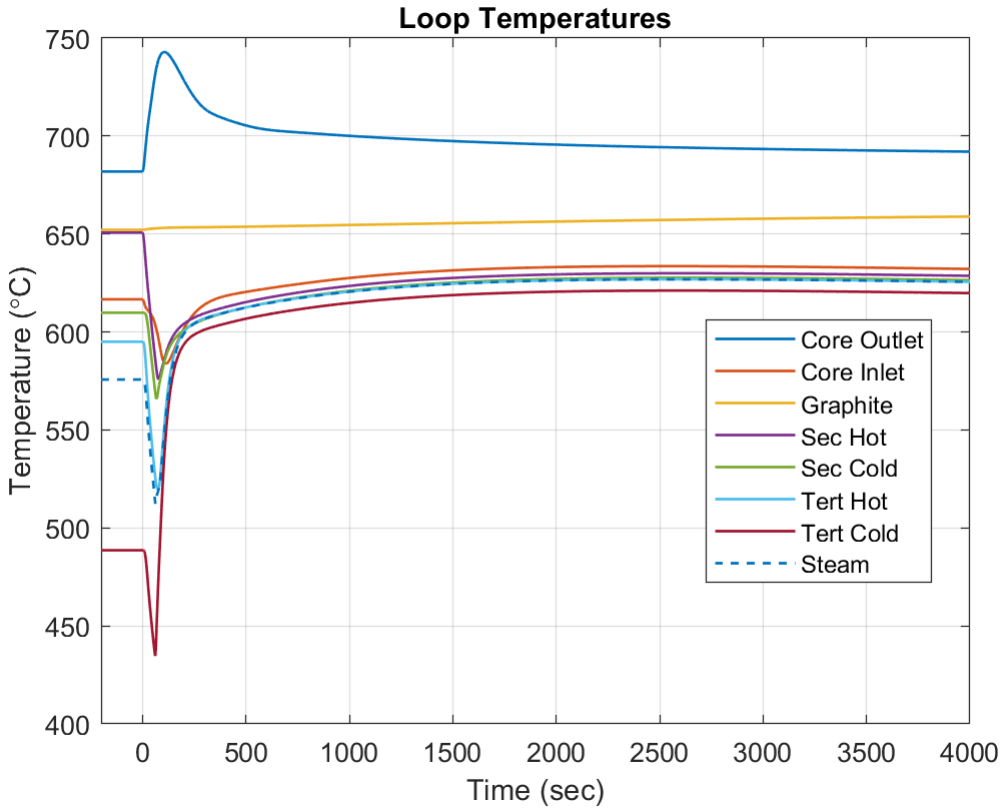


Figure 4.5: Temperatures on the hot and cold side of each loop, average graphite temperature, and steam outlet temperature after a trip in the primary coolant loop and a 60 second once-through steam generator trip response. Wherein, the loops are the primary, secondary (Sec), and tertiary (Tert).

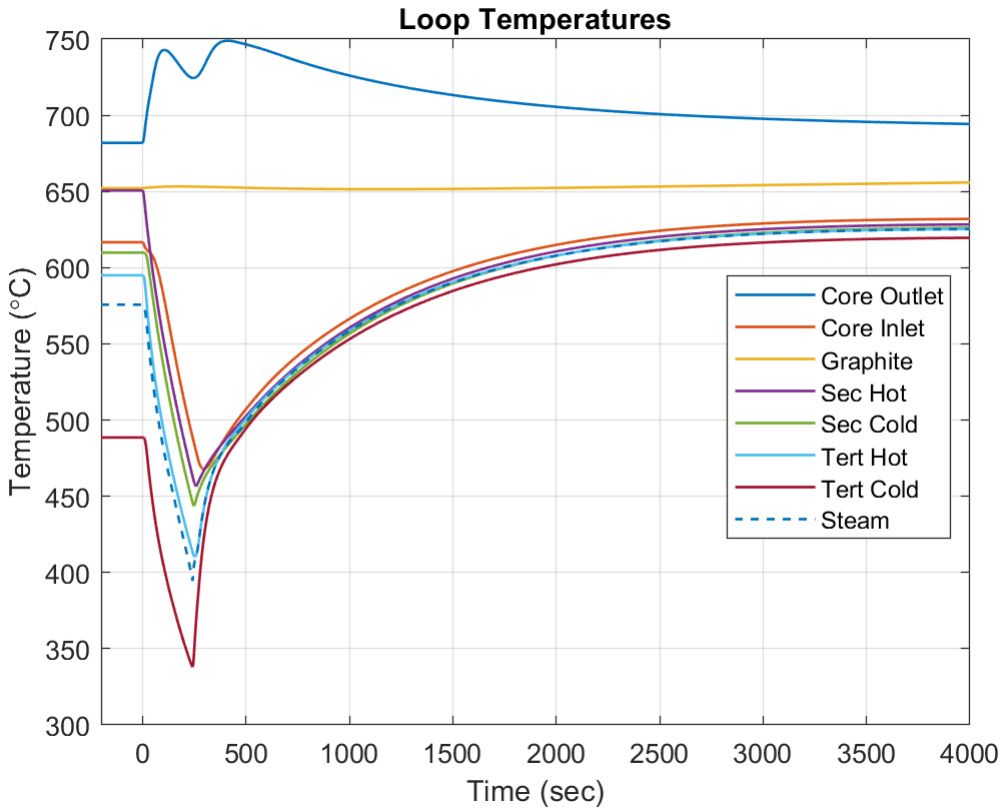


Figure 4.6: Temperatures on the hot and cold side of each loop, average graphite temperature, and steam outlet temperature after a trip in the primary coolant loop and a 240 second once-through steam generator trip response. Wherein, the loops are the primary, secondary (Sec), and tertiary (Tert).

A particularly relevant safety concern is the that if the salt temperatures get too low then they may begin to freeze, which can cause additional concerns that the model is unable to represent. For the salt in the secondary loop, the freezing temperature is approximately 460 . [107] Therefore, the salt in that loop would realistically be expected to be experiencing some freezing around the 250 second mark. The power response is not shown for every scenario due to them looking like what was previously discussed. However, for this last scenario, with a 240 second delayed OTSG trip response, the core inlet temperature dropped so low as to make a positive reactivity feedback. This phenomenon resulted in a fission power increase, as shown in Figure 4.7.

### 4.3.1 Secondary loop pump trip

In this set of transients, the secondary loop pump is the one that fails again with an accompanying OTSG trip at three different times. The resulting power output from a secondary loop pump failure with an immediate OTSG trip is shown in Figure 4.8. In which, the main difference is the fission power is suppressed to near zero until a power increase occurs at around 3200 seconds. The associated temperature outputs for each of the loops for that transient are shown in Figure 4.9.

The resulting temperature outputs for the secondary loop pump failure with a 60 second OTSG trip response is shown in Figure 4.10. As before, the trend of a decrease in loop temperatures before the OTSG trip can be seen. The temperatures then rise after the OTSG trip and settle at a new steady state with the largest temperature difference between adjacent regions being that of the hot side and cold side of the secondary loop. This phenomenon is to be expected due to it being the loop with the lowest flow rate and ability to transfer heat.

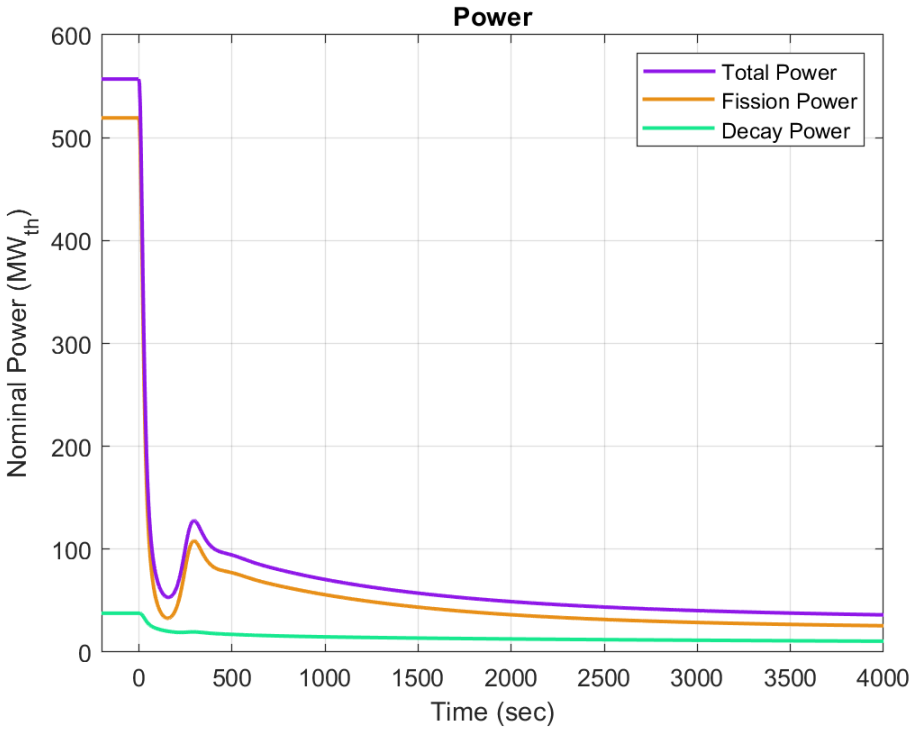


Figure 4.7: Thermal power produced by fission and decay within the reactor system after a trip in the primary coolant loop and a 240 second once-through steam generator trip response

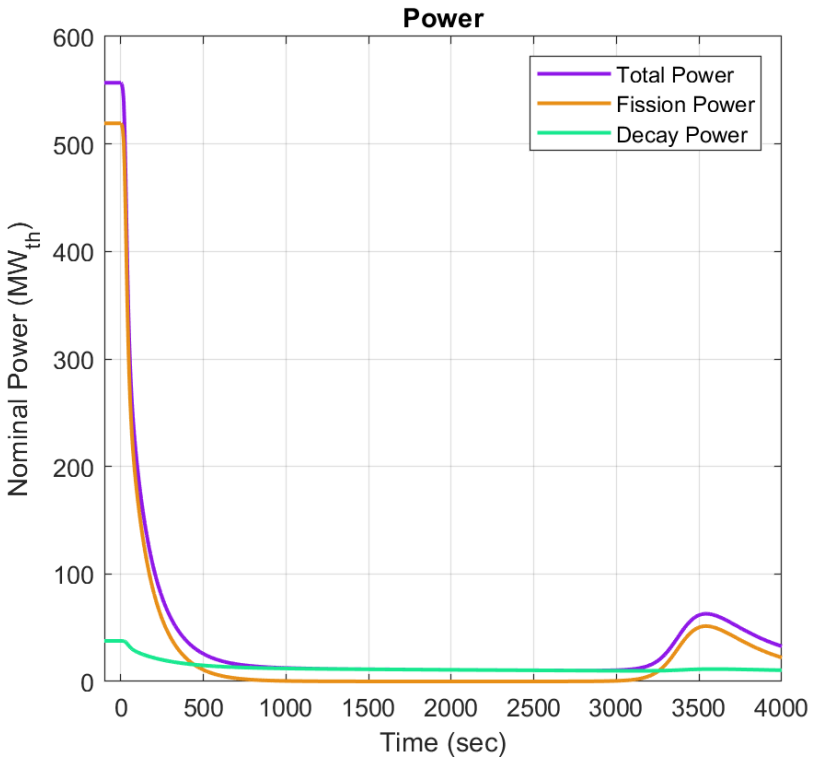


Figure 4.8: Thermal power produced by fission and decay within the reactor system after a trip in the secondary coolant loop and an immediate once-through steam generator trip response

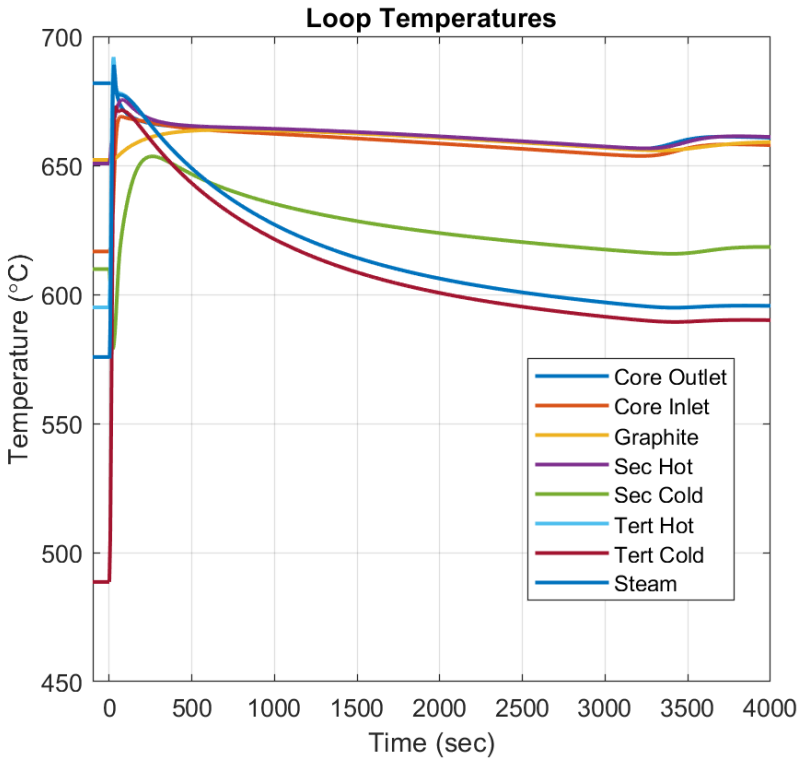


Figure 4.9: Temperatures on the hot and cold side of each loop, average graphite temperature, and steam outlet temperature after a trip in the secondary coolant loop and an immediate once-through steam generator trip response. Wherein, the loops are the primary, secondary (Sec), and tertiary (Tert).

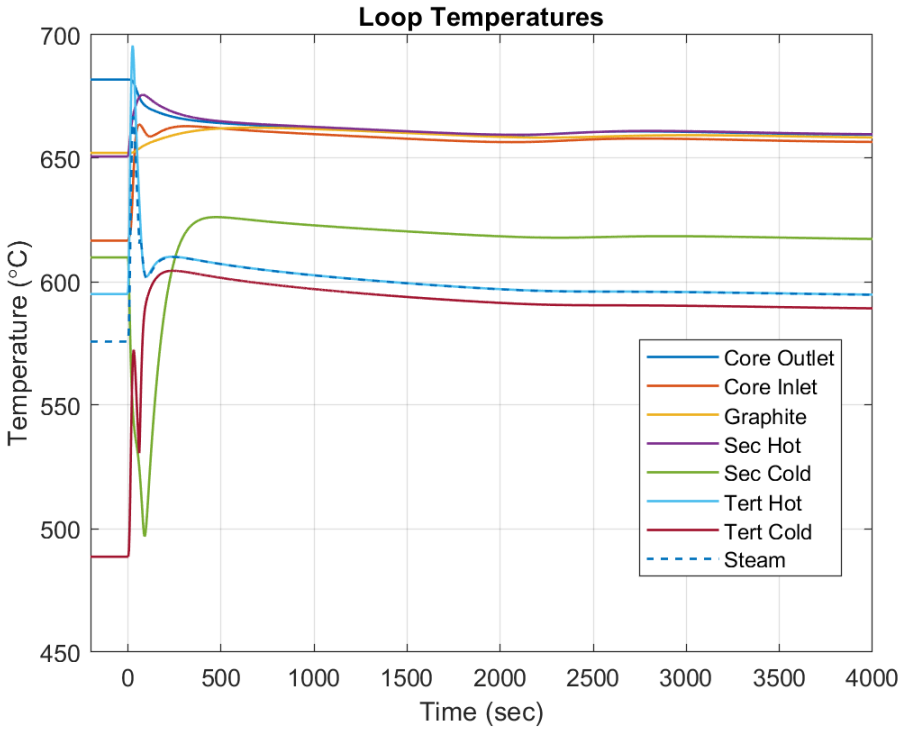


Figure 4.10: Temperatures on the hot and cold side of each loop, average graphite temperature, and steam outlet temperature after a trip in the secondary coolant loop and a 60 second once-through steam generator trip response. Wherein, the loops are the primary, secondary (Sec), and tertiary (Tert).

Finally, the temperature results of a secondary pump trip with a 240 second OTSG response are shown in Figure 4.11. Similar to with the comparison of 60 second to 240 second for the primary pump trip, it can be seen that the temperatures go much lower with a later OTSG response. In fact, the cold side of the secondary loop goes below the freezing temperature of the FLiBe coolant salt. However, the model does not know and cannot realistically portray that. The model currently cannot represent any phase change in the salt.

The issue of salt freezing in the pipes is a complicated topic due to the specific arrangement of pipes, whether it freezes from the pipeside inward or forms frozen particulates in the loop. Therefore, detailed salt freezing is beyond the scope of this paper. However, it is relevant to point out that the coolant salt in the secondary loop becomes an issue before the steam temperature does. For clarity, the steam outlet temperature becomes an issue if it drops below the saturated boiling temperature, and thus is not steam anymore. In comparing the primary pump trip scenarios to the secondary pump trip scenarios it becomes apparent that the secondary loop in this design is more sensitive to a pump failure than the primary loop is. As seen in Figure 4.12, the fuel salt temperature decreased enough to prevent the fission power from fully falling as in previous transients. Instead, the total thermal power of the reactor stops at approximately 34% of its pre-transient nominal value.

### 4.3.2 Tertiary loop pump trip

The final scenario is a pump failure in the tertiary loop with an immediate OTSG trip response. The resulting power output is shown in Figure 4.13 with the accompanying temperature output on Figure 4.14. As before the main temperature difference that forms is in the loop that suffered the pump failure; which in this instance is the tertiary loop. The relevance there is that with those temperatures decreasing, the steam temperature is at greater risk of decreasing to the point that the OTSG loses pressure and the model crashes.

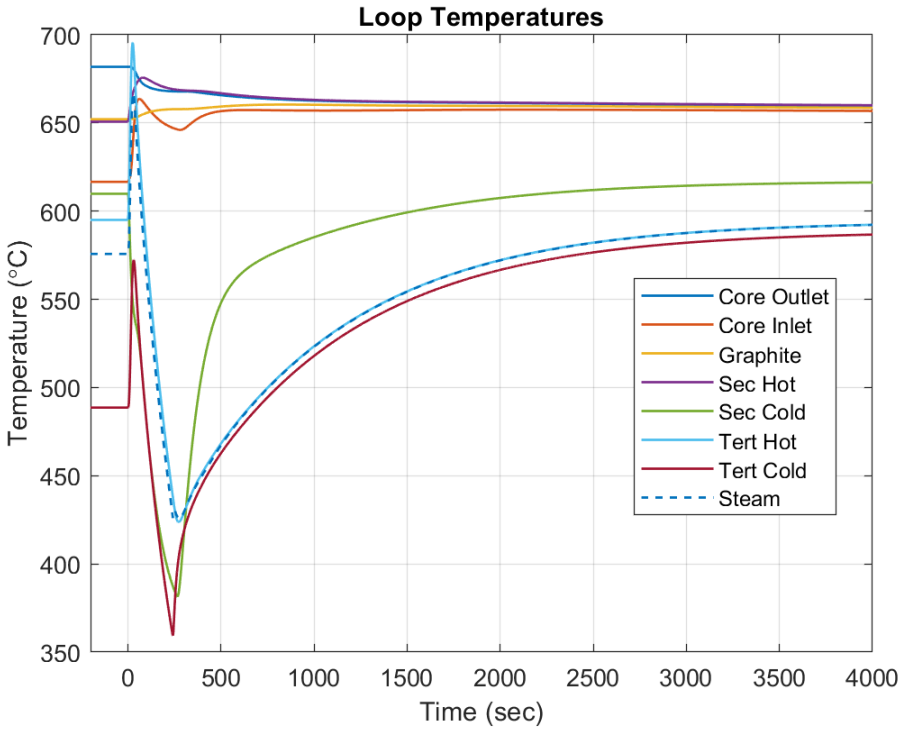


Figure 4.11: Temperatures on the hot and cold side of each loop, average graphite temperature, and steam outlet temperature after a trip in the secondary coolant loop and a 240 second once-through steam generator trip response. Wherein, the loops are the primary, secondary (Sec), and tertiary (Tert).

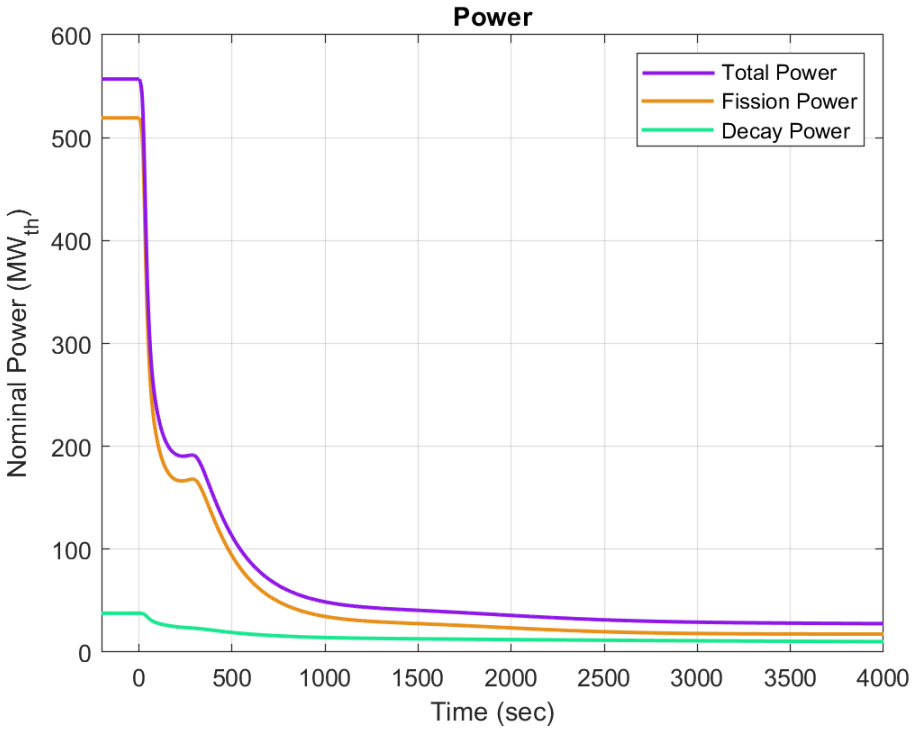


Figure 4.12: Thermal power produced by fission and decay within the reactor system after a trip in the secondary coolant loop and a 240 second once-through steam generator trip response

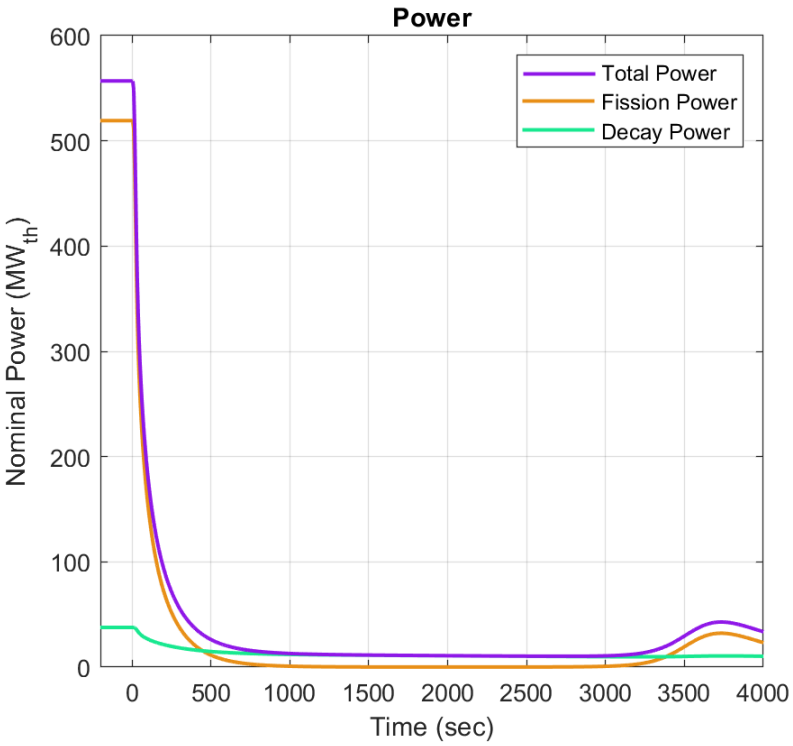


Figure 4.13: Thermal power produced by fission and decay within the reactor system after a trip in the tertiary coolant loop and an immediate once-through steam generator trip response

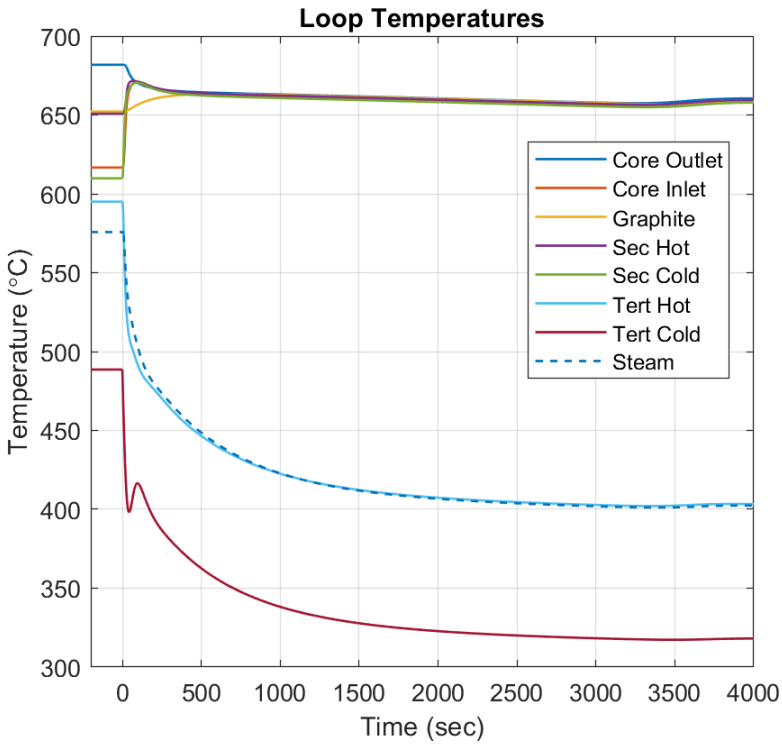


Figure 4.14: Temperatures on the hot and cold side of each loop, average graphite temperature, and steam outlet temperature after a trip in the secondary coolant loop and an immediate once-through steam generator trip response. Wherein, the loops are the primary, secondary (Sec), and tertiary (Tert).

The temperature minimum for the steam is 328°C due to its saturation temperature at that pressure. For this reason, the only results for the tertiary loop pump failure is that with the immediate OTSG trip response. Tests with a sixty second delay resulted in the model crashing. Further tests revealed that the maximum delay time before the OTSG loses pressure is around forty seconds. From these results, we see that the tertiary loop is even more sensitive to a loss of flow accident than the secondary loop. Combined with the fact that the secondary loop was more sensitive than the primary loop, it can be inferred that a pump failure farther than the core leads to more issues when the primary safety related concern is minimum temperatures.

## 4.4 Conclusion

In this paper, the behavior of a generic molten salt reactor (MSR) enduring pump failure in the primary and secondary loops is investigated along with different once-through steam generator (OTSG) response time. In these transients, there is no control rod movement and the only action taken is *via* the OTSG's feedwater flow rate. Future progress on this work will focus on greater functionality added to the dynamic model and with other types of accidents simulated too. These additional accidents include reactivity initiated accidents, loss of coolant accidents, and loss of heat sink accidents.

As MSRs are continued to be developed, there is importance in investigated the behavior of them under various conditions. The standard assumptions people familiar with light water reactors have do not always hold true due to the circulating fuel and the exotic coolants. In this way, there is value in educating others about it. The goal of the NERTHUS model is to serve as a tool for such a purpose and was used here in demonstration of that capability.

# Chapter 5

# Plutonium Signatures in Molten-Salt Reactor Off-Gas Tank and Safeguards Considerations

*This chapter has been submitted as an individual journal article. It is has been published in Volume 4, Issue 2 of the Journal of Nuclear Energy. The other authors are: Alex Wheeler, Jarod Richardson, Sandra Bogetic, Ondrej Chvala, and Steven E. Skutnik. Alex Wheeler and Jarod Richardson were both instrumental in the conceptual design of this research work. In particular, Jarod Richardson was the primary creator for the MSR neutronics model that was used to produce the data for this work. I curated and processed the data to produce the results shown in the work. I primarily wrote the entire paper with editting and revision support from the other authors. Ondrej Chvala and Steven E. Skutnik were the principal investigators for the project and helped shape the direction of the work. The only edit between the version presented here and that submitted to the journal is the removal of the abstract.*

## 5.1 Introduction

Nuclear reactors produce a tremendous amount of information in the form of radiation. The onus is on researchers to collect, decode, and make use of this information. One of the major goals of this work is utilizing this information to monitor the amount of special nuclear material in the system across operation for the purpose of safeguards. Safeguards for conventional nuclear reactors are currently performed with itemized accountancy techniques to maintain continuity of knowledge on the material at and between designated material balance areas. In these light water reactors, the solid fuel is easily itemized as individual fuel rods with serial numbers. In a molten salt reactor (MSR), the fuel is in a eutectic mixture with the salt. This fuel salt is fluid and flows all throughout the primary loop of the design. While it is possible to use traditional item accountancy techniques for MSR fuel salt before and after its use in the reactor, bulk accountancy techniques must be employed. [108] MSRs challenge the current international safeguards paradigm and encourage the development of new methods. Safeguards for MSRs can potentially utilize non-traditional information sources; such as from radiation within the offgas tank.

Presented in this paper is a conceptual technique to track plutonium buildup in a thermal spectrum molten salt reactor (MSR) through the analysis of radiation in the offgas tank. The goal of this novel technique is to observe the isotopes in the offgas tank and relate it to the fission reaction in the core via the ratio of isotopes with different fission yields for different fissile isotopes. This paper is a methodology and technique demonstration with the use of neutronics simulations. Offgas monitoring has the potential to become a valuable component and defense layer in an overall safeguards plan for an MSR. In an MSR, fission gasses can remain in solution or form bubbles in the liquid fuel salt. Of these fission products, noble gases will reliably form bubbles in the operating fluid. These bubbles can exit the fuel salt via an offgas tank. The relative production rates of these noble gas isotopes is dependent on the identity

of the atoms which underwent fission to produce them. Due to this relationship, the emissions from the offgas carry information on the amount of different fissile isotopes participating in the reaction in the core. Measurement of gamma rays is possible for both the fuel salt and offgas. However, measurement of beta particles is uniquely possible only in the offgas due to its gaseous state.

Analysis on the connected relationship between offgas and plutonium buildup was performed with simulations in Serpent. [102] The work included in this paper is an expansion of previous work on safeguards considerations for MSRs [108], plutonium signatures in MSRs [109], and also utilizes the NERTHUS neutronics model [11]. These techniques are potentially valuable safeguards and process monitoring tools for MSRs, and thus deserving further investigation.

MSRs are currently being developed by several companies (e.g., ThorCon Power, Kairos Power, TerraPower, Terrestrial Energy, Copenhagen Atomics, etc) and therefore require novel safeguards techniques. The unique and attractive potential of MSRs range from enhanced ability to perform load following [38], have improved passive safety, be used in non-electric energy markets requiring high temperatures, and more. Detailed discussion on the advantages of MSRs is available in further reading. [110, 94, 95]

## 5.2 Background

Analysis of the radiation emissions from an object or substance as a means to date it and investigate its composition is a well-understood technique in multiple fields. However, there are unique challenges that make this analysis more difficult in nuclear reactors in general, and molten salt reactors (MSR) in specific. Firstly, the material structure of the reactor shields any emitted alpha or beta radiation. Secondly, the bulk of gamma and neutron radiation that arrives at a nearby detector would likely overwhelm most detectors. Finally, the operating temperature of a reactor would make cooling any detector difficult or infeasible. These reasons form the basic

requirements for any detector to be useful. Despite these challenges, investigations have been conducted on the potential of spectroscopic and chemometric analysis on MSR offgas. [111, 112, 113] The methods performed in that research are focused on monitoring of iodine in the offgas via photon interactions. A similar project investigated using gamma spectroscopy on the offgas. [114] In this paper, we are the first to investigate the potential of using the beta radiation from several krypton and xenon isotopes in the offgas to conduct process monitoring for the purpose of safeguards. Multiphysics modeling methods have recently been used to simulate MSRs. [115] The MSR model used in this work is the NERTHUS neutronic model made in Serpent. [11]

Various noble gas isotopes of xenon and krypton are produced at differing rates from the fission of both uranium and plutonium. This fact has led to the monitoring of noble gas isotopes at nuclear reprocessing facilities to be a tool in the international safeguards toolkit for years. [116] The technique presented in this paper is similar in nature to these methods and represents a novel use specific to MSRs. Unique to MSRs, the special nuclear material and its products are in liquid state and circulating throughout the primary loop. As opposed to a reprocessing facility, the special nuclear material in an operating MSR is actively fissioning within the core and its products are decaying all throughout the loop. Due to the active fission reaction, there is a material evolution; which is discussed further in Section 5.4.2. Through research performed on the Molten-Salt Reactor Experiment (MSRE), much has been known for decades about the behavior and identity of fission products in an MSR. [55] A major opportunity exhibited by MSRs is that the noble gases will reliably form bubbles and exit the salt mixture into an offgas tank. [56] The foundation of the technique proposed in this paper is that these off-gases can be linked back to the active operation within the reactor and provide information on the production of plutonium.

Plutonium will be both produced and consumed within the reactor. Production occurs when $^{238}$U absorbs a neutron, becoming $^{239}$U and beta decaying into $^{239}$Np, then beta decaying again into $^{239}$Pu. Plutonium will also be consumed in the

reactor by absorbing a thermal neutron and undergoing fission. Further discussion of these phenomena and the overall evolution of the fuel with burnup is included in Section 5.4.2. The resulting relative participation of $^{239}$Pu and $^{235}$U in the fission reaction across fuel burnup is shown and discussed in Section 5.5.1.

### 5.2.1 Offgas Management and Analysis

The construction and operation of MSRs have multiple waste streams which take different forms. Discussion of these individual waste streams are available elsewhere in further reading. [117] Of particular relevance is the offgas stream. As an MSR is operated, gases form from within the fuel salt. These gases include reactive gases, residual halides, aerosols, noble gases, and others. Not all gases stay within the fuel salt, and whether they form bubbles or not is dependent on their solubility. Fission product solubility in operating fuel salt is a topic ripe for further research, and analysis has been performed on the topic in the days of the MSRE. [55, pg.54] For the sake of simplicity and applicability to general MSR designs, noble gases were chosen as the focus of this work. In particular, it has been shown that krypton and xenon will reliably bubble out of the mixture. [118, 119] It may be possible that other gases might prove to be useful with this method.

Both the MSRE and the Molten Salt Breeder Reactor (MSBR) [119, Fig.1] had an offgas tank in their design to manage gaseous waste streams for disposal. The primary purpose of the offgas tank was to act as an intermediate storage for the radioactive gases to cool off in before disposal. In this sense, the offgas system of an MSR is similar to the gas holdup system in conventional light water reactors (LWRs) to deal with their gaseous waste streams. These conventional LWRs, along with the MSRE and the MSBR, also utilize charcoal filtration systems in their designs to remove tritium from the gas. [120, pg.271] In particular, the MSBR planned to have offgas first held for two hours before being vented through particle traps then absorption into charcoal beds for forty-seven hours to remove most of the $^{135}$Xe. In their case, the gas was then

to be recycled back into the operating system via the bubble generators. [121, pg.7] MSRs reap many of the same benefits LWRs do from the use of an offgas system, with the significant additional benefit of the removal of gaseous fission products (primarily $^{135}$Xe) during operation. Depending on the location of the MSR plant, it may be required by domestic regulation to contain and/or separate out certain isotopes (ex: $^{85}$Kr). To comply, an offgas management system may be required. It is therefore reasonable to presume that most MSRs would include an offgas management system in their design. Research has already been conducted on what form an MSR offgas management system could be like in a commercial MSR power plant. [122, Fig.4] The example design given includes filtration and separation mechanisms, as well as recycling of helium in the system. There has also been additional research on the separation of Xe and Kr produced from a nuclear reactor using metal-organic frameworks. [123] Furthermore, the presence of an offgas tank receiving gases from an actively fissioning system allows for the ability to analyze the shorter lived (half-life in hours or less) gaseous fission products. This fact places MSRs in a privileged position in comparison to both conventional and advanced reactor designs. Further compounding this benefit is the fact that no intentional processing is needed to begin this analysis because it is done naturally by the MSR. In this sense, an MSR's offgas system is an ideal place to observe gaseous fission products.

In the MSRE, the offgas tank was placed downstream from the core in the pump tank, as shown in Figure 5.1. It operated by using a small pressurizer to maintain the gas pressure in the inlet of the tank and the tank itself. The liquid fuel salt would thus continue downstream through the primary loop, while some of the gases would bubble out into the offgas tank. The rate of bubbling out is dependent on the specific design of the mechanism and the flow rate of the primary fluid. A design with a more efficient offgas management system or with one located elsewhere in the primary loop may yield different specific results. However, the relative trends shown in this work can be expected to be representative of most liquid fuel MSR designs. Regardless of the amount of sparging in the system, the viscosity of the salt, or whatever else may

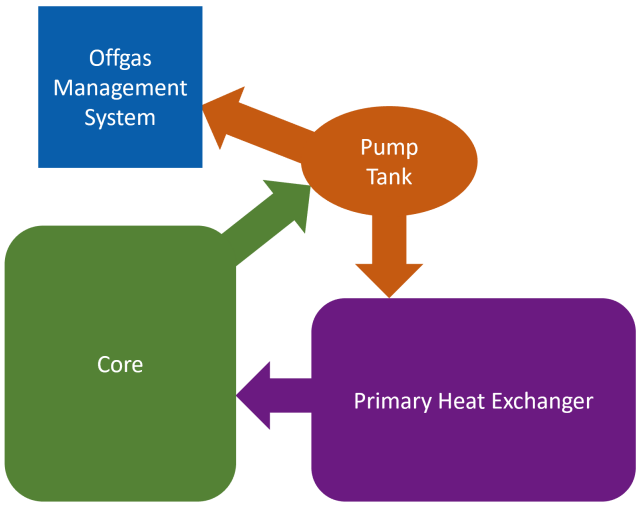


Figure 5.1: Arrangement of the offgas removal system in relation to the core and primary heat exchanger in the MSRE where arrows indicate flow channels. [2]

affect the overall rate of bubbling out, gases will be produced and exit to the offgas management system in relative amounts.

The major advantage of performing radiation detection at the offgas tank is that gases have very low self-shielding, which allows for the effective detection of beta particles emitted from them. Normally, with solid fuel or even liquid fuel salt, the fuel is self-shielding and blocks the beta particles from being detected. Therefore, one could place a detector within the offgas tank itself or within the entryway to the offgas tank, which is also filled with gas.

## 5.3 Process Monitoring using Offgas

Process monitoring is a familiar topic to those in nearly any industrial facility, whether nuclear or not. In general, it is the observation of a process for the purpose of maintaining it at a desired state. Such monitoring can take numerous forms in nuclear facilities and for various purposes ranging from control and safety, to plant performance and maintenance. Some examples of process monitoring in nuclear facilities are: vibration monitoring, acoustic monitoring, loose parts monitoring, reactor noise analysis, motor electrical signature analysis, and various modeling techniques. [124, pg.2] Process monitoring for the purpose of international safeguards is meant to increase both the timeliness of detection and the amount of information available to identify and verify a possible diversion. [125]

Within the topic of process monitoring is on-line monitoring. On-line monitoring (OLM) is process monitoring which is in situ, passive, and in service while the plant is operating. OLM is not necessarily real time, and whether an OLM technique is relatively real time or not is often determined by the data processing time. The offgas monitoring technique discussed in this paper can be used for OLM of the reactor and the fissile isotopes within it. While this method focuses on the observation of beta particles, other methods utilizing infrared spectroscopy have been investigated and

there is potential to incorporate sensor fusion into the design of an offgas management system. [126]

An MSR does not necessarily require an offgas tank to operate, but neglecting one in the design forfeits some of the advantages an MSR can boast. These advantages include the safeguards and process monitoring uses discussed in this paper, as well as enhanced load following and other capabilities. [38] Offgas tanks are analogous to a holdup tank system used to treat the gaseous waste stream from a conventional light water reactor. Therefore, a system tasked in removing and dealing with the offgas from an MSR can be expected in most designs. It can thus be leveraged as a signal source for monitoring.

The two forms of monitoring proposed in this paper are the tracking of special nuclear material for the purpose of safeguards, and tracking of isotopes relating to corrosion for the purpose of reactor health monitoring. Enhanced safeguards techniques are a major boon to utilities wishing to construct MSRs internationally where IAEA verification is required. Process monitoring is also a boon to utilities as it allows for data collection on reactor health, which can prevent costly repairs and maintenance downtime. [124]

### 5.3.1 Safeguards Relevance

Safeguards for molten salt reactors is seen as challenging due to the unique qualities involved in having multiple nuclear systems tightly coupled. [127] The fact that the fissile material is mixed throughout the fuel salt requires the use of bulk accountancy during operation. In addition to this difficulty, the fact that the fuel salt is a homogeneous mixture of actinides, salts, and fission products within a high temperature and actively fissioning system makes many bulk accountancy techniques, which are used in reprocessing and enrichment nuclear facilities, largely inapplicable.

The use of irradiated fuel measurements has long been a useful nondestructive assay technique for nuclear reactors. [128] However, these measurements have

historically been done on gamma ray emissions from the fission products. The important difference with MSR offgas monitoring is the utilization of beta particle emissions as a signal source. There are multiple ways in which the information gathered from the offgas tank can be utilized towards safeguards. The simplest means would be to observe for any disturbances in the trends predicted by the neutronics model of the reactor. A diversion of plutonium from the system would result in a noticeable and timely shift in the fission product ratios shown in Section 5.5.5. To test this method, diversion simulations can be tested to see how diversions of variable sizes and times would manifest in the fission product ratios. Further development can produce an inference model in which the fission product ratios are compared with the predicted results and used to determine the material unaccounted for (MUF).

A more advanced technique would be to develop a model which can compare multiple fission product ratios to each other to parse out a fission participation ratio for each of the fissile isotopes. Then, using the known thermal power production of the reactor and the average core flux at that time, determine the inventory of plutonium, uranium, and total fissile inventory. Use of this technique would still be some $\sigma$MUF due to measurement precision. This fact is not unique among bulk facilities, and it can be brought down to a minimum with proper development of the technique. MSRs would, however, have an opportunity which is unique among bulk accountancy facilities. This opportunity is the use of hybrid accounting techniques within the facility. Specifically, utilization of item accountancy techniques (serialization, weighing, etc) before and after use in the reactor. Discussion of this hybrid approach, its specifics, and advantages is found in previous work. [108]

### 5.3.2 System Monitoring

Beyond international safeguards, there are other beneficial reasons for utilities to observe and analyze the fission gases within their offgas tanks. Such benefits range from monitoring reactor health, with regard to corrosion products detection or the

halide potential of the fuel salt melt ("redox" monitoring), to improvements in the efficiency of the design. These are possible since the rate of gases entering the offgas is closely connected with certain isotopes of half-lives on the scale of minutes. Those isotopes can thus be used as indicators of reactor condition with only a slight lag.

In particular, as shown in Table 5.2, $^{139}$Xe has a short half-life of approximately forty seconds. Therefore, its equilibrium activity is closely dependent on recent events in the reactor, and it would be a useful isotope for power monitoring. There is also observation of $^{137}$Xe, which because of its balanced production between uranium and plutonium, could be used to determine the fission rate in the core.

Measurements related to iodine and xenon are also relevant to potential accident release doses [129]. This is an important research topic, since the iodine behavior in molten salts is not well understood. There are indications that iodine release correlates with the fluorine potential of the melt [130]. This would enable both monitoring of the salt's fluorine potential, and provide confidence for release estimates in MSR safety analyses. An exploration of MSR offgas monitoring potential for both operational and scientific purposes appears as an attractive field of future research.

## 5.4 Methodology

The results completed in this paper were performed by running a depletion simulation of a generic molten salt reactor in Serpent 2.1.32. [11] The MSR model, named NERTHUS, is open source and freely available on GitHub. It was inspired by and shares many similarities with ThorCon's TMSR-500 design. [131] The geometry described in the aforementioned paper is the same used in this project, as shown further in Section 5.4.1. The only difference as applies to the paper is the fuel cycle. Specifically changed in this work is: the reprocessing rate, refuel rate, refuel salt, and the initial salt. The initial salt has an enrichment of 2.1%, whereas the refuel salt has an enrichment of 19.75%. Refueling is done at a constant rate and with a method developed in previous work. [132] Reprocessing is performed within Serpent using the

Bateman equations and characterizing the change in the salt as constants in place of decay constants. Removal of the salt in reprocessing therefore acts similarly to decay. The simulation initially starts with hot fresh salt at beginning of cycle (BOC) and progresses with small-time steps to better capture the rapid changes. The time steps are set to progressively increase as the system reaches pseudo-steady state, up to a total simulated time of four years. In this way, the window of focus is set on the time of most rapid change.

The simulation tracks all of the fission products and their location at each step. In this way, there is a recording in the data file of all of the isotopes within the offgas tank as well as their masses, activity, thermal power, and atomic density for each step. The isotope tracking in the offgas tank is where the data came from for all of the figures used in the results section of this paper. The model considers the fuel salt to be homogeneous. There is no distinction within the model for in-core and out of core volume of fuel salt. Instead, to include the external fuel circulating through the core, the total volume of the fuel salt in the model is larger than that of just the in-core fuel salt. The data library used in the Serpent model is the ENDF/B-VII.0 Evaluated Nuclear Data Library. [58] In this work, the uncertainties of the cross sections and fission yields are neglected. The uncertainty of the fission yields of various isotopes may affect their usefulness as plutonium signatures. Determination of these effects is beyond the scope of this paper, but may be investigated in future work.

### 5.4.1 NERTHUS Neutronics Model

The model used in this work is the NERTHUS neutronics model. Detailed discussion on the development, methodology, and benchmarks of the model is explained in a previous paper. [11] For reader convenience, the most relevant information about the model is included here. A general overview of the MSR is shown in Table 5.1. The salt used in this work is FLiBe salt, which is is LiF-$BeF_2$-$UF_4$ (72-16-12 mole%) with the lithium depleted to 99.995% $^7$Li.

Table 5.1: NERTHUS Overview

| | |
|---|---|
| Thermal Power | 557 MW |
| Avg Core Inlet Temp | 617 °C |
| Avg Core Outlet Temp | 682 °C |
| Fuel | Uranium |
| Uranium Enrichment | 2.09% |
| Moderator | Graphite |
| Primary Fluid | LiF-$BeF_2$-$ZrF_4$-$UF_4$ |
| Secondary Fluid | LiF-$BeF_2$ |
| Tertiary Fluid | Hitec Salt [66] |
| Core Residency Time | 15 sec |
| PHX Residency Time | 11.6 sec |
| Out of Core Total Loop Time | 14.6 sec |

In the model, the core is comprised of 84 hexagonal prisms of graphite logs with fuel salt flowing between them. An example of one such prism is shown in Figure 5.2. Likewise, the full axial cross-section of the NERTHUS core is shown in Figure 5.3 and a longitudinal cross-section of the core is shown in Figure 5.4. There are only four materials used in the NERTHUS neutronics model. These materials are: the fuel salt, stainless steel, boron carbide, and graphite. The stainless steel used is SUS-316 with a density of 7.9 $\frac{g}{cm^3}$. The control rods are boron carbide with a density of 2.52 $\frac{g}{cm^3}$ and a boron enrichment of 20% $^{10}$B. The shield surrounding the reflector is made of 90% graphite and 10% boron carbine.

### 5.4.2 Fuel Evolution

Operation of a molten salt reactor (MSR) leads to a complex chemical environment due to the full array of fission products being present in "an exotic solvent at a cheerful red heat". [56, pg.161] Using the MSRE as an example, fresh fuel salt in a generic MSR would be something along the lines of LiF-$BeF_2$-$UF_4$ at a 72-16-12 mole% ratio, with the lithium depleted to 99.995% $^7$Li. Disregarding any slight contaminants from the production process or decays before the start of operation, fresh fuel salt would thus be comprised of six isotopes spread across four elements.

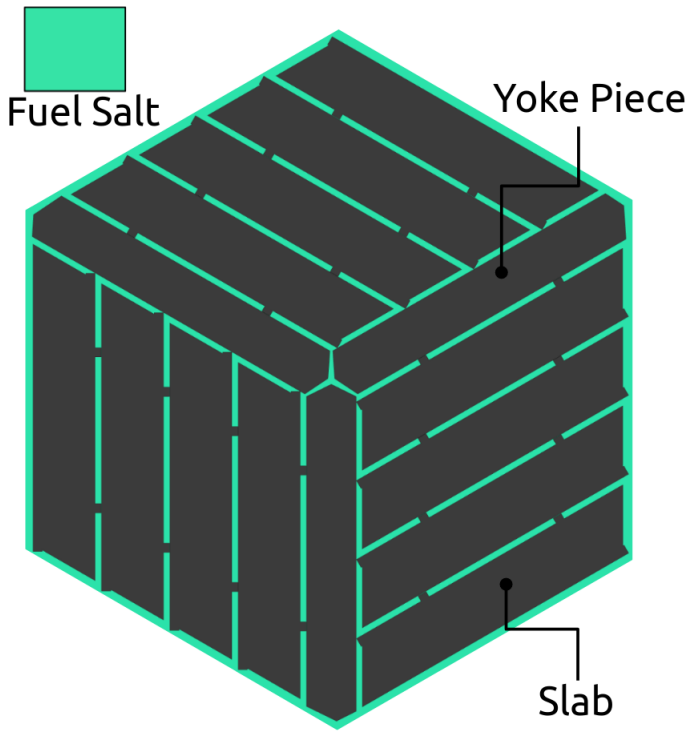


Figure 5.2: An axial cross-section of a log used in the NERTHUS reactor

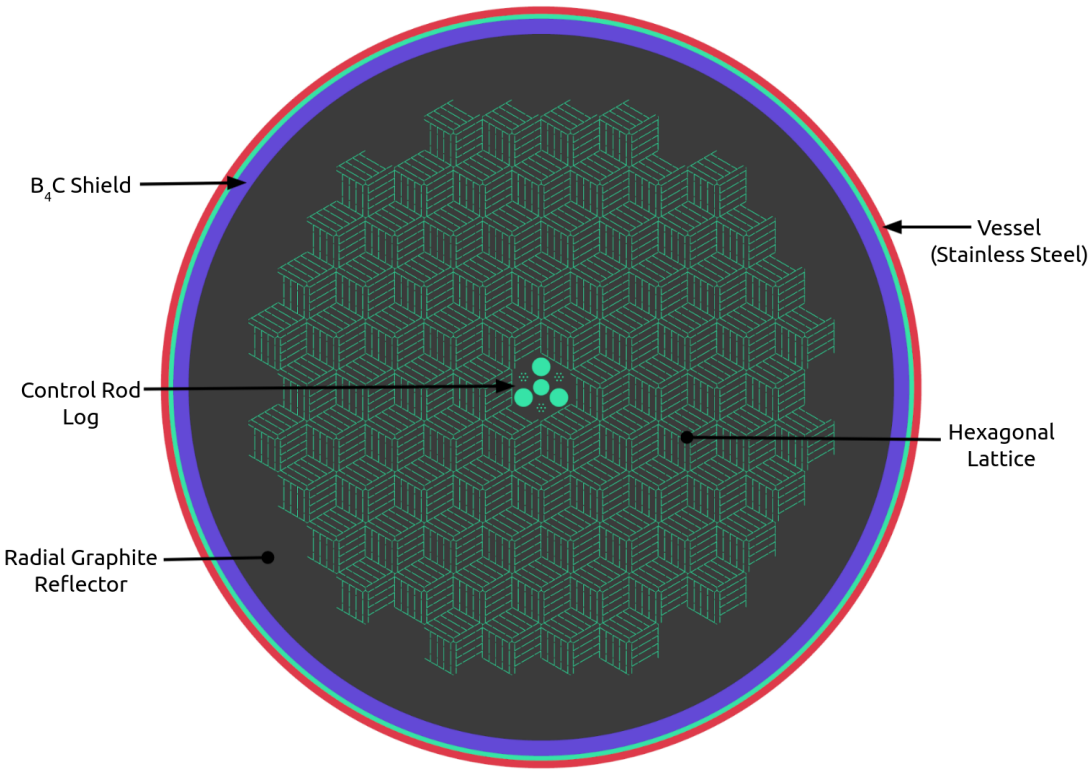


Figure 5.3: An axial cross-section of the NERTHUS core

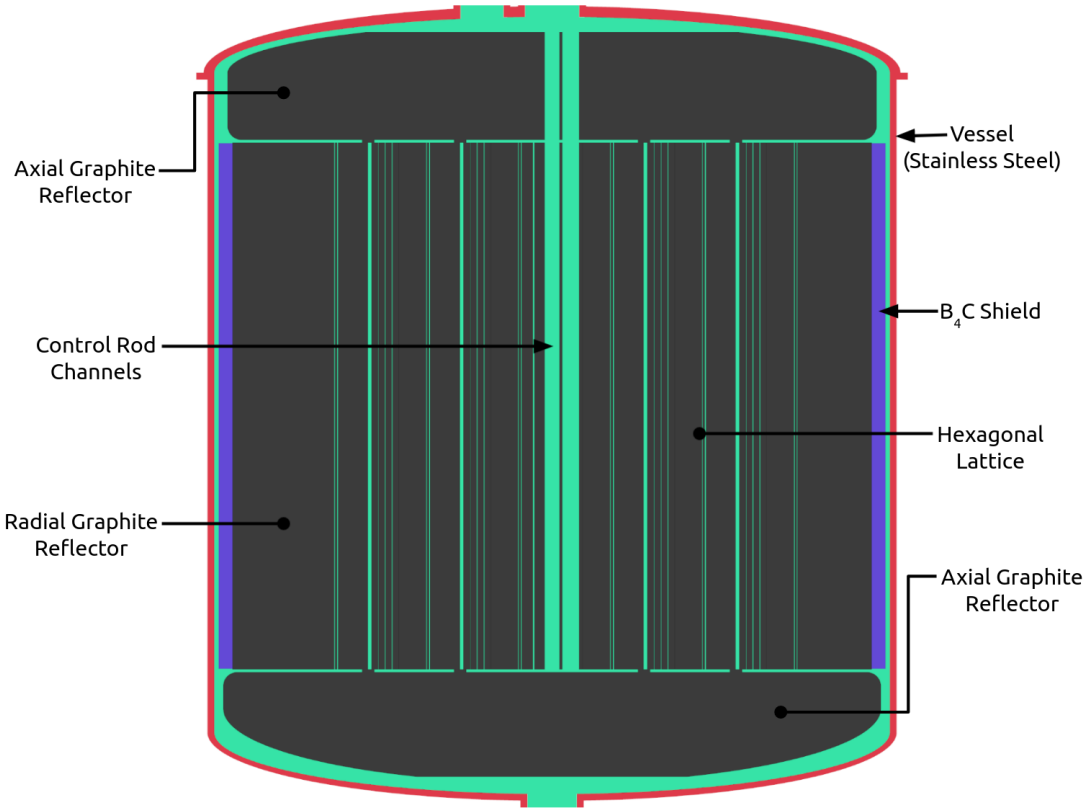


Figure 5.4: A longitudinal cross-section of the NERTHUS core with key features labeled

Specifically, the list of isotopes present would be: $^{6}$Li, $^{7}$Li, $^{9}$Be, $^{19}$F, $^{238}$U, and $^{235}$U. At the start of operation only uranium is fissioning and nearly all of it is $^{235}$U. As a result, a wide array of fission products are immediately introduced to the system. Many of these fission products then decay soon after, creating a cascade of various isotopes into the system. With the sustained neutron flux, many isotopes will absorb a neutron and many of those will have a subsequent decay reaction and change identity once again. Crucially, some of the large quantity of $^{238}$U will undergo this shift; absorbing a neutron, becoming $^{239}$U, beta decaying, becoming $^{239}$Np, beta decaying again, and becoming $^{239}$Pu. The first and most major influential of plutonium to arise is $^{239}$Pu, but as the concentration of it builds up, some $^{239}$Pu absorbs another neutron and becomes $^{240}$Pu. This process repeats up through the more massive plutonium isotopes. Of which, the most influential is $^{241}$Pu, which represents nearly all of the plutonium fission reactions not undergone by $^{239}$Pu. In this way, the variety of elements and isotopes goes from a few at the start of operation to a wide array of isotopes cascading down the periodic table. In general, there are three ways in which fission products can behave. They can either remain soluble in the salt, form insoluble metal particles which plate out, or form insoluble bubbles which exit through the offgas. [55, 56] Detailed discussion on the spent fuel salt from an MSR along with further information on how it can be used as sourdough in a new MSR can be found in previous work. [132]

The evolution of MSR fuel salt is further complicated through the process of online refueling. Online refueling is an optional design feature which is largely unique among most nuclear reactor designs. One such reactor design that utilized online refueling was the MSBR, which was intended to succeed the MSRE. [121] The process is performed by adding fresh fuel salt into the primary loop to raise the effective enrichment of the bulk fuel salt in the system. To better accomplish this goal, the refueling salt could be at a higher enrichment than the initial fuel salt was. If the enrichment of the initial fuel was 19.75% then the refueling salt would likely be the same. Conversely, some designs utilize a starting enrichment of approximately

4% for the initial bulk salt, then refuel with 19.75%. The variance between the enrichment of the initial and refueling salt is therefore design-dependent. In tandem, the rate of refueling is also design-dependent. Some designs refuel with small amounts very regularly (or even continuously [133, pg.20]) while others refuel a large amount infrequently, and again, some designs do not utilize online refueling at all. The act of online refueling has both rapid short-term effects on the fuel salt's isotopic variety and long-term effects on its overall evolution.

Each fissile isotope has a different probabilistic curve of possible fission products. These products each have a yield amount determined by experimental data. The constants used in this work are from ENDF-349. [57] As discussed in Section 5.4.2, different fissile isotopes are produced in the fuel over burnup. This phenomenon causes the ratio of these fissile isotopes' participation in fission to evolve over time. We can therefore expect the ratio of various fission products actively being produced to change over time as a function of the ratio of the fissile isotopes participating in the chain reactor.

The connection between fission product production ratio and fission participation ratio is the fission yield of the respective products. A product with a very similar fission yield between the participants would therefore be expected to stay mostly constant across burnup once it had reached its saturation point. Conversely, a product with a very different fission yield between the participants would be expected to have its concentration change over burnup to reflect the change in fissile ratio.

### 5.4.3 Isotopes of Interest

The variety of the fission products is vast. However, there are some considerations that help guide our selection of which isotopes to focus on. Firstly, the isotope must be entering the offgas tank. To do so, an isotope must reliably be a gas. Which fission products would leave the fuel salt solution to form bubbles in enough quantity is a difficult question. However, we can be reasonably assured that noble gases would

exit the solution and persist as a gas. [118, 119] Therefore, our selection of isotopes is primarily limited to noble gases.

Next, it is necessary for the isotopes to have a half-life low enough to have a measurable activity but high enough that most of the isotope has a chance to enter the tank. The MSRE had a loop transit time of 25.2 seconds. [120, pg.102] In the generic MSR model used in this paper, the loop transit time is 30.6 seconds. [11] In both of those cases, the loop transit time is the time in which a unit of fuel salt takes to complete a journey through the primary loop back to its starting point. In our model roughly half of that time (15 seconds) is core residency time. The offgas tank is presumed to be attached directly downstream from the core. Therefore, the core-offgas travel time is a fraction of the total loop transit time (likely only a few seconds) and we can be assured that most of an isotope would have a chance to enter the tank if its half-life is larger than the loop transit time.

Table 5.2 shows all of the isotopes of interest chosen for this paper. In the table, all presented fission yields are cumulative to better represent the aggregate amount of that isotope ending up in the offgas tank. However, use of cumulative fission yields is not without some underlying complexity. Specifically, iodine is a major source of xenon within the system. Therefore, some dragging time for the xenon population should be expected due to the half-lives of its respective parent isotopes being as long as twenty hours. This phenomenon is most apparent at the start of the fuel cycle, when the salt is clean and iodine is not yet at steady state. Of the chosen isotopes in table 5.2, $^{133}$Xe and $^{137}$Xe seem to have potential as a baseline case that has little difference in thermal neutron fission yield between $^{235}$U and $^{239}$Pu. In particular, $^{137}$Xe has such a small difference that could be used to approximate the number of fissions taking place in the core. Conversely, the krypton isotopes seem to be useful at parsing out the fission participation ratio between $^{235}$U and $^{239}$Pu. In this role, $^{89}$Kr seems to be the best by examination due to having the largest fission yield difference in both relative and absolute terms, as well as a high activity and high energy to release via beta decay.

Table 5.2: Half-lives, beta endpoint energies, and fission product yields for $^{235}$U, $^{239}$Pu, and $^{241}$Pu for the isotopes of interest.

| **Isotope** | **Half-Life** | $\mathbf{Q_\beta}$ (MeV) | $^{235}$U Yield | $^{239}$Pu Yield | $^{239}$Pu Ratio to $^{235}$U | $^{241}$Pu Yield | $^{241}$Pu Ratio to $^{235}$U |
|---|---|---|---|---|---|---|---|
| $^{87}$Kr | 76.30 m | 3.888 | 0.02558 | 0.00989 | 0.3866 | 0.00751 | 0.2936 |
| $^{88}$Kr | 169.5 m | 2.918 | 0.03553 | 0.01272 | 0.3580 | 0.00976 | 0.2747 |
| $^{89}$Kr | 3.150 m | 5.177 | 0.04511 | 0.01453 | 0.3221 | 0.01148 | 0.2545 |
| $^{133}$Xe | 5.280 d | 0.427 | 0.06700 | 0.07016 | 1.0472 | 0.06729 | 1.0043 |
| $^{137}$Xe | 3.818 m | 4.162 | 0.06129 | 0.06010 | 0.980 | 0.06558 | 1.0700 |
| $^{138}$Xe | 14.14 m | 2.915 | 0.06297 | 0.05171 | 0.8212 | 0.06258 | 0.9938 |
| $^{139}$Xe | 39.68 s | 5.057 | 0.05039 | 0.03086 | 0.6124 | 0.04921 | 0.9766 |

Not included in the table but still important to discussion is $^{135}$Xe, which is the most significant fission product poison. It can serve as a strong indicator of reactor power. The tracking of $^{135}$Xe and its effect on MSR load following has been investigated in previous work. [38]

## 5.5 Results

Presented in this section are the results from the simulation. Included in the results are: the buildup of $^{239}$Pu across burnup, in Section 5.5.1; the mass buildup of the isotopes of interest across burnup, in Section 5.5.2; the activity present in the offgas tank from each of the isotopes across burnup, in Section 5.5.3; and the relative activity from each of the isotopes along the buildup of $^{239}$Pu, in Section 5.5.4. The purpose of presenting these specific results is to demonstrate a clear connection between the presence of plutonium in the core and the amount of radiation of differing energies in the offgas tank.

### 5.5.1 Fission Participation Ratio

To determine expectations for the change in fission product production, we must first look at the change in fission participation in the system. Figure 5.5 shows the relative participation of the primary three fissile isotopes in the fission chain reaction. These isotopes in order of highest fission rate in the system to lowest are: $^{235}$U, $^{239}$Pu, and $^{241}$Pu. Included in the Pu total curve are all plutonium isotopes undergoing fission in the system. It can be considered that there are three time periods of discussion separated by the two plutonium isotopes reaching steady state. The first period goes from the beginning of cycle to when $^{239}$Pu reaches its maximum fission participation at approximately 400 days. This period starts with only $^{235}$U undergoing fission, but as $^{239}$Pu is transmuted within the system, it begins to increasingly participate in fission.

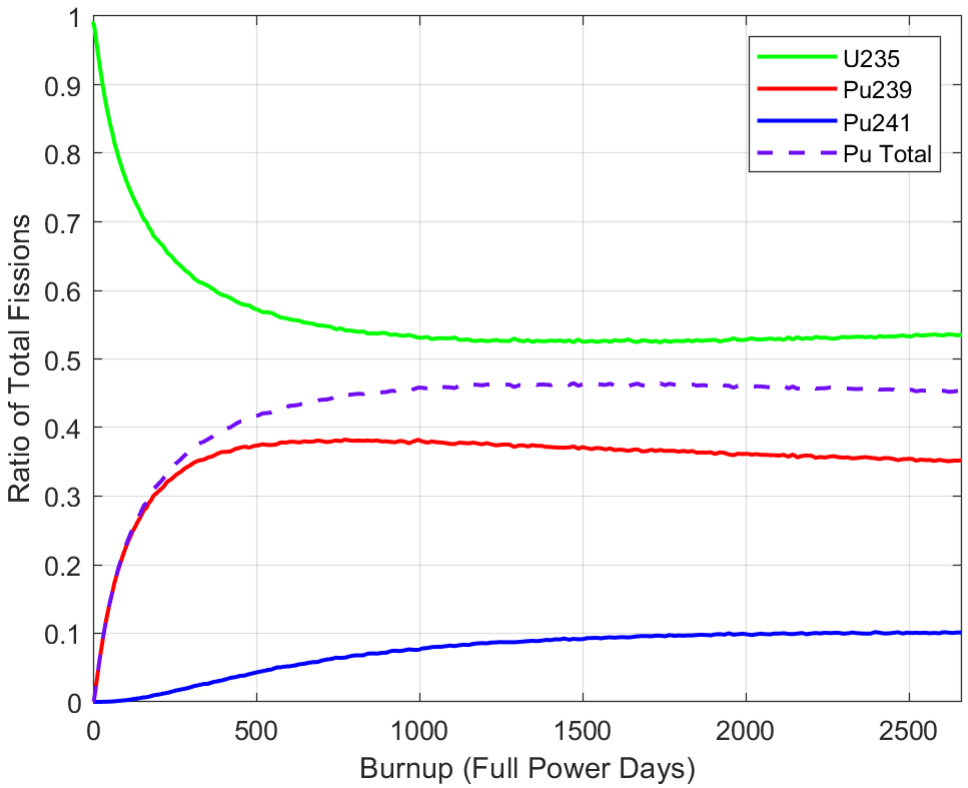


Figure 5.5: Fission participation ratio of major fissile isotopes in the system across burnup when starting with fresh fuel salt. Due to starting with fresh fuel, the most rapid change occurs near the beginning of cycle.

During this time, $^{241}$Pu is also being produced, albeit at a slower rate. It can be seen that $^{239}$Pu reaches saturation nearly 1,000 days sooner than $^{241}$Pu. However, as seen in Table 5.2, $^{241}$Pu has different fission product yields than $^{239}$Pu, which indicates a change in production of those isotopes should be expected across burnup.

The only fissile isotope in the reactor at the beginning of cycle is $^{235}$U. The production of other fissile isotopes is due to transmutation associated with burnup of the fuel. The relative amount of production is dependent on design (i.e. breeder vs burner), but the production method is the same. In any thermal reactor with $^{238}$U there will be neutron absorptions in $^{238}$U, which turns it into $^{239}$U. From there, $^{239}$U can decay into $^{239}$Np which can then decay into $^{239}$Pu, a fissile isotope. Therefore, as the reactor is operated, $^{239}$Pu will be produced. We see this in the results as a shift in the Pu/U fission ratio within the first 500 full power days of burnup. The amount of $^{241}$Pu is dependent on and will always remain a fraction of $^{239}$Pu. This fact is due to $^{241}$Pu being produced by the absorption of a neutron in $^{239}$Pu turning it into $^{240}$Pu and then a subsequent neutron absorption. These results are in agreement with previous research on the signature of plutonium in a MSR. [109]

### 5.5.2 Mass Buildup

The mass buildup of each of the isotopes in the offgas tank provides some additional information necessary to make sense of the later results. Figure 5.6 shows the masses of the krypton isotopes of interest ($^{87}$Kr, $^{88}$Kr, and $^{89}$Kr) across burnup and normalized to their maximum value. Likewise, Figure 5.7 shows the masses of the xenon isotopes of interest ($^{133}$Xe, $^{137}$Xe, $^{138}$Xe, and $^{139}$Xe). The normalization was done to more clearly show the relative difference between the isotopes. The maximum mass of the isotopes is shown further on. In all cases, excluding $^{133}$Xe, the isotope reaches its maximum mass quickly in a matter of hours within the first day of operation. Conversely, $^{133}$Xe does not reach its maximum mass until approximately 700 days.

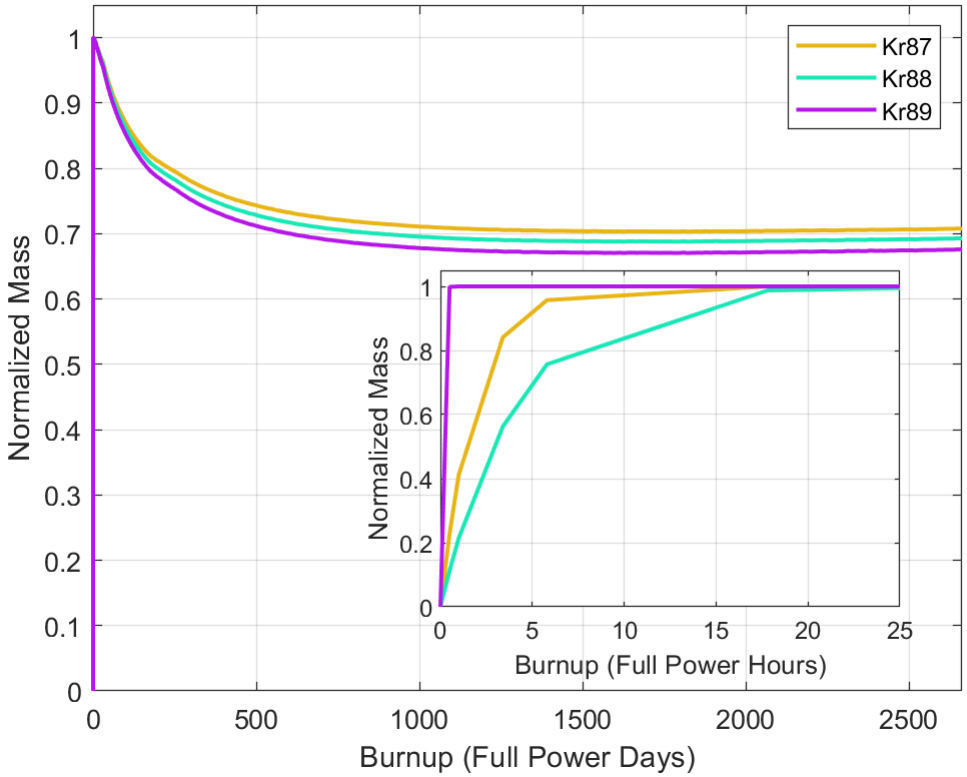


Figure 5.6: The masses of the three krypton isotopes of interest across burnup. They are displayed relative to their maximum mass for better comparison. All three reach their maximum mass within 24 full power hours.

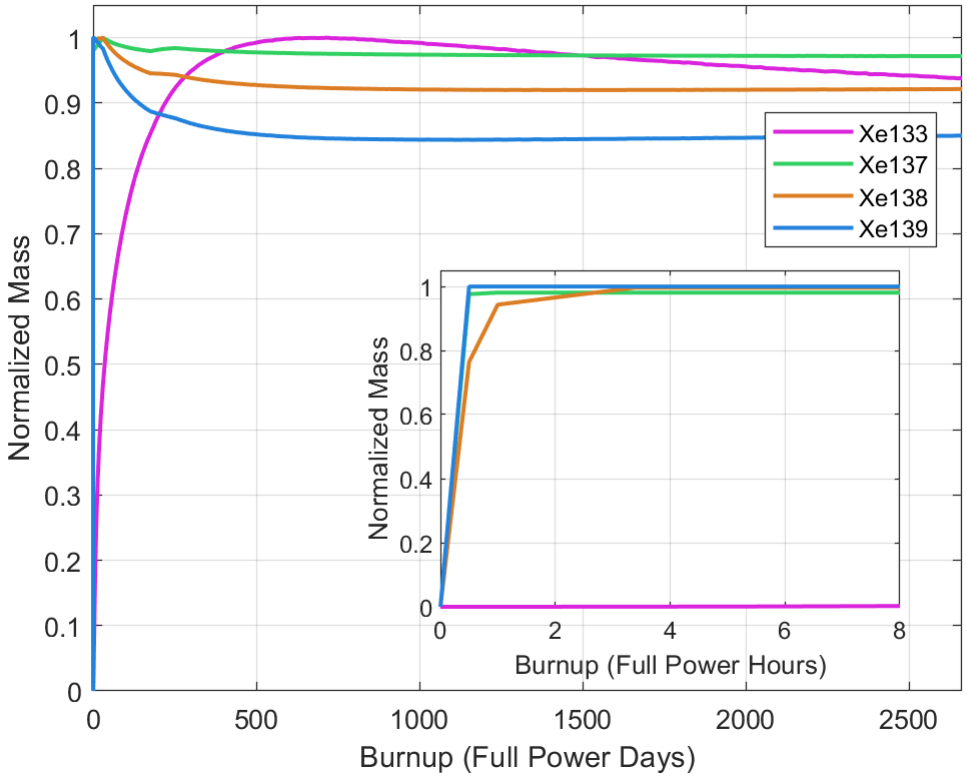


Figure 5.7: The masses of the four xenon isotopes of interest across burnup. They are displayed relative to their maximum mass for better comparison. With exception to $^{133}$Xe, all reach their maximum mass within 24 full power hours.

The reason for this delay is that the half-life of $^{133}$Xe is on the scale of days, whereas the others are on the scale of minutes or seconds, as shown in Table 5.2. As expected, it can be seen that the inverse is also true: the isotopes with the shortest half-lives reach their maximum values the quickest. With all the isotopes, after the maximum mass has been reached, the mass of the isotope within the tank decreases in connection with the changing fission participation.

In both figures, the insets have sharp changes due to the size of the time steps used in the simulation. Similarly, there is a non-physical disturbance in the data at around 200 full power days due to the size of the time step changing there as well. In both cases, this disturbance is an artifact of the simulation process and not a physical phenomenon. The data could be improved with increased computational time involved with smaller time steps nearer to the beginning of the cycle. However, for our discussion here, the important aspect is that the isotopes are shown to quickly reach their maximum values (within 24 hours) after the beginning of cycle with fresh fuel salt.

The maximum mass of each of the seven isotopes of interest is shown in Table 5.3. An astute reader will quickly see why it was necessary to show the mass buildup of the isotopes relative to their maximum values. To be clear, these masses are the amount within the offgas tank. The rate of production is comparatively closer between the isotopes than are their half-lives, leading to stark differences in maximum mass. Therefore, as one would expect, the isotope with the largest half-life would have the largest mass, and vice versa. It is for this reason that the maximum mass of $^{139}$Xe is so small in comparison to the others.

An important consideration is that the mass of the isotopes in the offgas tank is not one-to-one representative of the activity of those isotopes. As we will see with the activity results, most of the activity from these isotopes is not from the mass which has already been accrued into the tank, but from the mass that is actively entering the tank.

Table 5.3: The maximum mass of each isotope of interest within the offgas management system across burnup.

| Isotope | Maximum Mass (g) |
|---|---|
| $^{87}$Kr | 0.3864 |
| $^{88}$Kr | 1.2833 |
| $^{89}$Kr | 0.0290 |
| $^{133}$Xe | 13.8307 |
| $^{137}$Xe | 0.0752 |
| $^{138}$Xe | 0.2977 |
| $^{139}$Xe | 0.0085 |

Therefore, tracking the mass of the isotopes of interest in the offgas tank is indicative of its history, whereas tracking the activity is indicative of the present state of the fission reaction in the core. Also, this phenomenon suggests that the offgas tank might not need to be particularly large.

### 5.5.3 Activity

The activity of each of the isotopes of interest is where the results become particularly relevant. This importance is due to activity being the source of the signal which would be seen by the detectors. As shown previously, the mass of the isotopes in the offgas tank is not large ($<$16 g) due to their short half-lives. However, as shown in Figure 5.8, the maximum activity of the isotopes is comparatively large. For reference, $10^{17}$ Bq is equal to roughly 2.7 million Curie. The offgas tank is therefore quite hot, radioactively speaking, and there is plenty of a signal to measure. If anything, the intensity of the radiation would require special considerations for the detector. However, specific design of the detector is beyond the scope of this paper and would likely require a further research project on its own. The isotopes of interest chosen for this work have particular usefulness for beta spectroscopy due to the array of different energies they have, as shown in Table 5.2.

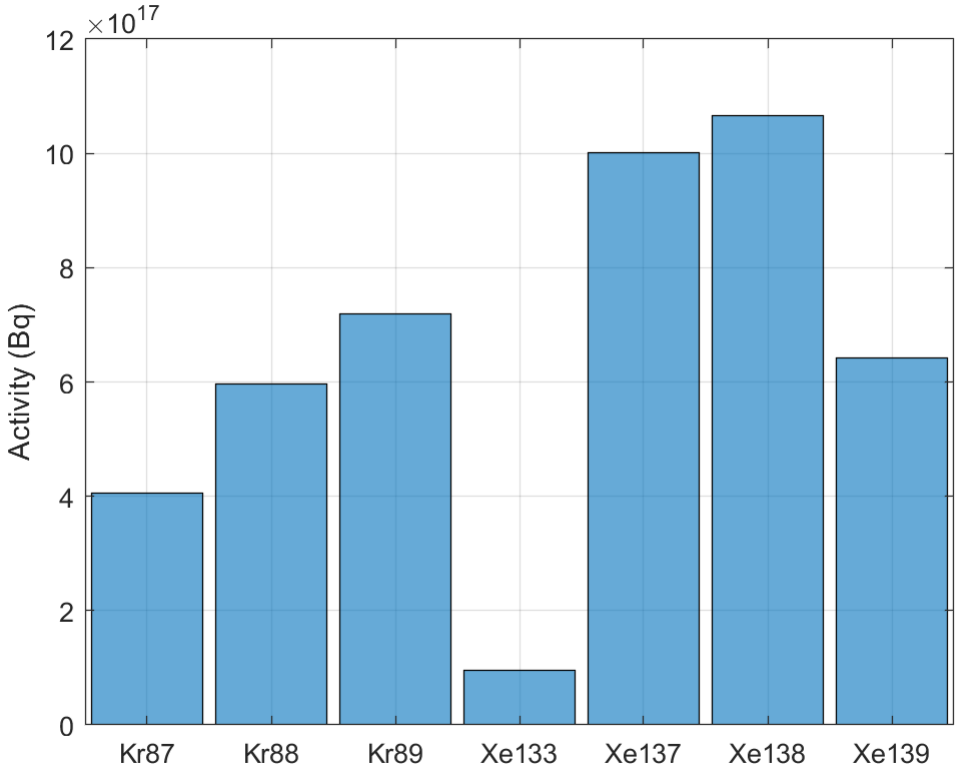


Figure 5.8: The maximum activity of each of the isotopes of interest within the offgas management system across burnup. Despite reaching the largest maximum mass, $^{133}$Xe has the smallest maximum activity.

There are two pairs of isotopes which may lead to overlapping signal: $^{88}$Kr and $^{138}$Xe, which both have a decay energy of approximately 2.92 MeV; and $^{89}$Kr and $^{139}$Xe, which have a decay energy of 5.177 MeV and 5.057 MeV, respectively. For that reason, isotope pairs must be chosen that have both a difference in fission yield and decay energy, such as the ones shown in Section 5.5.5.

The activity in the offgas tank from each of the krypton and xenon isotopes across the cycle is shown in Figures 5.9 and 5.10, respectively. As discussed, all of the isotopes, excluding $^{133}$Xe, reach their respective maximums relatively quickly. However, despite $^{133}$Xe requiring nearly 700 full power days to reach its maximum mass, it only took approximately 200 full power days to reach its activity saturation. This phenomenon is further indicative of the fact that most of the activity observed is from atoms that were recently produced from fission reactions.

### 5.5.4 Activity Relationship to Fission Participation

Each of the isotopes of interest have a relative shift in steady state activity across burnup due to the evolution of fission participation. This shift in relative activity as a function of fission participation ratio is shown in Figure 5.11. In the figure, the x-axis is the ratio of all plutonium fissions to all uranium fissions, discussed in Section 5.5.1. The isotope activities are normalized to their respective maximums and are the same results discussed in Section 5.5.3. In this way, by comparing normalized activity over time to fission participation ratio over time, the time variable is canceled out and the resulting relationship of isotope activity to fission participation is made clear.

At the highest Pu/U ratios in Figure 5.11, the activity curves of all of the isotopes loops around and forms a downward tail; with exclusion of $^{139}$Xe, which has an upward tail. The tails are due to the amount of plutonium reacting in the system decreasing slightly. This decrease makes the same Pu/U fission participation ratio correspond to two different burnup values.

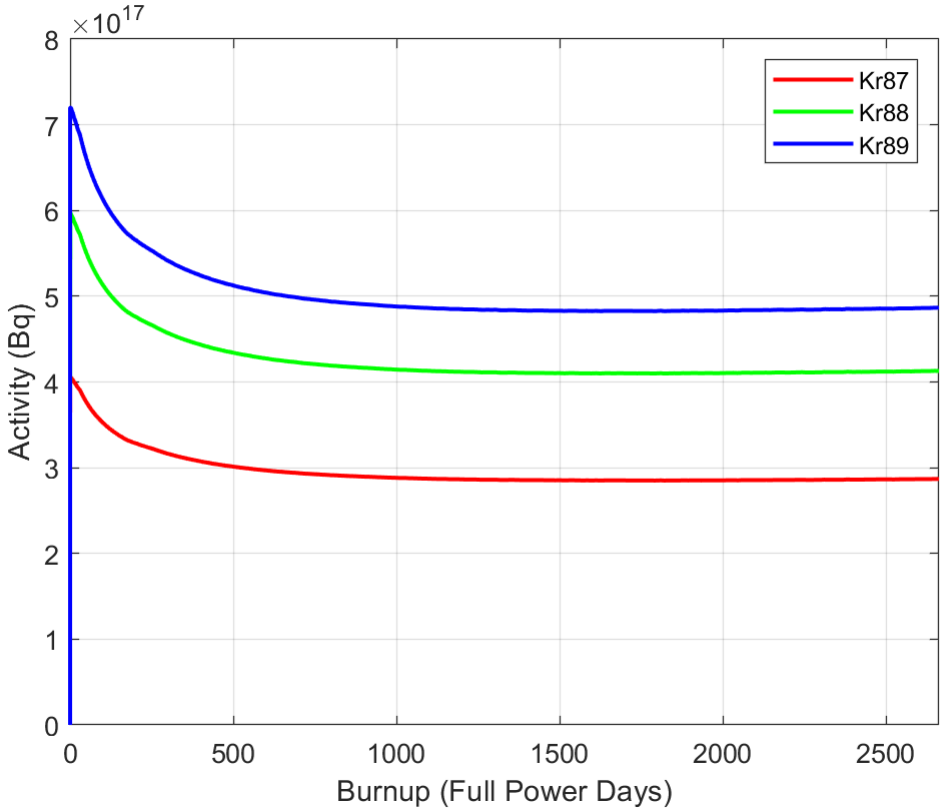


Figure 5.9: The activity of the three krypton isotopes of interest within the offgas management system across burnup.

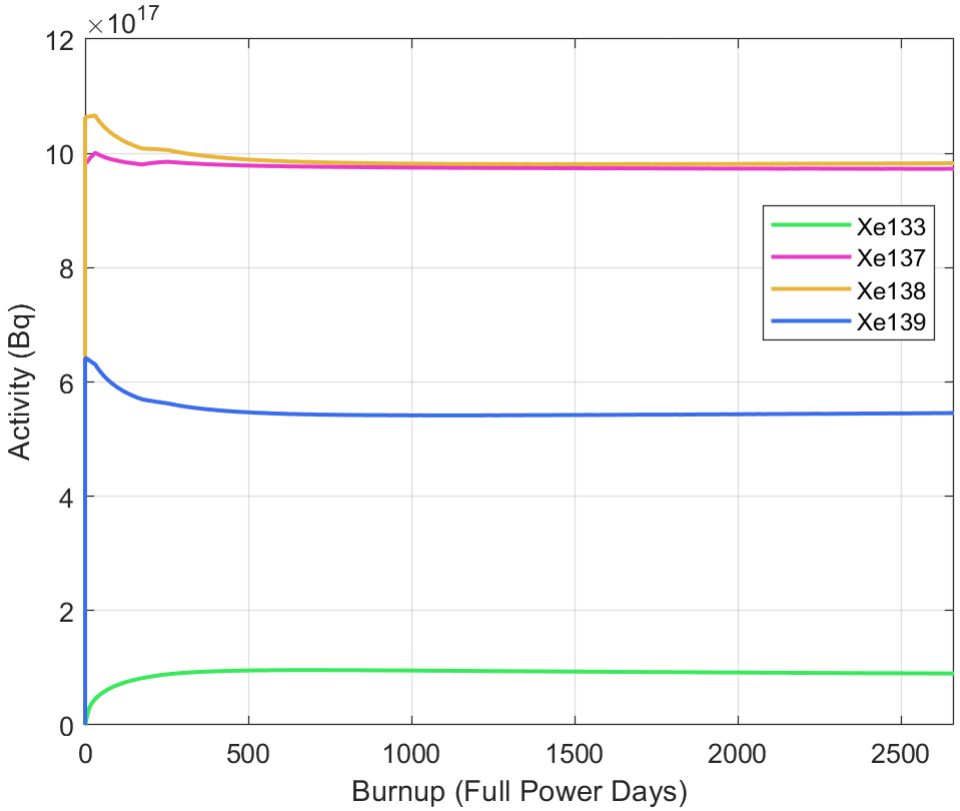


Figure 5.10: The activity of the four xenon isotopes of interest within the offgas management system across burnup.

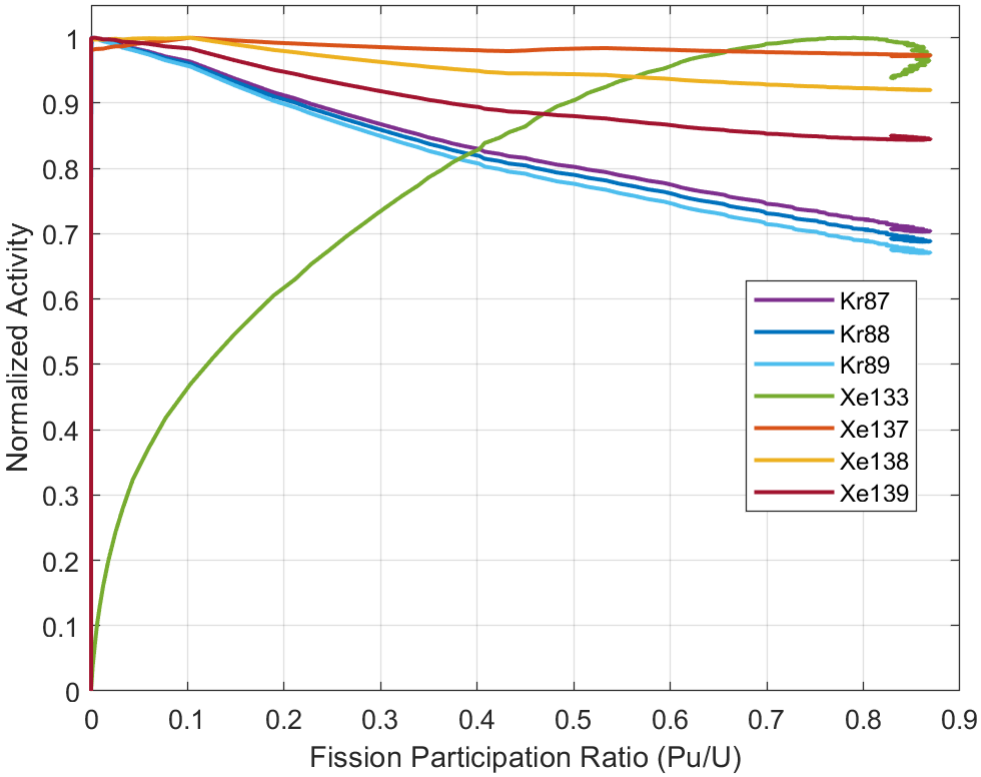


Figure 5.11: The activity of each isotope of interest, relative to the maximum activity that isotope reached, and compared to the fission participation ratio of plutonium to uranium from Figure 5.5.

Importantly, the activity of all of the isotopes trends downward with increased participation of plutonium; with exception to $^{133}$Xe, which increases. This relationship is to be expected, as seen in the relative fission yields discussed in Table 5.2. Furthermore, the slope for each of the trend-lines in Figure 5.11 indicates the degree of usefulness for its respective isotope. For example, $^{137}$Xe is shown to have the least change overall and can thus be used as a good partner in ratio with an isotope that changes significantly. As seen in the figure, two such isotopes are $^{89}$Kr, which decreases the most, and $^{133}$Xe, which increases drastically. The relevance of Figure 5.11 is that it helps indicate which isotopes may be paired well together to connect their ratio to the burnup of the fuel salt and the amount of plutonium in it. These ratios would be used in a method similar to chronometric pairs, but the difference therein is that its connection is to burnup, not directly to time. Some example isotope ratios are provided and discussed further in the next section.

### 5.5.5 Isotope Pairs

Three isotope pairs were chosen for demonstration, though others could be used. These pairs are: $^{137}$Xe to $^{89}$Kr; $^{133}$Xe to $^{89}$Kr; and $^{133}$Xe to $^{139}$Xe. The results of each are shown in Figures 5.12, 5.13, and 5.14, respectively. In each, the most change in the ratio occurs within the first five hundred days. This effect is to be expected due to the increase in $^{239}$Pu fissions during that time period; shown in Figure 5.5. In this way, the isotope ratios demonstrate a physical connection to the fission participation ratio.

The isotope pair ratios in this section are of the utmost relevance to the offgas monitoring method proposed in this work. These curves are important because they are what could be expected from an MSR plant that starts with fresh fuel salt and operates through its planned cycle without any outages.

The monitoring instrumentation would thus: observe the rate of beta particle emissions, associate them to each isotope via their beta endpoint energies shown in

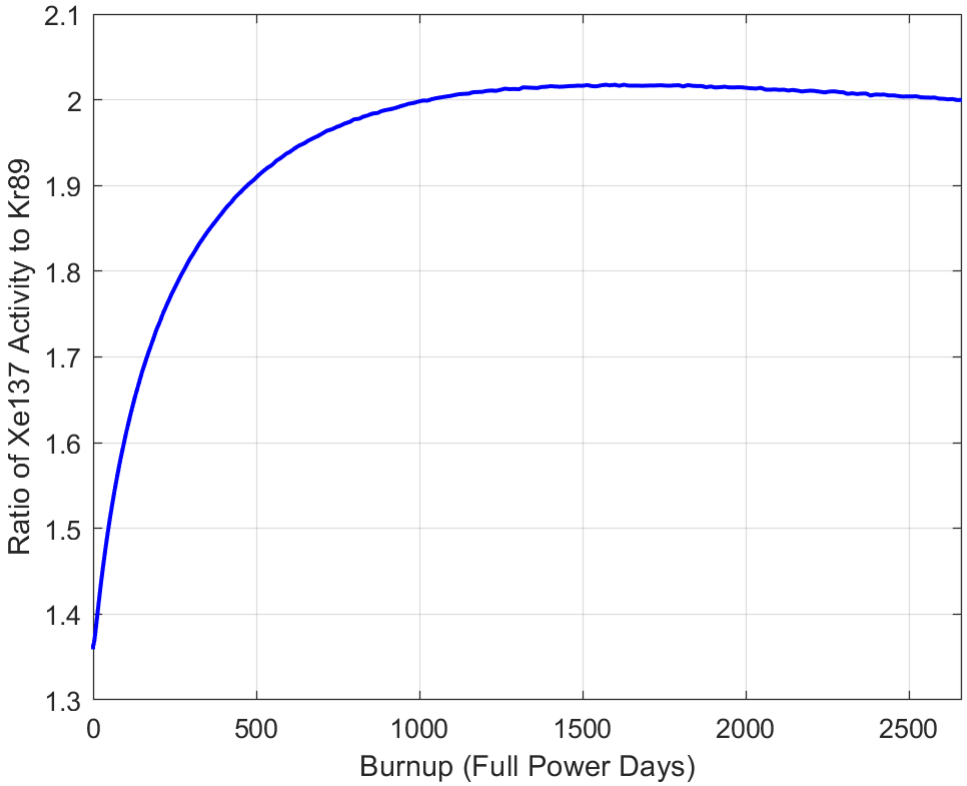


Figure 5.12: The ratio of the absolute activity of $^{137}$Xe to $^{89}$Kr in the offgas management system across burnup.

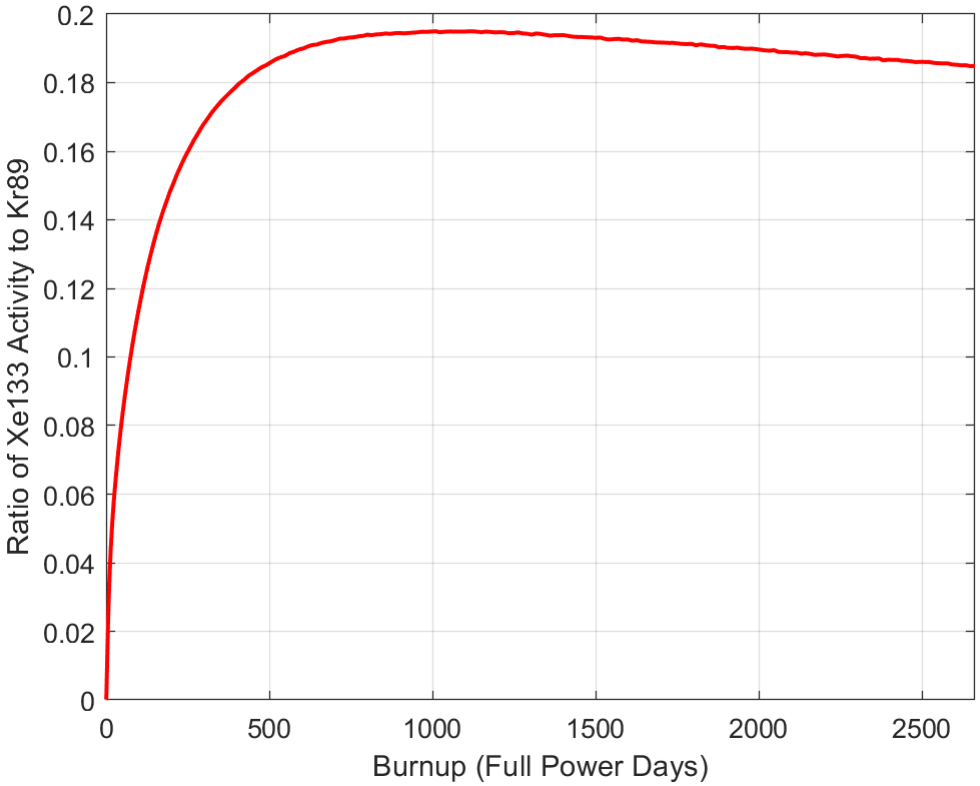


Figure 5.13: The ratio of the absolute activity of $^{133}$Xe to $^{89}$Kr in the offgas management system across burnup.

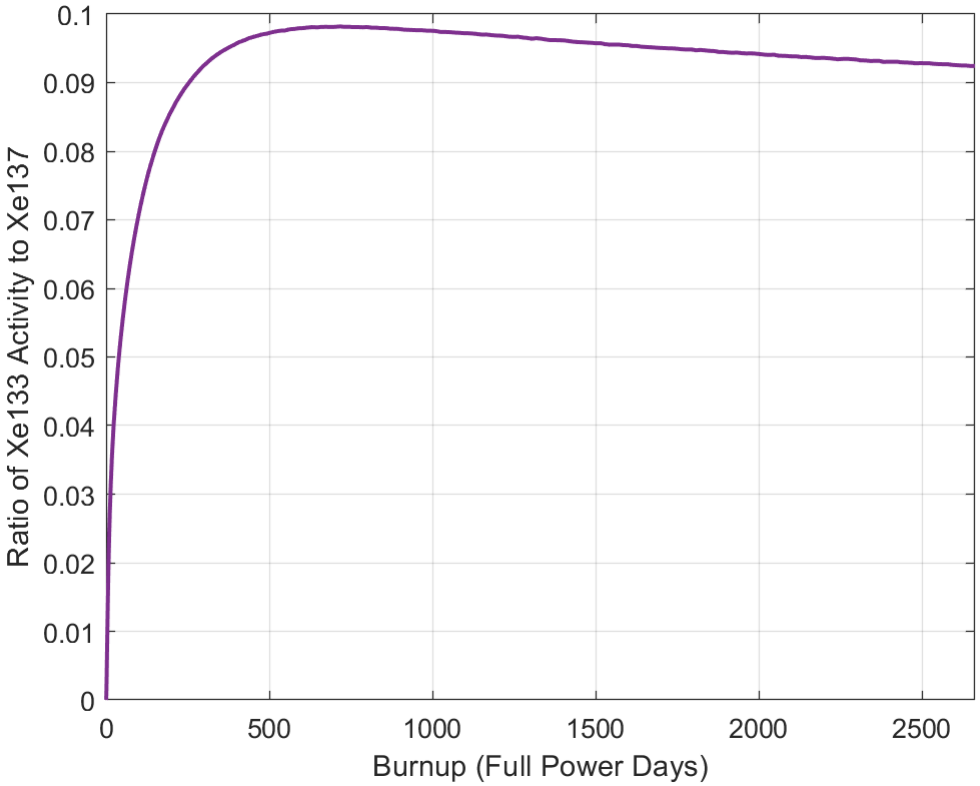


Figure 5.14: The ratio of the absolute activity of $^{133}$Xe to $^{137}$Xe in the offgas management system across burnup.

Table 5.2, calculate the ratios using the chosen pairs, and use the multiple ratios to determine both the burnup and the fraction of fissions belonging to plutonium. From the fission rate known by the reactor's power generation, the amount of plutonium in the system can be assayed. Use of different isotope pairs can decrease uncertainty in the assessment, and also allow for the determination of how much of each plutonium isotope there is in the system.

Figure 5.12 shows the activity ratio of $^{137}$Xe to $^{89}$Kr across burnup. These two isotopes were chosen as a pair due to $^{137}$Xe having the least change in relative activity across burnup, and $^{89}$Kr having the most change across burnup; with the exception of $^{133}$Xe. As seen in Figure 5.11, $^{133}$Xe is a unique case among its peers. The yield of $^{137}$Xe from the fission of $^{239}$Pu is 98% that of $^{235}$U. This rate is the closest of the isotopes of interest to 100% parity. Therefore, $^{137}$Xe can serve as a useful measuring tool for the overall fission rate. Also, yield of $^{137}$Xe from the fission of $^{241}$Pu is 107% that of $^{235}$U. This difference allows for $^{137}$Xe to be used to determine the amount of $^{241}$Pu in the system. Likewise, the yield of $^{89}$Kr from the fission of $^{239}$Pu is 32.2% that of $^{235}$U, and from the fission of $^{241}$Pu is 25.5% that of $^{235}$U. For these reasons, the $^{137}$Xe to $^{89}$Kr pair possesses the greatest change in its activity ratio across the cycle, demonstrated by y-axis steps of 0.1.

Figure 5.13 shows the activity ratio of $^{133}$Xe to $^{89}$Kr across burnup. As previously mentioned, $^{133}$Xe is a unique case among its peers, and it possesses the greatest change in relative activity across the Pu/U fission participation ratio. For this reason, it was decided to show pair it with $^{89}$Kr, which had the second greatest change in relative activity across the Pu/U fission participation ratio. The yield of $^{133}$Xe from the fission of $^{239}$Pu is 104.7% that of $^{235}$U, and from the fission of $^{241}$Pu is 100.4% that of $^{235}$U. These values indicate that, like $^{137}$Xe, the activity of $^{133}$Xe is closely tied to both uranium and plutonium. However, due to the longer half-life of $^{133}$Xe and the amount of time it takes to reach its maximum, the signal from it is more indicative of the time since the beginning of operation rather than the fission rate. The $^{137}$Xe

to $^{89}$Kr pair possesses the second greatest change in its activity ratio across the cycle of the three pairs, demonstrated by y-axis steps of 0.02.

In the previous two figures, $^{133}$Xe and $^{137}$Xe had been used to help identify $^{239}$Pu and $^{241}$Pu, respectively. They are each useful in that regard because they have a small difference in fission yield between $^{235}$U and one of the two plutonium isotopes while having a larger difference in fission yield between $^{235}$U and the other plutonium isotope. Specifically, $^{133}$Xe has a 104.7% yield ratio of $^{239}$Pu to $^{235}$U, compared to a 100.4% yield ratio of $^{241}$Pu to $^{235}$U. Conversely, $^{137}$Xe has a 98.0% yield ratio of $^{239}$Pu to $^{235}$U, compared to a 107.0% yield ratio of $^{241}$Pu to $^{235}$U. Shown in Figure 5.14, the results of this pairing have the smallest ratio of the three isotope pairs.

If large enough, a diversion of plutonium could be seen in the isotope pairs shown in this section. In future work, the diversion simulations will demonstrate the effect that removal of plutonium would have on the isotope pairs. As part of that investigation, variable amounts of plutonium could be removed at variable times in the burnup cycle and at variable rates. This process would then be able to demonstrate the overall sensitivity and timeliness of this method to determine whether or not a diversion has taken place. As for how a diversion of plutonium would affect reactor performance, more experimentation and discussion is included in previous work. [109]

## 5.6 Conclusion

Safeguards for MSRs continue to be regarded as difficult due to the inapplicability of conventional techniques used on LWRs. Whereas LWRs can utilize item accountancy solely, the homogeneous nature of the fuel salt in an MSR requires the use of bulk accountancy during operation. This necessity challenges the modern safeguards paradigm to adapt conventional techniques and develop new assay methods. The work presented in this paper is one such novel method which joins the ranks of various similar research on the topics of MSR offgas monitoring, noble gas atmospheric

monitoring, and MSR modeling. The intent of this work is to aid in the progression towards the goal of a comprehensive strategy for international safeguards.

The offgas monitoring technique demonstrated in this paper leverages the unique opportunity MSRs have to measure the beta particle emissions from recently produced fission products in an operating reactor. Similar to other nondestructive assay techniques on irradiated fuel, the underlying principle of the method is that the activity of the fission products can be linked to the identity and amount of the fissile isotopes in the system. To demonstrate this connection, the NERTHUS neutronic model [11] was used to simulate a full burnup cycle of a generic MSR and track the isotopes entering the offgas tank. Seven were chosen as isotopes of interest due to their 'Goldilocks' half-lives, distinct beta decays, reliable bubble forming, and distribution of fission yields between the three fissile isotopes considered. Of the seven isotopes of interest, three pairs were chosen to demonstrate their connection to the fissile inventory in the system.

# Chapter 6

# Conclusion

In the preceding chapters, multiple dynamic models are developed, demonstrated, and used to advance the understanding of safety and safeguards for MSRs. The systems modeled in this work are: a fast spectrum MSR inspired by Terrapower's MCFR-C, a regenerative Rankine cycle balance of plant with a once-through steam generator, a hybrid sulfur cycle industrial plant for hydrogen production, and an IES model which is comprised of all three systems. The models were developed in OpenModelica. The IES dynamic model is used in this project to simulate a variety of safety scenarios, including: LOFA in the primary loop, RIA due to control rod withdrawal, and two loss of heat sink scenarios specific to the Rankine and hybrid sulfur cycles, respectively. The methodology and development of the IES model is presented in Chapter 2 along with the LOFA and RIA scenario results. The heat sink failure scenarios and results are presented in Chapter 3 along with analysis of the frequency characteristics of the IES and the effect that the mass of the thermal manifold has on them. The theme of safety analysis is continued in Chapter 4, which takes the NERTHUS thermal spectrum generic MSR and investigates the effects that different LOFA scenarios in each of its loops have on the reactor. Lastly, Chapter 5 presents a novel safeguards technique for liquid fueled MSRs, in which, beta spectroscopy on the offgas is shown to provide information on the identity and relative quantity of fissile isotopes in the

reactor core. This safeguards technique is a form of passive, non-destructive assay with an information transmission delay in seconds.

The results of the accident analysis on the IES and NERTHUS models provide initial information on the inherent safety of MSRs. The scenarios investigated in this work, particularly for the IES, are all without any automated or operator action. The reasoning for this decision was to simplify the methodology and further isolate the inherent behavior of the system in response to the scenarios. The possibilities for automated and operator controls on a large and complex system, such as the IES presented in this work, are numerous. If standard controls were integrated effectively into the IES model, it could be expected that the system's response to the accident scenarios would be more minimal than the results shown in this work. Specifically, if a scenario affects the total heat transfer through the IES, then the control mechanisms could modify the fluid flow rates and external reactivity such that the temperatures in each of the loops are kept closer to nominal despite the decrease in overall power production. The lack of standard controls limits the IES model from simulating accident scenarios which include system responses external to the inherent behavior of the system. Similarly, there are other limitations of the IES model which could be focused on in future work to further refine the model. These limitations include: the lack of any capability to model the effects of salt freezing, salt mixing (in the event of leaks), or thermal hydraulic effects within the components. The simplifying assumption in the methodology that models system components as a collection of several control volumes with lumped parameters allows for rapid simulation of a large and complex IES in a single script, but it does also lower the fidelity of the data. The low fidelity of the data is the reason why the discussion in this work focuses on the minimum and maximum temperatures in each loop and the overall production outputs of the IES. Increased fidelity and fluid transportation delays within components could potentially affect the frequency characteristics of the IES.

The importance of this research is primarily due to the fact that these IES arrangements, with an advanced reactor system integrated with an industrial plant,

have little comparable operating experience. As such, investigation of their inherent safety characteristics can improve the deployability of the technology. Similarly, development of novel safeguards techniques for MSRs are needed due to the difficulties associated with bulk accountancy of liquid fuels. The novel contributions of this dissertation primarily include the IES dynamic model, safety analysis on the IES design, and proposal of beta spectroscopy on MSR offgas as a bulk accountancy safeguards technique. In future work, the IES model could be refined to expand its capabilities in regard to the salt phase and composition, and to raise the fidelity within the components. For the offgas analysis, the safeguards technique can be further investigated by testing its accuracy and the amount of time needed to detect a diversion under multiple scenarios including gradual and one-time diversions.

# Bibliography


[1] LLNL. "U.S. Energy Consumption in 2022". *Energy Flow Charts: Charting the Complex Relationships among Energy, Water, and Carbon*, Accessed October 2023. URL `https://flowcharts.llnl.gov`. viii, 3

[2] ORNL. *"The Molten-Salt Reactor Experiment"*. United States Atomic Energy Commission, 1969. `https://youtu.be/tyDbq5HRs0o`. xv, 139

[3] United Nations Department of Economic and Social Affairs. "World Population Prospects 2022: Summary of Results". *Population Division*, (No.3), 2022. URL `https://www.un.org/development/desa/pd/sites/www.un.org.development.desa.pd/files/wpp2022_summary_of_results.pdf`. 1

[4] "International Energy Intensity by GDP and Population". Accessed October 2023. URL `https://www.eia.gov/international/data/world/other-statistics/energy-intensity-by-gdp-and-population`. 1

[5] H.; V. Krett; J. Kupitz Barnert. "Nuclear energy for heat applications: Co-generating electricity and heat is a promising application". *Topical Reports*, 1991. 2

[6] E.D. et al Muralev. "Experience Gained in the Operation and Maintenance of the Nuclear Desalination Plant in Aktau, Kazakhstan". *IAEA-SM-347*, 1997. 2

[7] J. Weinburg and A. Ophir. "Experience Gained in the Ashdod Plant and Other Dual Purpose Desalination Plants Using Multi-Effect Distillation with Aluminium Tubes". *IAEA-SM-347*, 1997. 2

[8] Maximilian B. Gorensek and William A. Summers. “the hybrid sulfur cycle”. pages 499–545, 2011. 4

[9] Maximilian Gorensek and Bryce Edwards. “energy efficiency limits for a recuperative bayonet sulfuric acid decomposition reactor for sulfur cycle thermochemical hydrogen production”. *Industrial & Engineering Chemistry Research*, 48:7232–7245, 07 2009. doi: 10.1021/ie900310r. 4

[10] William A. Summers Maximilian B. Gorensek. “Hybrid sulfur flowsheets using PEM electrolysis and a bayonet decomposition reactor”. *International Journal of Hydrogen Energy*, 34:4097–4114, 2009. doi: http://dx.doi.org/10.1016/j.ijhydene.2008.06.049. URL `https://www.sciencedirect.com/science/article/abs/pii/S0360319908006976?via%3Dihub`. 4

[11] Nicholas J. Dunkle, Jarod Richardson, Visura Pathirana, Alex Wheeler, Ondrej Chvala, and Steven Skutnik. "NERTHUS thermal spectrum molten salt reactor neutronics and dynamic model". *Nuclear Engineering and Design*, 411:112390, 2023. ISSN 0029-5493. doi: https://doi.org/10.1016/j.nucengdes.2023.112390. `https://www.sciencedirect.com/science/article/pii/S002954932300239X`. 4, 11, 15, 46, 111, 113, 135, 136, 143, 144, 151, 171

[12] Dunkle Nicholas; Wheeler Alex; Richardson Jarod; Bogetic Sandra; Chvala Ondrej; Skutnik Steven E. "Plutonium Signatures in Molten-Salt Reactor Off-Gas Tank and Safeguards Considerations". *Journal of Nuclear Engineering*, 4(2):391–411, 2023. ISSN 2673-4362. doi: 10.3390/jne4020028. URL `https://www.mdpi.com/2673-4362/4/2/28`. 5

[13] Mathilde Huismans. "Electrification". *IEA*, 2023. https://www.iea.org/energy-system/electricity/electrification. 8

[14] IES. "Net Zero Emissions by 2050 Scenario (NZE)". *Global Energy and Climate Model*, 2023. https://www.iea.org/reports/global-energy-and-climate-model/net-zero-emissions-by-2050-scenario-nze. 8

[15] Lawrence Livermore National Laboratory. "France Energy Flow in 2017: 11,000 PJ", (2021). https://flowcharts.llnl.gov/sites/flowcharts/files/styles/orig/public/ENERGY$_2$017$_F$RANCE.png. 8

[16] NRC. "Molten Chloride Fast Reactor (MCFR)". *Pre-application Activities*, December 2023. https://www.nrc.gov/reactors/new-reactors/advanced/who-were-working-with/licensing-activities/pre-application-activities/mcfr.html. 9

[17] Terrapower, LLC. "Molten Chloride Fast Reactor Technology", (Accessed Aug 2024). https://www.terrapower.com/future/. 9

[18] Jeff Latkowski. "TerraPower's Molten Chloride Fast Reactor (MCFR)". Terrapower LLC, National Accademy of Sciences, (2021). https://www.nationalacademies.org/documents/embed/link/LF2255DA3DD1C41C0A42D3BEF0989ACAECE3053A6A9B/file/DB0D308269688B2BD7B1AF60BAA143D48890C2DE80BB?noSaveAs=1. 9, 12

[19] Claudio Corgnale, Sirivatch Shimpalee, Maximilian Gorensek, John W. Weidner, and William Summers. "Modeling of a Bayonet Reactor for Sulfuric Acid Decomposition in Thermo-Electrochemical Sulfur Based Hydrogen Production Processes". *ECS Transations*, 75(43), 2017. doi: 10.1149/07543.0007ecst. https://iopscience.iop.org/article/10.1149/07543.0007ecst. 9, 24

[20] Maximilian B. Gorensek and William A. Summers. "Hybrid sulfur flowsheets using PEM electrolysis and a bayonet decomposition reactor". *International Journal of Hydrogen Energy*, 34(9):4097–4114, 2009. ISSN 0360-3199. doi: https://doi.org/10.1016/j.ijhydene.2008.06.049. URL `https://www.sciencedirect.com/science/article/pii/S0360319908006976`. `https://doi.org/10.1016/j.ijhydene.2008.06.049`. 9, 36

[21] BWX Technologies. "Once Through Steam Generators (OTSG)", (Accessed Aug 2024). `https://www.bwxt.com/what-we-do/commercial-nuclear-components/steam-generators/once-through-steam-generators`. 9, 38

[22] ORNL. "Design and intelligent optimization of the thermal storage and energy distribution for the TerraPower Molten Chloride Fast Reactor in an Integrated Energy System (IES)". *Research Projects Impact*, 2021. `https://impact.ornl.gov/en/projects/design-and-intelligent-optimization-of-the-thermal-storage-and-en-2`. 10, 78

[23] Anna Podgordney. "Design and intelligent optimization of the thermal storage and energy distribution for the TerraPower Molten Chloride Fast Reactor in an Integrated Energy System (IES)". *U.S. DOE Nuclear Energy University Program*, 2021. `https://neup.inl.gov/Lists/Awards/DispForm.aspx?ID=904&ContentTypeId=0x01000FF41AD33234E04B888509DF4B53DDA9`. 10, 78

[24] Nicholas R. Brown. "Design and intelligent optimization of the thermal storage and energy distribution for the TerraPower Molten Chloride Fast Reactor in an Integrated Energy System (IES)". *U.S. DOE Nuclear Energy University Program*, 2021. `https://neup.inl.gov/SiteAssets/FY%202021%20Abstracts/2021%20CFA%20Technical%20Abstract%2021-24037.pdf`. 10, 78

[25] Kyra Lawson, CT Callaway, and Nicholas Brown. "Initial Assessment of an Integrated Energy System Driven by an MCFR". *Hybrid and Integrated*

*Energy Systems*, 126:622–624, 2022. https://www.ans.org/pubs/transactions/article-51516/. 10, 78

[26] CT Callaway and Nicholas Brown. "The Atkau Nuclear Power Plant and Its Relevance to Models of Nuclear Hydrogen". *Theory, Modeling and Simulation of Nuclear Chemical Processes I*, 2022. https://www.aiche.org/academy/conferences/aiche-annual-meeting/2022/proceeding/paper/268e-atkau-nuclear-power-plant-and-its-relevance-models-nuclear-hydrogen. 10, 78

[27] Kyra Lawson and Nicholas Brown. "Modeling of a Fast Chloride MSR". *MSR Workshop Presentation*, 2022. https://msrworkshop2023.ornl.gov/wp-content/uploads/2022/10/MSR2022WorkshopAGENDA$_{\text{f}}$inal$_{\text{r}}$4.pdf. 10, 11, 79

[28] Kyra Lawson and Nicholas Brown. "Development of Two-Step Method for Fast Chloride MSR Neutronics". *Nuclear Technology*, pages 1–18, 2024. doi: 10.1080/00295450.2024.2310911. https://doi.org/10.1080/00295450.2024.2310911. 10, 11, 79

[29] Kyra Lawson and Nicholas Brown. "Fast Chloride MSR Coefficients of Reactivity". *Reactor Physics of Advanced Reactors*, 130:1022–1024, 2024. https://www.ans.org/pubs/transactions/article-56218/. 10, 11, 13, 17, 79

[30] CT Callaway and Nicholas Brown. "A reduced order sulfuric acid decomposition model for a nuclear-powered hybrid sulfur cycle". *International Journal of Hydrogen Energy*, 54:1188–1198, 2024. ISSN 0360-3199. doi: https://doi.org/10.1016/j.ijhydene.2023.11.352. https://www.sciencedirect.com/science/article/pii/S0360319923062067. 10, 11, 24, 30, 32

[31] Aziz Akhlak, Caleb Brooks, CT Callaway, and Nicholas Brown. "Integrated Energy System Model in OpenModelica for Producing Energy, Powering a Desalination Plant and for District Heating". *20th International Topical Meeting on Nuclear Reactor Thermal Hydraulics (NURETH-20)*, pages 5242–5252, 2023.
https://www.ans.org/pubs/proceedings/article-54482/. 10, 11, 79

[32] Emily Meilus and Nicholas Brown. "Postulating Transient Events for Molten Chloride Fast Reactors (MCFRs) with Application for Integrated Energy Systems (IESs)". *Nuclear Installations Safety: General*, 130:844–846, 2024.
https://www.ans.org/pubs/transactions/article-56175/. 10, 11, 79

[33] Steven E. Skutnik. "Development of an MC&A toolbox for liquidfueled molten salt reactors with online reprocessing". *U.S. DOE Nuclear Energy University Program*, 2018.
https://neup.inl.gov/SiteAssets/FY%202018%20Abstracts/CFA-18-15061_TechnicalAbstract_2018CFATechnicalAbstract18-15061.pdf. 11

[34] Ondrej Chvala and Steven E. Skutnik. "Development of an MC&A toolbox for liquid-fueled molten salt reactors with online reprocessing: Final Report". *U.S. DOE Nuclear Energy University Program*, 2022. doi: 10.2172/1958864.
https://www.osti.gov/biblio/1958864. 11

[35] Nicholas J. Dunkle, Alex Wheeler, Jarod Richardson, Sandra Bogetic, Ondrej Chvala, and Steven Skutnik. "Plutonium Signatures in Molten-Salt Reactor Off-Gas Tank and Safeguards Considerations". *Journal of Nuclear Engineering*, 4:391–411, 05 2023. doi: 10.3390/jne4020028.
https://www.researchgate.net/publication/370884612_Plutonium_Signatures_in_Molten-Salt_Reactor_Off-Gas_Tank_and_Safeguards_Considerations. 11

[36] Nicholas J. Dunkle and Sandra Bogetic. "Molten Salt Reactor Loss of Flow Accident Analysis using the NERTHUS Dynamic Model". *Nuclear Science and Technology Open Research*, 2023. https://doi.org/10.12688/nuclscitechnolopenres.17459.1. 11

[37] Alexey Lokhov. "Technical and Economic Aspects of Load Following with Nuclear Power Plants". *OECD Nuclear Energy Agency*, Nuclear Development, 2011. https://www.oecd-nea.org/upload/docs/application/pdf/2021-12/technical_and_economic_aspects_of_load_following_with_nuclear_power_plants.pdf. 11

[38] Nicholas J. Dunkle and Ondrej Chvala. "Effect of xenon removal rate on load following in high power thermal spectrum Molten-Salt Reactors (MSRs)". *Nuclear Engineering and Design*, 409:112329, 2023. ISSN 0029-5493. doi: https://doi.org/10.1016/j.nucengdes.2023.112329. https://www.sciencedirect.com/science/article/pii/S0029549323001784. 11, 110, 135, 141, 153

[39] N. R. Brown, V. Seker, S. T. Revankar, and T. J. Downar. "Transient simulation of an endothermic chemical process facility coupled to a high temperature reactor: Model development and validation". *Nuclear Engineering and Design*, 248:1–13, 2012. ISSN 0029-5493. doi: https://doi.org/10.1016/j.nucengdes.2012.03.049. URL https://www.sciencedirect.com/science/article/pii/S0029549312001835. https://doi.org/10.1016/j.nucengdes.2012.03.049. 12

[40] N. R. Brown and S. T. Revankar. "A review of catalytic sulfur (VI) oxide decomposition experiments". *International Journal of Hydrogen Energy*, 37 (3):2685–2698, 2012. ISSN 0360-3199. doi: https://doi.org/10.1016/j.ijhydene.2011.10.054. URL https:

//www.sciencedirect.com/science/article/pii/S0360319911024165. https://doi.org/10.1016/j.ijhydene.2011.10.054. 12

[41] Center for Sustainable Systems. "Hydrogen Factsheet". *University of Michigan*, Pub. No. CSS23-07., 2023. https://css.umich.edu/sites/default/files/2023-10/Hydrogen$_{C}$SS23-07.pdf. 12

[42] CEVA Logistics. "Energy Density of a Battery", (Accessed August 2024). https://www.cevalogistics.com/en/glossary/energy-density-battery. 12

[43] EIA. "Hydrogen explained: Production of hydrogen". *U.S. Energy Information Administration*, 2023. https://www.eia.gov/energyexplained/hydrogen/production-of-hydrogen.php. 12

[44] Ibrahim Dincer and Calin Zamfirescu. *"Sustainable Hydrogen Production"*. Elsevier, (2017). ISBN 978-0-12-801563-6. https://doi.org/10.1016/C2014-0-00658-2. 12

[45] EIA. "Hydrogen explained: Use of hydrogen". *U.S. Energy Information Administration*, 2024. https://www.eia.gov/energyexplained/hydrogen/use-of-hydrogen.php. 12

[46] David B. Mengel. "Types and Uses of Nitrogen Fertilizers for Crop Production". *Agronomy Guide*, 1986. https://www.extension.purdue.edu/extmedia/ay/ay-204.html. 12

[47] Antoine Hoxha. "Clean Hydrogen as A Major Enabler for Making Carbon-Free Ammonia and Fertilizers". *Fertilizers Europe*, 2021.

https://www.europeanfiles.eu/climate/clean-hydrogen-as-a-major-enabler-for-making-carbon-free-ammonia-and-fertilizers. 12

[48] Tommy Cisneros, Matt Wargon, and Jeff Latkowski. "Representative Neutronics Models of MCFR Reactors". *MCFR-ENG-PRSNT-0021*, Revision 0:1–15, 2023. 12, 22

[49] Dan Walter. "MCRE Design Description in Support of External Model Development". *MCRE-ENG-PRSNT-0029*, Revision 1A:1–26, 2022. 12

[50] James J. Duderstadt and Louis J. Hamilton. *"Nuclear Reactor Analysis"*. University of Michighan, Ann Arbor, Michighan, (1976). ISBN 0-471-22363-8. https://deepblue.lib.umich.edu/handle/2027.42/89079. 13, 15

[51] John Macphee. "The Kinetics of Circulating Fuel Reactors". *Nuclear Science and Engineering*, 4(4):588–597, 1958. doi: 10.13182/NSE4-588-597. https://doi.org/10.13182/NSE4-588-597. 15

[52] S. Dulla, P. Ravetto, and M. M. Rostagno. "Neutron kinetics of fluid–fuel systems by the quasi-static method". *Annals of Nuclear Energy*, 31(15): 1709–1733, 2004. ISSN 0306-4549. doi: https://doi.org/10.1016/j.anucene.2004.05.004. https://www.sciencedirect.com/science/article/pii/S0306454904000982. 15

[53] Benjamin R. Betzler, Florent Heidet, Bo Feng, Cristian Rabiti, Tanju Sofu, and Nicholas R. Brown. "Modeling and simulation functional needs for molten salt reactor licensing". *Nuclear Engineering and Design*, 355:110308, 2019. ISSN 0029-5493. doi: https://doi.org/10.1016/j.nucengdes.2019.110308. URL https://www.sciencedirect.com/science/article/pii/S0029549319303437. https://doi.org/10.1016/j.nucengdes.2019.110308. 15

[54] Won Yang. "Fast reactor physics and computational methods". *Nuclear Engineering and Technology*, 44, 03 2012. doi: 10.5516/NET.01.2012.504. https://www.researchgate.net/publication/264145852_Fast_reactor_physics_and_computational_methods. 17

[55] E. L. Compere, S. S. Kirslis, E. G. Bohlmann, F. F. Blankenship, and W. R. Grimes. "Fission product behavior in the Molten Salt Reactor Experiment". *Oak Ridge National Lab*, 10 1975. doi: 10.2172/4077644. https://www.osti.gov/biblio/4077644. 19, 136, 137, 149

[56] C. F. Jr Baes. "The Chemistry and Thermodynamics of Molten Salt Reactor Fuels". *Journal of Nuclear Materials*, 51(1):149–162, May 1974. ISSN 0022-3115. doi: https://doi.org/10.1016/0022-3115(74)90124-X. https://www.sciencedirect.com/science/article/pii/002231157490124X. 19, 136, 145, 149

[57] T. R. England and B. F. Rider. "Evaluation and Compilation of Fission Product Yields", October (1994). https://www-nds.iaea.org/endf349/. 19, 150

[58] M. B. Chadwick, P Obložinskỳ, Michal Herman, N. M. Greene, R. D. McKnight, D. L. Smith, P. G. Young, R. E. MacFarlane, G. M. Hale, and S. C. et al Frankle. "ENDF/B-VII. 0: next generation evaluated nuclear data library for nuclear science and technology". *Nuclear data sheets*, 107(12): 2931–3060, 2006. 19, 144

[59] C.W. Jr. Nestor. "Murgatroyd - An IBM 7090 Program for the Analysis of the Kinetics of the MSRE". Technical Report ORNL-TM-203, Oak Ridge National Laboratory, Oak Ridge, TN, 4 (1962). https://www.osti.gov/biblio/4786415. 19

[60] S. J. Ball. "Approximate Models for Distributed-Parameter Heat-Transfer Systems". *ISA Transactions*, 3(1):38–47, (1964). https://digital.library.unt.edu/ark:/67531/metadc1201699/. 19

[61] S. J. Ball and T. W. Kerlin. *"Stability Analysis of the Molten-Salt Reactor Experiment"*. Oak Ridge National Laboratory, (1966). http://moltensalt.org/references/static/downloads/pdf/ORNL-TM-1070.pdf. 19, 110

[62] R. C. Robertson. *"MSRE Design and Operations Report. Part 1. Description of Reactor Design"*. Oak Ridge National Laboratory, (1965). http://moltensalt.org/references/static/downloads/pdf/ORNL-TM-0728.pdf. 19

[63] Carolina Villada, Wenjin Ding, Alexander Bonk, and Thomas Bauer. "Engineering molten MgCl2–KCl–NaCl salt for high-temperature thermal energy storage: Review on salt properties and corrosion control strategies". *Solar Energy Materials and Solar Cells*, 232:111344, 2021. ISSN 0927-0248. doi: https://doi.org/10.1016/j.solmat.2021.111344. https://www.sciencedirect.com/science/article/pii/S092702482100386X. 22

[64] Xiaoxin Wang, Jesus Del Rincon, Peiwen Li, Youyang Zhao, and Judith Vidal. "Thermophysical Properties Experimentally Tested for NaCl-KCl-MgCl2 Eutectic Molten Salt as a Next-Generation High-Temperature Heat Transfer Fluids in Concentrated Solar Power Systems". *Journal of Solar Energy Engineering*, 143(4):041005, 01 2021. ISSN 0199-6231. doi: 10.1115/1.4049253. https://doi.org/10.1115/1.4049253. 22

[65] Yuanyuan Li, Xiankun Xu, Xiaoxin Wang, Peiwen Li, Qing Hao, and Bo Xiao. "Survey and evaluation of equations for thermophysical properties of binary/ternary eutectic salts from NaCl, KCl, MgCl2, CaCl2, ZnCl2 for heat transfer and thermal storage fluids in CSP". *Solar Energy*, 152:57–79, 2017.

ISSN 0038-092X. doi: https://doi.org/10.1016/j.solener.2017.03.019. Progress in Solar Energy Special Issue: Concentrating Solar Power (CSP). 24

[66] Coastal Chemical Co. LLC. "HITEC® Heat Transfer Salt". 2023. https://coastalchem.com/products/heat-transfer-fluids/hitec-heat-transfer-salt/. 24, 29, 113, 145

[67] Gerhard Venter. "Process sensitivity of the Hybrid Sulphur thermochemical cycle". Master's thesis, North-West University, Potchefstroom, South Africa, May (2010). http://hdl.handle.net/10394/5067. 24, 30

[68] M. D. Coetzee. "The Chemical Reactor for the Decomposition of Sulphuric Acid for the Hybrid Sulphur Process". Master's thesis, North-West University, Potchefstroom, South Africa, November (2008). http://hdl.handle.net/10394/3143. 24, 30, 32

[69] Peter J. Linstrom. "A Guide to the NIST Chemistry WebBook". *NIST*, SRD 69, Accessed Aug 2024. https://webbook.nist.gov/chemistry/guide/. 32, 33, 36

[70] M.W. Jr. Chase. "NIST-JANAF Themochemical Tables". *J. Phys. Chem. Ref. Data, Monograph 9*, Fourth Edition:1–1951, 1998. https://webbook.nist.gov/cgi/cbook.cgi?Source=1998CHA1-1951&Mask=FFF. 32

[71] Yunus A. Çengel and Michael A. Boles. *"Thermodynamics: An Engineering Approach"*. Number 8th Edition. McGraw-Hill Education, (2015). ISBN 978-0-07-339817-4. 37

[72] Jeffrey Robert Kapernick. "Dynamic Modeling of a Small Modular Reactor for Control and Monitoring". Master's thesis, University of Tennessee, Knoxville, Knoxville, TN, May (2015). https://trace.tennessee.edu/utk$_g$radthes/3377/. 38

[73] Vikram Singh. "Study of the Dynamic Behavior of Molten-Salt Reactors". Master's thesis, University of Tennessee, Knoxville, Knoxville, TN, May 2019. https://trace.tennessee.edu/utk_gradthes/5482/. 38, 45

[74] Vikram Singh, Alexander M. Wheeler, Belle R. Upadhyaya, Ondřej Chvála, and Scott M. Greenwood. "Plant-level dynamic modeling of a commercial-scale molten salt reactor system". *Nuclear Engineering and Design*, 360:110457, 2020. ISSN 0029-5493. doi: https://doi.org/10.1016/j.nucengdes.2019.110457. https://www.sciencedirect.com/science/article/pii/S0029549319304881. 38

[75] Modelica Association. "Package Modelica.Media.Water.StandardWater", (Accessed 2024). https://doc.modelica.org/Modelica%203.2.3/Resources/helpMapleSim/Media/Water/StandardWater/index.html. 48

[76] Modelica Association. "ReferenceMoistAir: Detailed moist air model (143.15 ... 2000 K)", (Accessed 2024). https://doc.modelica.org/Modelica%204.0.0/Resources/helpDymola/Modelica_MediaA_ir_ReferenceMoistAir.html. 48

[77] W. Wagner, J. R. Cooper, A. Dittmann, J. Kijima, H. J. Kretzschmar, A. Kruse, R. Mareš, K. Oguchi, H. Sato, I. Stöcker, O. Šifner, Y. Takaishi, I. Tanishita, J. Trübenbach, and Th. Willkommen. "The IAPWS Industrial Formulation 1997 for the Thermodynamic Properties of Water and Steam". *Journal of Engineering for Gas Turbines and Power*, 122:150–184, 2000. ISSN 0742-4795. doi: 10.1115/1.483186. URL https://doi.org/10.1115/1.483186. https://asmedigitalcollection.asme.org/gasturbinespower/article-pdf/122/1/150/5548474/150_1.pdf. 48

[78] Cleansky. "Modelica Model Library Development for Media, Magnetic Systems and Wavelets: Verification Report". 2013. https://doc.modelica.org/Modelica%204.0.0/Resources/Documentation/Media/MoMoLib_VerificationResults_XRG.pdf. 48

[79] L. J. Koch, H. O. Monson, W. R. Simmons, M. Levenson, F. Verber, E. Hutter, R. A. Jaross, T. R. Spalding, J. R. Simanton, and A. Lovoff. "Construction Design of EBR-II: An Integrated Unmoderated Nuclear Power Plant". *A/CONF.15/P/1782*, 10 1958. doi: 10.2172/4325807. https://www.osti.gov/biblio/4325807. 52

[80] A Alvestav. "State-of-the-art Report on Nuclear Fuel Behaviour Under Reactivity initiated Accident Conditions". *Nuclear Safety*, No. 7575:1–336, 2022. https://www.oecd-nea.org/upload/docs/application/pdf/2022-10/7575_ria_soar.pdf. 52

[81] D. J. Diamond, B. P. Bromley, and A. L. Aronson. "Studies of the Rod Ejection Accident in a PWR". *Energy Sciences & Technology Dept.*, W-6382, 2022. https://www.nrc.gov/docs/ML0204/ML020430129.pdf. 53

[82] Marc Petit. "Nuclear Fuel Behaviour during Reactivity Initiated Accidents". *Committee on the Safety of Nuclear Installations*, NEA/CSNI/R(2010)7: 1–433, 2010. https://www.oecd-nea.org/upload/docs/application/pdf/2021-03/csni-r2010-7.pdf. 53

[83] T. Sumner, T. Kim, and T. H. Fanning. "Analysis of VTR Primary Pump Coastdown". *Nuclear Science and Engineering Division*, 4 2019. doi: 10.2172/1868341. https://www.osti.gov/biblio/1868341. 53

[84] T. Kim, T. Sumner, and T. H. Fanning. "Assessment of Pump Coastdown and Reactor Protection Scram Delays during Station Blackout Conditions". *Nuclear Science and Engineering Division*, 4 2019. doi: 10.2172/1868342. https://www.osti.gov/biblio/1868342. 53

[85] G. Purciarello. "Ultimate Heat Sink for Nuclear Power Plants". *Regulatory Guide 1.27*, Revision 3:1–16, 2015. https://www.nrc.gov/docs/ML1410/ML14107A411.pdf. 55

[86] Nicholas J. Dunkle, Sandra Bogetic, and Brown Nicholas. "Dynamic Modeling of a Fast Spectrum Molten Salt Reactor Integrated Energy System". *In Review by Nuclear Science and Engineering*, 2024. 78, 79

[87] Howard Austerlitz. Chapter 4 - analog/digital conversions. In Howard Austerlitz, editor, *"Data Acquisition Techniques Using PCs (Second Edition)"*, pages 51–77. Academic Press, San Diego, second edition edition, 2003. ISBN 978-0-12-068377-2. doi: https://doi.org/10.1016/B978-012068377-2/50004-8. URL `https://www.sciencedirect.com/science/article/pii/B9780120683772500048`. 81

[88] J. Katz, R.F. Burkard, and L. Medwetsky. *"Handbook of Clinical Audiology"*. Lippincott Williams & Wilkins, 2002. ISBN 9780683307658. URL `https://books.google.com/books?id=CBFhLXcyJ4UC`. 81

[89] Donald N. Kovacic, Andrew Worrall, Louise G. Worrall, George F. Flanagan, David Eugene Holcomb, Robert Bari, Lap Cheng, David Farley, and Matthew Sternat. "Safeguards Challenges for Molten Salt Reactors". *USDOE*, INMM Annual Meeting, 8 2018. URL `https://www.osti.gov/biblio/1474868`. 110

[90] Michael P. Dion, Michael Scott Greenwood, Karen K. Hogue, Sean E. O'Brien, Logan M. Scott, and Greg T. Westphal. "Material Control & Accountancy for Molten Salt Reactors (FY2021 Report)". 9 2021. doi: 10.2172/1840163. URL `https://www.osti.gov/biblio/1840163`. 110

[91] R. C. Steffy T. W. Kerlin, S. J. Ball and M. R. Buckner. "Experiences with Dynamic Testing Methods at the Molten-Salt Reactor Experiment". *Nuclear Technology*, 10(2):103–117, 1971. doi: 10.13182/NT71-A30919. URL `https://doi.org/10.13182/NT71-A30919`. 110

[92] IAEA. "Molten Salt Reactors". Date Accessed NOV 2023. URL https://www.iaea.org/topics/molten-salt-reactors. 110

[93] H. G. MacPherson. The molten salt reactor adventure. *Nuclear Science and Engineering*, 90(4):374–380, 1985. doi: 10.13182/NSE90-374. URL https://doi.org/10.13182/NSE90-374. 110

[94] S Wang; A Rineiski; D Zhang; E Merle-Lucotte R Li. "Transient analyses for a molten salt fast reactor with optimized core geometry". *Nuclear Engineering and Design*, 292:164–176, 2015. 110, 135

[95] S Goluoglu Z Mausolff, M DeHart. "Design and assessment of a molten chloride fast reactor". *Nuclear Engineering and Design*, 379:111–181, 2021. 110, 135

[96] ORNL. "Molten Salt Reactor Experiment 1965-1972". https://web.archive.org/web/20160303211133if_/https://dl.dropboxusercontent.com/u/15726934/Historic_Molten_Salt_Reactor_Experiment_Brochure_ORNL_1965-1972.pdf, 2016. 110

[97] S.J. Ball and T.W. Kerlin. *"Experimental Dynamic Analysis of the Molten-Salt Reactor Experiment"*. Oak Ridge National Laboratory, 1966. 110

[98] Ritsuo Yoshioka and Koshi Mitachi. "SAFETY CRITERIA AND GUIDELINES FOR MSR ACCIDENT ANALYSIS". *PHYSOR 2014 – The Role of Reactor Physics Toward a Sustainable Future*, page 19, 2014. URL http://tamachan.cute.coocan.jp/MSR%20accident%20gudelines140623.pdf. 110

[99] Dunkle, Nicholas and Chvala, Ondrej. "Nerthus Dynamic Model Respository", 2022. URL https://github.com/ondrejch/2022-NERTHUS-system-dynamics. 111

[100] Matlab. "Simulink". https://www.mathworks.com/products/simulink.html, 2022. 111

[101] Dunkle, Nicholas. "NERTHUS Dynamic Model in OpenModelica Respository", 2023. URL `https://github.com/njdunkle/2023-NERTHUS-Modelica`. 111

[102] Jaakko Leppanen. *"Serpent – a Continuous-energy Monte Carlo Reactor Physics Burnup Calculation Code"*, 6 2015. URL `https://usermanual.wiki/Document/Serpentmanual.1526141273/view`. 113, 135

[103] Alexander M. Wheeler Visura Pathirana, Ondrej Chvala. Scalable modular dynamic molten salt reactor system model with decay heat. 11 2020. 114

[104] Kim, T. and Sumner, T. and Fanning, T. "Assessment of Pump Coastdown and Reactor Protection Scram Delays during Station Blackout Conditions". *Nuclear Science and Engineering Division*, 4 2019. doi: 10.2172/1868342. URL `https://www.osti.gov/biblio/1868342`. 114

[105] Sumner, T. and Kim, T. and Fanning, T. H. "Analysis of VTR Primary Pump Coastdown". *Nuclear Science and Engineering Division*, 4 2019. doi: 10.2172/1868341. URL `https://www.osti.gov/biblio/1868341`. 114

[106] Dunkle, Nicholas. "2023-NERTHUS-Pumpfail-Data-csv", 2023. URL `https://zenodo.org/records/10275128`. 116

[107] Baral, Khagendra et Al. "Temperature-Dependent Properties of Molten $Li_2BeF_4$ Salt Using Ab *Initio* Molecular Dynamics". *ACS Omega*, 6(30): 19822–19835, 2021. doi: 10.1021/acsomega.1c02528. 122

[108] Dunkle, Nicholas and Chvala, Ondrej. "Safeguards By Design Considerations For Modular Molten Salt Reactors". INMM/ESARDA Joint Annual Meeting,

INMM, 2021. https://resources.inmm.org/annual-meeting-proceedings/safeguards-design-considerations-modular-molten-salt-reactors. 134, 135, 142

[109] Alexander M. Wheeler, Ondřej Chvála, and Steven Skutnik. "Signatures of plutonium diversion in Molten Salt Reactor dynamics". *Annals of Nuclear Energy*, 160:108370, 2021. ISSN 0306-4549. doi: https://doi.org/10.1016/j.anucene.2021.108370. URL https://www.sciencedirect.com/science/article/pii/S0306454921002462. 135, 155, 170

[110] H. G. MacPherson. "The Molten Salt Reactor Adventure". *Nuclear Science and Engineering*, 90(4):374–380, 1985. doi: 10.13182/NSE90-374. URL https://doi.org/10.13182/NSE90-374. 135

[111] Heather M. Felmy, Andrew J. Clifford, Adan Schafer Medina, Richard M. Cox, Jennifer M. Wilson, Amanda M. Lines, and Samuel A. Bryan. "On-Line Monitoring of Gas-Phase Molecular Iodine Using Raman and Fluorescence Spectroscopy Paired with Chemometric Analysis". *Environmental Science & Technology*, 55(6):3898–3908, 2021. doi: 10.1021/acs.est.0c06137. URL https://pubs.acs.org/doi/10.1021/acs.est.0c06137. PMID: 33411509. 136

[112] Kendall D. Hughey, Ashley M. Bradley, Heather M. Felmy, Andrew J. Clifford, Richard M. Cox, Amanda M. Lines, Samuel A. Bryan, and Timothy J. Johnson. "Quantitative far-infrared band strengths of iodine monochloride (ICl), a molten salt off-gas product". In Jason A. Guicheteau and Chris R. Howle, editors, *Chemical, Biological, Radiological, Nuclear, and Explosives (CBRNE) Sensing XXI*, volume 11416, page 114160Q. International Society for Optics and Photonics, SPIE, 2020. doi: 10.1117/12.2557555. URL https://doi.org/10.1117/12.2557555. 136

[113] Kendall D. Hughey, Ashley M. Bradley, Russell G. Tonkyn, Heather M. Felmy, Thomas A. Blake, Samuel A. Bryan, Timothy J. Johnson, and Amanda M. Lines. "Absolute Band Intensity of the Iodine Monochloride Fundamental Mode for Infrared Sensing and Quantitative Analysis". *The Journal of Physical Chemistry A*, 124(46):9578–9588, 2020. doi: 10.1021/acs.jpca.0c07353. URL https://doi.org/10.1021/acs.jpca.0c07353. PMID: 33153259. 136

[114] Matthew H. Carpenter et al. "EXPERIMENTAL VALIDATION OF NDA CAPABILITIES FOR MSR SAFEGUARDS: FIRST RESULTS". *INMM& ESARDA Joint Virtual Annual Meeting*, 2021. 136

[115] Aaron M. Graham, Zack Taylor, Benjamin S. Collins, Robert K. Salko, and Max Poschmann. "Multiphysics Coupling Methods for Molten Salt Reactor Modeling and Simulation in VERA". *Nuclear Science and Engineering*, 195 (10), 5 2021. ISSN 0029-5639. doi: 10.1080/00295639.2021.1901000. URL https://www.osti.gov/biblio/1818739. 136

[116] Charles W. Nakhleh, William D. Stanbro, Louis N. Hand, and R.T. Perry Jr., William B. Wilson, and Bryan L. Fearey. "Noble-gas atmospheric monitoring for international safeguards at reprocessing facilities". *Science & Global Security*, 6(3):357–379, 1997. doi: 10.1080/08929889708426444. URL https://doi.org/10.1080/08929889708426444. 136

[117] Brian J. Riley, Joanna Mcfarlane, Guillermo DelCul, John D. Vienna, Cristian I. Contescu, Laurie M. Hay, A. V. Savino, and Harold E. Adkins. "Identification of Potential Waste Processing and Waste Form Options for Molten Salt Reactors". 8 2018. doi: 10.2172/1543229. URL https://www.osti.gov/biblio/1543229. 137

[118] Hunter B. Andrews, Joanna McFarlane, A. Shay Chapel, N. Dianne Bull Ezell, David E. Holcomb, Dane de Wet, Michael S. Greenwood, Kristian G.

Myhre, Samuel A. Bryan, Amanda Lines, Brian J. Riley, Heather M. Felmy, and Paul W. Humrickhouse. "Review of molten salt reactor off-gas management considerations". *Nuclear Engineering and Design*, 385:111529, 2021. ISSN 0029-5493. doi: https://doi.org/10.1016/j.nucengdes.2021.111529. URL `https://www.sciencedirect.com/science/article/pii/S0029549321004817`. 137, 151

[119] Joanna McFarlane, Brian Riley, David Eugene Holcomb, Amanda Lines, Hunter B. Andrews, Sam A. Bryan, A. Shay Chapel, N. Dianne Bull Ezell, Heather M. Felmy, Michael Scott Greenwood, Paul W. Humrickhouse, and Kristian Myhre. "Molten Salt Reactor Engineering Study for Off-Gas Management". *Oak Ridge National Laboratory*, 8 2020. doi: 10.2172/1649021. URL `https://www.osti.gov/biblio/1649021`. 137, 151

[120] R C. Robertson. "MSRE Design & Operations Report Part 1 Description of Reactor Design". *ORNL-TM-728*, 1 1965. doi: 10.2172/4654707. URL `http://moltensalt.org/references/static/downloads/pdf/ORNL-TM-0728.pdf`. 137, 151

[121] R C Robertson. "CONCEPTUAL DESIGN STUDY OF A SINGLE-FLUID MOLTEN-SALT BREEDER REACTOR.". 1 1971. doi: 10.2172/4030941. URL `https://www.osti.gov/biblio/4030941`. 138, 149

[122] Brian J. Riley, Joanna McFarlane, Guillermo D. DelCul, John D. Vienna, Cristian I. Contescu, and Charles W. Forsberg. "Molten Salt Reactor Waste and Effluent Management Strategies: A review". *Nuclear Engineering and Design*, 345:94–109, 2019. ISSN 0029-5493. doi: https://doi.org/10.1016/j.nucengdes.2019.02.002. URL `https://www.sciencedirect.com/science/article/pii/S002954931930024X`. 138

[123] Debasis Banerjee, Amy J. Cairns, Jian Liu, Radha K. Motkuri, Satish K. Nune, Carlos A. Fernandez, Rajamani Krishna, Denis M. Strachan, and Praveen K. Thallapally. "Potential of Metal–Organic Frameworks for Separation of Xenon and Krypton". *Accounts of Chemical Research*, 48(2): 211–219, 2015. doi: 10.1021/ar5003126. URL https://pubs.acs.org/doi/10.1021/ar5003126. PMID: 25479165. 138

[124] IAEA. *"On-line Monitoring for Improving Performance of Nuclear Power Plants Part 2: Process and Component Condition Monitoring and Diagnostics"*. Number NP-T-1.2 in Nuclear Energy Series. INTERNATIONAL ATOMIC ENERGY AGENCY, Vienna, Austria, 2008. ISBN 978-92-0-101208-1. URL https://www.iaea.org/publications/7908/on-line-monitoring-for-improving-performance-of-nuclear-power-plants-part-2-process-and-component-condition-monitoring-and-diagnostics. 140, 141

[125] Michael H. Ehinger, George D. Pomeroy, and Kory W. Budlong-Sylvester. "Process Monitoring for Nuclear Safeguards". In *NUCLEAR FUEL CYCLE AND FUEL MATERIALS (S11)*. ORNL, INIS, 2009. URL https://inis.iaea.org/search/searchsinglerecord.aspx?recordsFor=SingleRecord&RN=43126277. 140

[126] Amanda M. Lines, Gabriel B. Hall, Susan Asmussen, Jarrod Allred, Sergey Sinkov, Forrest Heller, Neal Gallagher, Gregg J. Lumetta, and Samuel A. Bryan. "Sensor Fusion: Comprehensive Real-Time, On-Line Monitoring for Process Control via Visible, Near-Infrared, and Raman Spectroscopy". *ACS Sensors*, 5(8):2467–2475, 2020. doi: 10.1021/acssensors.0c00659. URL https://pubs.acs.org/doi/abs/10.1021/acssensors.0c00659. PMID: 32662261. 141

[127] Donald N. Kovacic, Andrew Worrall, Louise G. Worrall, George F. Flanagan, David Eugene Holcomb, Robert Bari, Lap Cheng, David Farley, and Matthew Sternat. "Safeguards Challenges for Molten Salt Reactors". *USDOE*, 8 2018. URL `https://www.osti.gov/biblio/1474868`. 141

[128] J.R. Phillips. *"Passive Nondestructive Assay of Nuclear Materials - Irradiated Fuel Measurements"*, 3 1991. URL `https://www.lanl.gov/org/ddste/aldgs/sst-training/assets/docs/PANDA/Iradiated%20Fuel%20Measurements%20Ch.%2018%20p.%20529-562.pdf`. 141

[129] O Beneš, E Capelli, N Morelová, J-Y Colle, A Tosolin, T Wiss, B Cremer, and RJM Konings. Cesium and iodine release from fluoride-based molten salt reactor fuel. *Physical Chemistry Chemical Physics*, 23(15):9512–9523, 2021. 143

[130] Geng, Junxia and Zhao, Zhongqi and Cheng, Zhiqiang and Li, Wenxin and Dou, Qiang and Li, Qingnuan. Activity measurement of iodine fission products in 2lif-bef2 salt and its application in redox potential surveillance for a thorium molten salt reactor. *Inorganic Chemistry*, 2022. 143

[131] ThorCon USA Inc. Thorcon documents. https://thorconpower.com/documents, 2021. 143

[132] Alexander M Wheeler and Ondřej Chvála. "Molten Salt Reactor Sourdough Refueling and Waste Management Strategy". *Journal of Nuclear Engineering*, 2(4):471–483, 2021. 143, 149

[133] Jess C Gehin and Jeffrey J Powers. "Liquid fuel molten salt reactors for thorium utilization". *Nuclear Technology*, 194(2):152–161, 2016. URL `https://www.osti.gov/pages/servlets/purl/1254086`. 150

# Vita

Nicholas Dunkle grew up in Franklin, Tennessee. From an early age they had an innate interest in science. After high school, they pursued a higher education at the University of Tennessee, Knoxville. There, they earned a Bachelor's degree in Nuclear Engineering with a minor in Material Science and Engineering. They continued their studies with graduate school at UTK. There, they earned a Master of Science degree in Nuclear Engineering, a Doctor of Philosophy degree in Nuclear Engineering, and a Nuclear Security Science and Analysis graduate certificate. Their research interest includes the study of advanced reactors with a particular interest in molten salt reactors. They are very grateful for all the support they have received.